5-2018

An Experimental and Computational Investigation into Laser-Based Synthesis and Spectrochemical Characterizations of Metal/intermetallic Nanoparticles with Engineered Interfacial Functionalities

Seyyed Ali Davari
University of Tennessee, sdavari@vols.utk.edu

To the Graduate Council:

I am submitting herewith a dissertation written by Seyyed Ali Davari entitled "An Experimental and Computational Investigation into Laser-Based Synthesis and Spectrochemical Characterizations of Metal/intermetallic Nanoparticles with Engineered Interfacial Functionalities." I have examined the final electronic copy of this dissertation for form and content and recommend that it be accepted in partial fulfillment of the requirements for the degree of Doctor of Philosophy, with a major in Mechanical Engineering.

Dibyendu Mukherjee, Major Professor

We have read this dissertation and recommend its acceptance:

Gerd J. Duscher, Bamin Khomami, Zhili Zhang

Accepted for the Council:

Dixie L. Thompson

Vice Provost and Dean of the Graduate School

(Original signatures are on file with official student records.)

An Experimental and Computational Investigation into Laser-Based Synthesis and Spectrochemical Characterizations of Metal/intermetallic Nanoparticles with Engineered Interfacial Functionalities

A Dissertation Presented for the

Doctor of Philosophy

Degree

The University of Tennessee, Knoxville

Seyyed Ali Davari

May 2018

Dedication

This dissertation is dedicated to my wonderful family who equipped me with great values that help me to find my path in difficult times.

To the memory of my grandmother, Banoo Jan.

Acknowledgement

I have had a great opportunity to work with wonderful people during my time at UT. I would like to thank my advisor, Dr. Dibyendu Mukherjee, for numerous valuable lessons in my academic and personal life. He provided a rare positive environment for independent thinking. This dissertation would not come together in lack of his mentorship.

I would like to thank my committee members, Prof. Khomami, Prof. Duscher, and Prof. Zhang for serving as my committee members and providing critical comments and questions to improve the current work.

I would like to thank my collaborator and committee memeber Prof. Duscher for providing technical assistance during TEM and EELS measurements. I would like to thank Dr. Masjedi for handling biomedical part of our collaboration to extend LIBS in biomedical engineering. Special thanks to Dr. Gottfried for performing LASEM measurements in our samples.

I would like to thank SunEdison Semiconductor Ltd. for providing financial supports during two years of my Ph.D.

Special thanks to my lab mates, Dr. Sheng Hu, Erick Ribeiro, and Brian Park who created a fantastic work place and shared great memories.

My greatest appreciation goes to my mother Mahvash Amin, my father Seyed Esmaeil Davari, my grandmother Banoo Jan, my brother Reza, my in-law Mahsa, and Uncle Mehrdad who influenced me in many instructive ways.

“The Grape that can with Logic absolute

The Two-and-Seventy jarring Sects confute:

The sovereign Alchemist that in a trice

Life's leaden metal into Gold transmute”

- Quatrains of Omar Khayyam

Abstract

Nanomaterials have, over the years, generated tremendous interests of scientists and engineers from nearly all disciplines. This interest has been due to a large number of desired physico-chemical properties such as magneto-optic properties, mechanical strength, melting points, charge transport behavior, and surface reactivity exhibiting unique size-dependent characteristics at the nanoscale. The unique interfacial properties are widely believed to be a result of high ratio of surface to bulk atoms as well as, bridging states in which nanoparticles exist between atomic and bulk materials. Thus, in the world of material processing and engineering, recent years have seen a surge in the use of wide classes of nanostructured materials as novel energetic, catalytic, semiconductor, and biomedical materials with engineered functionalities that find use in industrial, technological and defense applications. Therefore, it becomes imperative to develop fundamental understanding on the manufacturing and characterization routes that can allow the systematic tuning of the interfacial-property characteristics of advanced nanomaterials by tailoring their sizes and architectures. The current PhD thesis aims to address this grand-challenge engineering problem by investigating early-stage formations theoretically, synthesis and novel spectrochemical characterizations of advanced metal/intermetallic and composite nanoparticles (NPs) with engineered surface properties. Specifically, the thesis is categorized into two broad sections, namely laser-based synthesis studies and laser-based spectroscopic characterizations of NPs. The synthesis section presents theoretical investigations into the inception stage of NP formations, namely nucleation via numerical simulations. Briefly, this section aims to reveal the processing-structure-property relations of metal NPs synthesized via gas phase routes in an effort to relate the processing parameters to the size and morphology of the NPs, which in turn, dictates their

interfacial energetic and catalytic behaviors. Then, using the obtained fundamental understandings a laser-based synthesis technique is presented for generating novel energetic metallic nanocomposites. The size, morphology and energetic activities of these materials are analyzed and tuned to improve the energetic properties. Finally, the laser spectroscopic characterization section focuses on experimental investigations by introducing laser induced breakdown spectroscopy (LIBS) as a relatively non-destructive and robust spectrochemical technique for the structural and chemical composition characterizations of composite NPs in a facile, yet effective manner.

Table of Contents

List of Tables

List of Figures

Chapter 1 Introduction

1.1 Nanomaterials with interfacial functionalities: Synthesis & characterization techniques

1.1.1 Synthesis

Nanomaterials have attracted the interests of materials science researchers for more than 60 years now. Tailoring the properties of materials at nano-scale by changing their sizes and morphologies has been the center of all these efforts. To this end, numerous studies till date have tried to explain why and how material surface properties can be changed as the size decreases. An obvious and immediate answer is that at nano-scale, the properties of materials change due to the large surface area available. A more detailed discussion into this leads to the more fundamental understanding that for materials with nanometer length scales, atoms and molecules at the surface have lesser number of nearest neighbors which leads to unsaturated bonds [1]. The state of these surface atoms or molecules is different than the atoms in the bulk and the thickness of this particular surface atoms is about 5 atomic layers; ~1 nm [1]. Therefore, it is needless to say that to tailor the various physico-chemical properties of nanomaterials it becomes essential to control their characteristic sizes and shapes during the synthesis processes.

In general, the synthesis of nanomaterials can be categorized in two groups: *Top-Down* and *Bottom-Up* approaches. The *Top-Down* approach refers to the synthesis technique that starts with a bulk material and attempts to reduce the size of the bulk material to nano size through mechanical fragmentation (Figure 1.1). The mechanical fragmentation can be implemented via various equipment including ball, vibration, vortex mills etc. [2]. While this approach is relatively simple, it is difficult to control the sizes and shapes of the nanoparticles. The *Bottom-Up* approach, which has gained significant interest recently, refers to the techniques that attempt to build up

multifunctional nanostructures by self-assembly of atoms and molecules. The inception of nanoparticle formation starts with the nucleation process. Usually a metastable supersaturated state is required to induce homogeneous/heterogeneous nucleation that subsequently continues and sustains the growth process. Generally, the supersaturated state can be prepared through chemical and physical approaches. In the first approach, a chemical reaction is induced by which a species is released whose concentration reaches the desired limit to create a saturated state thereby initiating the nucleation and subsequent growth process.

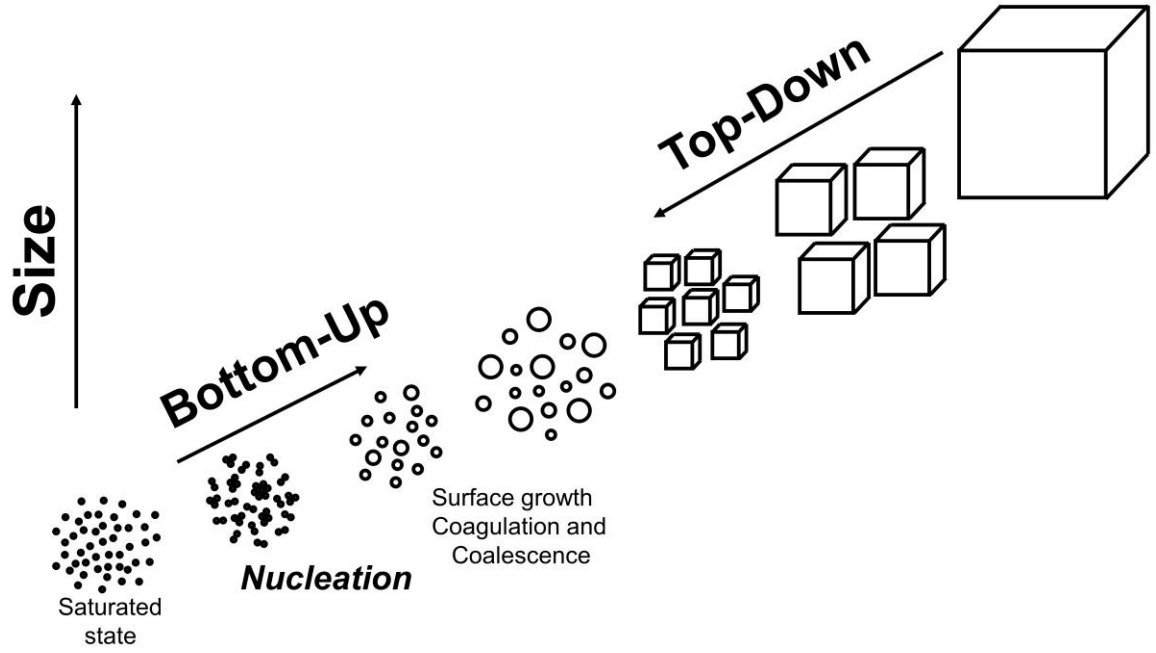

Figure 1.1: Top-down vs bottom up approaches.

Various methods such as chemical vapor synthesis (CVD) [3], spray pyrolysis [4], flame synthesis [5] etc. have been employed regularly for formation of nanoparticles. In the second method, a high-energy physical process initiates the creation of the supersaturated state for the species of interest. In this category, various techniques have been developed such as inert gas condensation [6], ion sputtering [7], electric arc discharge [8], and pulsed laser ablation [9]. Considering the steady increase in advanced design of pulsed lasers in terms of their output powers, repetition rates and

pulse durations, the yield of nanoparticle production has been increased rapidly which draws the attention of materials science researchers to laser ablation synthesis. Moreover, laser ablation provides facile, green and yet robust routes for initiating plasma-confined non-equilibrium pathways that can generate metastable structures which are otherwise difficult to attain via common chemical synthesis routes [10, 11]. However, laser ablation synthesis in air results in large-scale particle aggregations and a relatively weaker control on their compositions apart from the fact that it might cause workplace contamination with aerosols which can endanger the health of workers and researchers [12]. Therefore, in recent years significant efforts have been dedicated to laser ablation in solution which is relatively a safe medium for laser ablation synthesis. In the current thesis, laser ablation in solution (LASiS) has been investigated for production of engineered nanoparticles with tunable properties in the following chapters.

1.1.2 Characterization

In conjunction with synthesis routes, various characterization techniques for the as-synthesized nanomaterials have always played a pivotal role in providing necessary controls and feedbacks to the synthesis processes. Various properties are needed to be considered for evaluating a synthesized nanomaterial. In general, nanomaterials are characterized by their sizes, morphologies, physical and chemical properties. Numerous characterization techniques have been developed for obtaining the properties of nanomaterials. Here, we briefly introduce a few common and widely used physical and chemical characterization tools and techniques for nanomaterials.

In regards to physical characterizations, transmission electron microscopy (TEM), is a powerful imaging tool for obtaining size, and morphology information, which when coupled with energy dispersive X-ray (EDX), selected area electron diffraction (SAED) and electron energy loss spectroscopy (EELS) can also provide qualitative chemical compositions, crystal structure

properties, etc. Usually, the nanoparticles are dispersed on an electron-transparent substrate. Typically, TEM works based on an electron beam focused on a small area that passes, bombards and interacts with the sample to provide structural information. Scanning electron microscopy (SEM) is similar to TEM but based on the secondary electron emitted from the sample surface. In general, the electron beam has lower energy and results in poorer resolution when is compared to the TEM technique. On other hand, atomic force microscopy (AFM) is used for physical and topological characterizations of the sample surface as a fine nano-scaled tip interacts with the sample to experience attractive/repulsive forces close to the sample surface. In regards to chemical characterizations, inductively coupled plasma-optical emission spectroscopy (ICP-OES) can be employed to obtain information about the chemical and elemental composition of the sample. Here, inductively-induced plasma is employed to decompose and excite the elements that comprise the sample. The plasma provides the energy to excite the elements to upper levels of energy. As they relax back to the lower states of energy they emit light in proportion to the energy differences between energy levels in terms of ionic, atomic or molecular emissions. These emissions can be used for qualitative and quantitative analysis of samples chemical compositions.

The need for obtaining accurate results with minimum time/energy investment motivates researchers/engineers to develop new characterization techniques. While the aforementioned techniques are powerful, they are either significantly expensive such as TEM or involved with cumbersome sample preparation steps and lack of convenience to be implemented for in-line measurements. Obeying the same principles of ICP-OES and other optical emission spectroscopy techniques, recently extensive efforts have been focused on laser-induced breakdown spectroscopy (LIBS) due to its promising features in regards to the cost and simplicity of data collection/analyses

that can address the above issues. In this thesis, we will study and discuss this technique extensively in later chapters.

1.2 Laser-based synthesis: Laser ablation synthesis in solution (LASiS)

LASiS employs a high-energy laser to evaporate a target immersed in a solution to generate nanomaterials. Specifically, a pulsed laser with flux above ~ 1 GW/cm^2 is irradiated on a target (Figure 1.2 a). Laser energy is transferred to the target, increases its temperature and evaporates it abruptly (Figures 1.2 b and c). The evaporated target atoms are at high temperature and pressure, therefore undergo numerous effective collisions. These collisions result in excitation of the atoms to ionic species and consequently creation of small volume plasma (Figure 1.2 d and e). Upon creation of the plasma, a radial shock wave is released into the liquid due to expansion of the plasma. The plasma contains various excited ionic and atomic species generated from the target and ambient liquid and as they relax to the ground state, they can be probed spectroscopically.

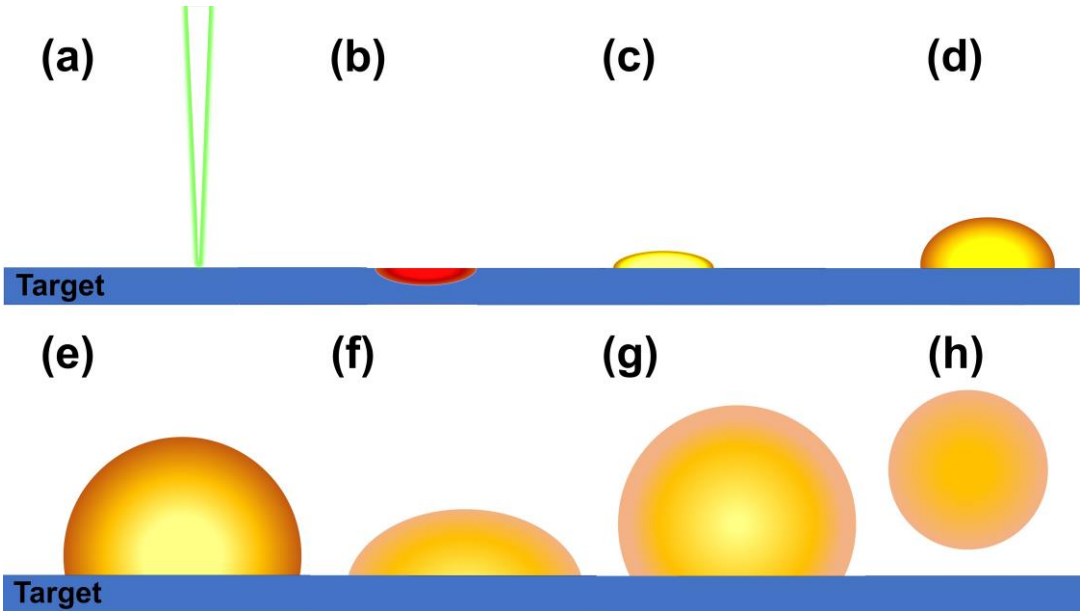

Figure 1.2: Evolution of laser-matter interaction and bubble dynamics in solution.

As the plasma quenches the energy is transferred to the surrounding liquid and results in evaporation of the liquid which continuously grows and becomes a bubble. The generated vapor has approximately the same volume as the plasma [13]. A few microseconds after the first shock wave, a second shock wave parallel to the target is observable. The second parallel shock wave has been attributed to the sound wave [14]. The cavitation bubble experiences a periodic expansion and compression before it completely collapses [15] (Figure 1.2 f and g). While the bubble is expanding and shrinking, a supersaturated state is generated due to fast cooling of the plasma and evaporated atoms from the target. This saturated condition triggers the homogeneous/heterogeneous nucleation and subsequently formation of the primary particles and even aggregates [16] (Figure 1.3 d). Generally, nucleation can be realized as a first-order phase transition that marks the birth of a thermodynamically stable condensed phase in the form of a critical nucleus and is the precursor to the crystallization process, followed by subsequent growth of the critical cluster via coagulation and condensation/evaporation processes. In formation of particles, nucleation is the first physical process that occurs during system evolution. Based on existence of foreign seeds, nucleation can be subcategorized into homogeneous, and heterogeneous nucleation. Atoms and molecules need nucleation sites in order to condense and create a new phase. The nucleation sites can be provided by the nucleating atoms, and molecules (self-nucleation) or by another material or surface. Homogeneous nucleation is defined as nucleation of specific phase of a material (vapor e.g.) on embryos comprised of that material, while foreign seeds do not play any role in terms of providing nucleation site in the process.

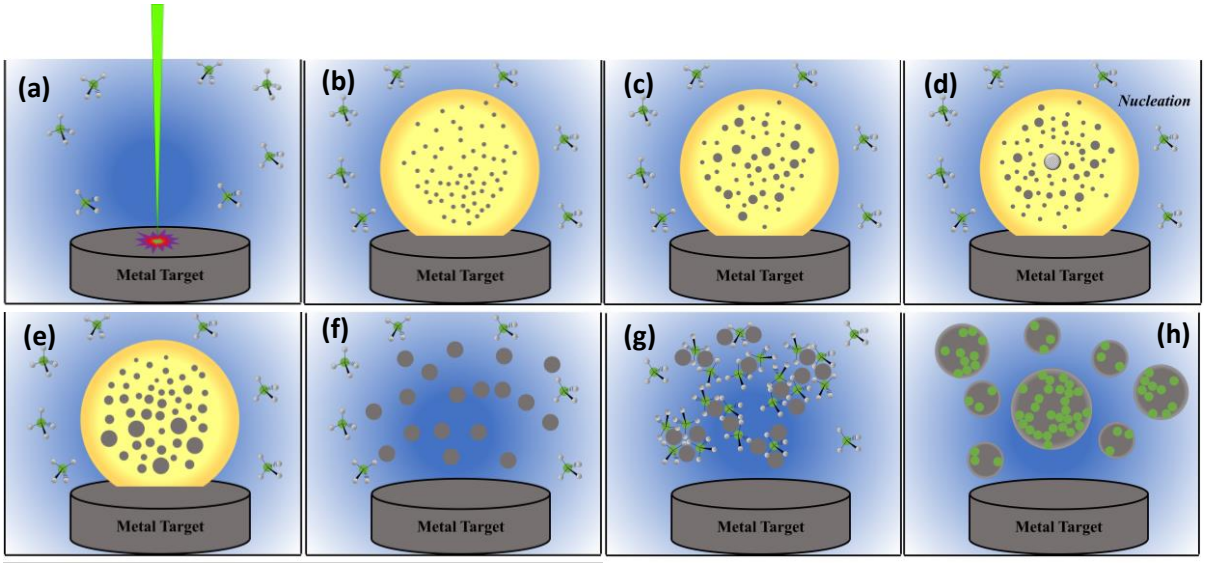

Figure 1.3: Schematic of LASiS evolution during formation of nanoparticles.

On the other hand, heterogeneous nucleation is the nucleation of specific phase of a material (vapor e.g.) on an embryo comprised of another material. Homogeneous nucleation is a kinetically disfavored process that involves surmounting a nucleation barrier during the vapor-phase cooling of monomers leading to supersaturation where in clusters grow via collisions and/or condensation of monomers, or decompose into smaller clusters and monomers via evaporation. The aforementioned processes continue till the critical nucleus is formed (Figure 1.3 d) as the new phase that resides on top of the nucleation barrier and undergoes barrier-less spontaneous growth under any perturbation (Figure 1.3 e). The presence of a free energy barrier in a first-order phase transition process makes nucleation a rare event whose exceedingly small length and time scales pose an insurmountable challenge for designing experiments that can accurately monitor and/or control the in-situ NP formation. It has been shown that along the cavitation bubble height there is a smooth transition from the primary particles to secondary particles [16]. Chemical reaction can be incorporated during these processes for engineering functionalized nanomaterials (Figure 1.3 g). It has been suggested that once the bubble collapses, the formed nanoparticles are released into

the solution and chemical reactions take place [17]. However, it is worth mentioning that the exact position and time of these chemical reactions are not completely known yet and occurrence of chemical reactions has been reported at all stages of the LASiS including plasma cooling [18], bubble expansion [19] and bubble collapse [20].

1.3 Laser-based spectroscopic characterization: Laser-induced breakdown spectroscopy (LIBS)

The high-energy laser ablation technique can also be implemented for chemical characterization of samples. Here, the general idea is to evaporate a sample and generate high pressure and high temperature plasma emissions. By measuring the laser-induced plasma emission spectrum, qualitative and quantitative information about the sample chemical composition can be revealed. Based on the properties of the laser, such as laser energy, wavelength, pulse width, repetition rate etc. the processes for generating plasma is different. In this direction, recent efforts have been specifically directed towards tuning the pulse width (nanosecond, picosecond or femtosecond time scales) to tailor the physics of the desired ablation process and hence, the plasma emission characteristics. Thus, in femtosecond pulsed lasers, the photoionization are dominant through which electrons absorb laser energy and become excited to the conduction band. Also, due to superposition of nuclear Coulomb field and laser electric field, the potential barrier might oscillate and valance electrons can escape atoms through tunneling (tunneling ionization). Meanwhile, free electrons can absorb laser energy and increase their energies and through collisions with valance electrons increase the population of free electrons (Avalanche ionization). This process can be continued till the laser electromagnetic field is available. Once ~10% of valance electrons are removed through these ionization processes, the lattice becomes weak and starts melting. The process is known as non-thermal melting or Coulomb explosion [21, 22].

While the ionization process and plasma generation is mostly non-thermal in femtosecond laser ablation, thermal ionization is the dominant process for plasma generation in nanosecond pulsed lasers. Basically, as it was explained earlier the laser energy is spent for heating, melting and vaporizing the sample. The vaporized sample can be ionized either by absorbing laser beam or through thermal collisions. Another difference between the femtosecond and nanosecond lasers is related to plasma shielding. Since the pulse duration is significantly longer in compare to femtosecond, part of the laser irradiance is absorbed by the materials during the plasma expansion while this process is negligible in femtosecond pulses. Plasma expansion can be considered adiabatic up to ~ 1μs. In this period, continuum emission can be observed up to several hundred nanoseconds. Also, ionic emission is observable in this period. After this time, the dominant energy loss is due to atomic and molecular lines radiations affecting plasma temperature. These emissions contain information regarding the sample chemical compositions. Under certain conditions these emissions can be employed to obtain the chemical composition of ablated samples. The first required condition is stoichiometric ablation in which the elemental composition of ablated materials is the same as the sample. It has been showed that at high irradiance this condition is fulfilled [23]. The local thermodynamic equilibrium (LTE) is the second necessary condition. At full thermodynamic equilibrium, each process is accompanied with its reverse (detailed balance) pathway, thereby indicating the emergence of optically thick plasma with an abundance of collisional pathways. However, once the energy loss due to emission from the plasma is much smaller than the total energy of the plasma, LTE can be established in which distribution of all the plasma species can be characterized by a single temperature value through Maxwell-Boltzmann equation.

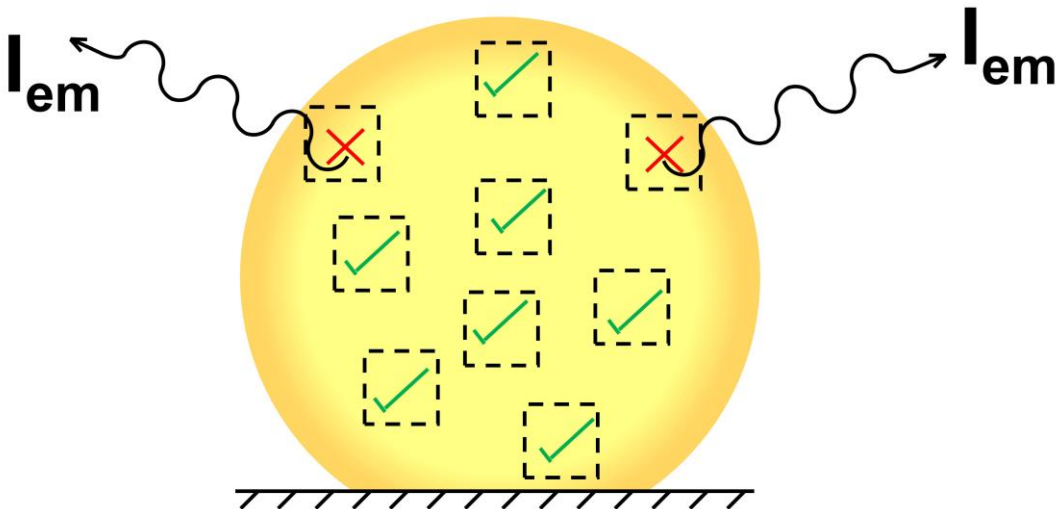

Figure 1.4: Establishment of LTE through negligible energy loss due to emission in compare to the plasma total energy.

Generally, four criteria are necessary for LTE establishment: 1) the rate of collision processes has to be greater than radiative processes (McWhirter); 2) the rate of change in the plasma parameters should be smaller than the typical time scales required for establishing equilibrium; 3) the length scale of thermodynamic parameters should be larger than the diffusion length of atoms [24]. A reasonable satisfaction of all these conditions lead to the establishment of plasma LTE. The third necessary condition for obtaining chemical composition of ablated sample is plasma spatial homogeneity. And final condition is the plasma optical thinness in which the self-absorption must be minimized which always becomes challenging for dense plasmas under LTE. Generally, self-absorption usually occurs for transitions with low excitation energy of upper levels and high transition probabilities, especially being prevalent for resonant lines [25]. Fulfilling the aforementioned conditions can lead to more accurate quantitative analysis during laser-induced breakdown spectroscopy.

1.4 Scope of the present thesis

In light of the above-mentioned tools and techniques for acquiring fundamental understanding on the synthesis and characterization of advanced engineered nanomaterials, the prime objective of this research work is to provide detailed experimental and computational investigations into high-energy laser-based synthesis and spectrochemical characterizations of composite nanomaterials with designed surface functionalities. To this end, the current thesis will be developed and divided into the following chapters, each addressing a critical problem related to the aforementioned research objective. In Chapter 2, we will delve into a high-fidelity computational study on homogeneous nucleation as the inception stage during Bottom-Up formation of nanoparticles in high energy gas-phase synthesis routes such as flame and/or plasma synthesis. Here, our motivation stems from the fact that the size and nucleation rates of primary particles formed during their inception stages determine the fate, transport and evolution of nanoparticles. We employ a stochastic Monte-Carlo approach which is ideal for describing random collisions among clusters during the nucleation process. Chapter 3 is dedicated towards the introduction of LASiS technique as a high energy synthesis routes for producing metallic nanocomposites with engineered interfacial functionalities for energetic applications. Following this, Chapter 4 will focus on a comprehensive investigation into the development of LIBS technique for the elemental analyses of diverse classes of metallic, intermetallic nanoalloys and nanocomposites. Herein, we will go into the details for carrying out quantitative calibration-free LIBS analyses of chemical compositions of the nanomaterials, and compare the quantitative LIBS results to conventional techniques such as ICP-OES. Moreover, in the appendices we will also demonstrate the efficacy of the LIBS technique when extended to other systems such as biological samples and semiconductor thin films analyses (Appendices A and B).

Chapter 2 Homogeneous Nucleation: A Theoretical Study on the Inception of Nanoparticles

This chapter is based on the following publications:

- **Davari, S. A.**; Mukherjee, D. (2018) "Homogeneous nucleation of metal nanoparticles: A kinetic Monte Carlo model to study the vapor phase synthesis of Al nanoparticles", AIChE J., 64, 18-28

- Mukherjee D., **Davari S.A.** (2017) "Computational Modeling for Fate, Transport and Evolution of Energetic Metal Nanoparticles Grown via Aerosol Route". In: Shukla M., Boddu V., Steevens J., Damavarapu R., Leszczynski J. (eds) "Energetic Materials. Challenges and Advances" in Computational Chemistry and Physics, vol 25. Springer, Cham

2.1 Introduction

Recent years have seen a rise in the use of metal nanoparticles (NPs) as novel energetic, catalytic, and semiconductor materials with engineered functionalities [26, 27]. To this end, it becomes imperative to tune the structure-property characteristics of these NPs by tailoring their sizes and architectures during industrial or, laboratory-based vapor phase synthesis involving rapid cooling of saturated atoms or molecules (monomers). Particle formation from vapor phase occurs in two distinct stages: 1) homogeneous nucleation that produces thermodynamically stable condensed phase in the form of a critical nucleus within a metastable phase, and is the precursor to the crystallization process; 2) subsequent growth by coagulation and condensation/evaporation processes of the critical nucleus to NPs of larger sizes.

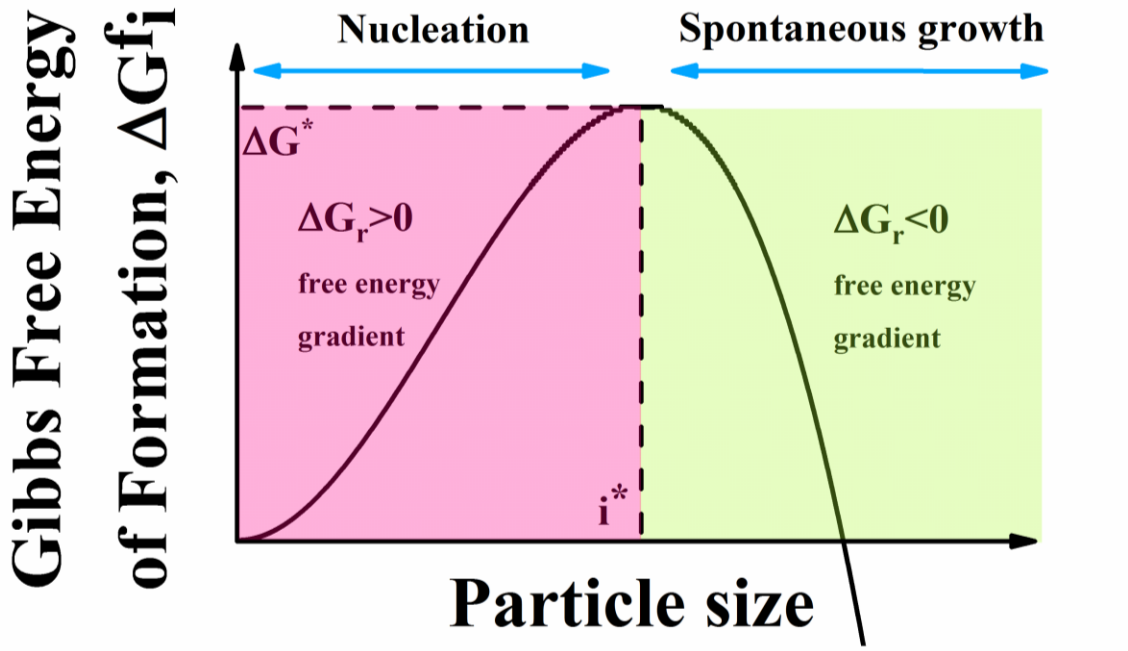

Figure 2.1: Typical Gibbs free energy of formation as a function of cluster size.

Homogeneous nucleation is a kinetically disfavored process that involves surmounting a nucleation barrier during the vapor phase cooling of monomers (Figure 2.1). The process leads to cluster growth via collisions and/or condensation of monomers, or cluster decomposition into smaller clusters and monomers via evaporation [28, 29]. The processes continue until a critical nucleus is formed as a new phase perched atop the nucleation barrier. Any perturbation at this stage allows the critical nucleus to undergo barrier-less spontaneous growth. In the framework of classical nucleation theory (CNT), the Gibbs' free energy of a cluster formation with size i, ΔG_i^f, contain two terms; a favorable bulk free energy term and an unfavorable surface energy term due to the formation of an interface between the phases [30-32]. However, the presence of a free energy barrier in a first-order phase transition process makes nucleation a rare event. A few significant experimental efforts in the past have investigated the synthesis of nanoparticles via flame synthesis routes [33-35]. But, the exceedingly small length and time scales of the nucleation process pose significant challenge for designing experiments that can accurately monitor and control the in-situ

NP formation [36-38]. It needs to be mentioned here that although CNT assumptions have been much debated over the years, a vast majority of homogeneous vapor phase nucleation studies resort to CNT due to its ability to predict relatively accurate results in a convenient fashion [32, 39-43]. The main point of contention in CNT arises from the capillarity approximation that extends bulk thermodynamic properties to nano-scale clusters. This, in turn, leads to errors in the free energy estimation of clusters below the critical size [44, 45].

The aforementioned challenges highlight the need for hi-fidelity simulations that can model the mechanistic and collective picture of vapor-phase homogenous nucleation for predictive synthesis of tailored metal NPs. Past phenomenological models have resorted to solving population balance equations using sectional and nodal techniques [29, 41] including our hybrid nodal method that accounted for size-dependent surface tension in the nucleation study [46]. Although such methods are robust and capture large time-scale processes, they suffer from numerical diffusion and round-off errors due to the discrete binning of cluster sizes, and resort to steady-state nucleation rate derivations in many cases. On the other hand, molecular simulations comprising both Monte Carlo (MC) and molecular dynamics (MD) modeling have been used to estimate the structural and free energy variations from first principles [47]. To this end, MC configuration integral and MD simulations enabled the calculation of Gibbs free energy changes and association rate constants for Al clusters [31, 48]. Although such atomistic simulations capture the physics of NP formation at specific temperatures and saturation ratios, they fail to capture the ensemble nucleation process during real-time cooling of a background gas [49]. Specifically, this becomes computationally challenging bearing in mind that typical MD time scales (~1 fs) would require 1014 time-steps to simulate such a process. On the other hand, MC has the ability to capture ensemble processes [50]

leading to rare events and is not being limited to MD time scales. However, unlike MD simulations, it is limited on its ability to capture the detailed atomistic picture of the process dynamically.

Here, we develop a stepwise constant-volume kinetic Monte Carlo (KMC) model to simulate vapor phase nucleation of Al NPs via random collisions and temporal evolution of clusters. We use the CNT-based formulation for Gibbs' free energy of cluster formation to allow for easy comparison with earlier nucleation studies [29]. The model is based on the fundamental principles of Metropolis algorithm and applies a pseudo sampling technique that is capable of capturing the rarity of first-order phase transitions. To the best of our knowledge, no similar KMC models have been developed till date to simulate ensemble gas-to-particle conversions during rapid cooling of gas phase monomers without a priori constraints on the system cluster distributions.

2.2 Mathematical model and theory

The change in Gibbs' free energy of cluster formation (ΔG_i^f) comprising of i monomers (i.e., an i-mer) based on the self-consistent CNT is expressed as [51]:

$$\frac{\Delta G_i^f}{k_B T} = \theta(i^{2/3} - 1) - (i - 1)\ln(S) \tag{2.1}$$

where θ is the dimensionless surface tension defined as:

$$\theta = (36\pi)^{1/3} v_1^{2/3} \frac{\sigma}{k_B T} \tag{2.2}$$

and v_1, σ, k_B and T are volume of monomer, surface tension, Boltzmann constant and temperature respectively. S is the saturation ratio given as the ratio of monomer concentration in the simulation box (n_1) to the saturated monomer concentration (n_s) based on the saturated vapor pressure of monomers in equilibrium with its liquid phase at a specific T:

$$S = \frac{n_1}{n_s} \tag{2.3}$$

Figure 2.1 schematically illustrates ΔG_i^f as a function of cluster size. Based on the Gibbs free energy of formation, the equilibrium size distribution can be expressed as:

$$n_i^e = n_1 \exp\left(-\frac{\Delta G_i^f}{k_B T}\right) \tag{2.4}$$

The size distribution of clusters that undergo cluster-cluster collision, condensation and evaporation is given by the population balance equation:

$$\frac{dn_i}{dt} = \frac{1}{2}\sum_{j+k=i} K_{j,k} n_j n_k - n_i \sum_{j=2} K_{j,i} n_j + (k_{f,(1,i-1)} n_{i-1} n_1 - k_{b,(i)} n_i) - (k_{f,(1,i)} n_i n_1 - k_{b,(i+1)} n_{i+1}) \tag{2.5}$$

Where n_i is the concentration of i-mer particles and $K_{i,j}$ is the free molecular collision kernel between an i-mer and j-mer:

$$K_{i,j} = \left(\frac{3v_1}{4\pi}\right)^{1/6}\left(\frac{6k_B T}{\rho}\right)^{1/2}\left(\frac{1}{i} + \frac{1}{j}\right)^{1/2}\left(i^{1/3} + j^{1/3}\right)^2 \tag{2.6}$$

where ρ is the mean density of clusters. In eqn. (2.5) $k_{f,(1,i-1)}$ is the forward reaction rate between a (i-1)-mer and a monomer and $k_{b,(i)}$ is the backward reaction rate for the dissociation of an i-mer. These forward and backward rates are associated with the following reaction:

$$A + A_{i-1} \underset{k_{b,(i)}}{\overset{k_{f,(1,i-1)}}{\rightleftharpoons}} A_i \qquad \textbf{(R1)}$$

From eqn. (2.1), the difference in Gibbs free energy during (R1) is given as:

$$\frac{\Delta G_{i,i-1}^r}{k_B T} = \frac{\Delta G_i^f}{k_B T} - \frac{\Delta G_{i-1}^f}{k_B T} = \theta\left[i^{2/3} - (i-1)^{2/3}\right] - \ln(S) \tag{2.7}$$

Furthermore, thermodynamic equilibrium constants are defined as:

$$K_p = e^{\frac{-\Delta G^r_{i,i-1}}{k_B T}} \tag{2.8}$$

$$K_c = \frac{k_{f,(1,i-1)}}{k_{b,(i)}} \tag{2.9}$$

$$K_p = K_c n_1 \tag{2.10}$$

Hence, based on eqns. (2.8-2.10), the backward reaction rate can be derived as [46]:

$$k_{b,(i)} = k_{f,(1,i-1)} n_s \exp(\theta[i^{2/3} - (i-1)^{2/3}]) \tag{2.11}$$

where $k_{f,(1,i-1)}$ is assumed to be the free molecular collision kernel $K_{i-1,1}$ between clusters with sizes i-1 and monomers.

KMC model development:

Numerous studies have investigated the evolution of aerosol size distributions using MC methods [52-57] that have shown the capabilities of MC approach to approximate aerosol growth processes. Generally, MC methods can be divided into two classes: Constant-Volume (*Constant-V*) and Constant-Number (*Constant-N*). In the *Constant-V* method, the number of particles in the system reduces over time. Due to the accuracy of MC simulations being proportional to $\frac{1}{\sqrt{N}}$ [55] this method is only applicable to systems with large number of particles and hence, is computationally expensive. To overcome this, two different MC methods have been classically proposed. The first is the Constant-N method which the number of system particles is kept fixed by adding a particle at each time step. And the second is the stepwise constant-V [58] method wherein the system duplicates the particles array whenever the number of particles drops to half of the initial value [55].

The aforementioned stepwise constant-V MC via duplication can be implemented in two directions. In the first approach (time-driven), a time step is chosen and the number of events is specified by the probability of events driven by MC. In the second approach (event-driven), an event is identified through the MC and an appropriate time increment is calculated and added to the time [56]. The advantage of the latter is that one does not need to specify any pre-calculated time increment prior to the simulation. However, the rates of transition between the states are required in both the cases.

Based on our earlier KMC model [59] the current study employs the stepwise constant-V method in conjunction with the event-driven approach to simulate the vapor phase nucleation of Al NPs. First, we identify an event based on the MC probability of success for the event. Then, driven by the transition rate for the selected event, a time increment is calculated and added to the MC time scale. Assigned probabilities are derived based on the Gibbs free energy change associated with (R1) and the free molecular collision kernel given by eqn. (2.6). All simulations presented here start with 20,000 monomers in the MC volume.

Implementing the MC algorithm:

At each MC time step, two processes can take place namely, growth (categorized as condensation and cluster-cluster collisions), and/or evaporation. By condensation, we refer to collisions between a monomer and i-mer, whereas cluster-cluster collisions indicate collisions between an i-mer and a j-mer. Each of these processes has inherent MC probabilities assigned to them. Using a random number generator, two clusters with sizes i and j are first chosen ($i, j \in [1, M]$, where M is the total number of MC clusters). Based on the condensation or cluster-cluster collision probabilities, two clusters with sizes i and j might be combined to form a new cluster with size i+j, and the total number of clusters is reduced by unity. Furthermore, a cluster with size k is randomly chosen such

that k ∈ [2, M]. Based on the evaporation probability, the cluster with size k is decomposed to a cluster with size k-1 and a monomer, and the total number of monomers is increased by unity. Any statistical inaccuracies arising from cluster depletion are addressed by duplicating the system when the total number of clusters in the system drops to half of the initial value. Such topping-up does not change the cluster size distribution owing to periodic boundary conditions, while conserving the system mass loading due to corresponding adjustments in the MC volume.

Cluster-cluster collision:

Cluster-cluster collision occurs when an i-mer and a j-mer collide. The probability of the collision event (Pcollision) is determined from the free molecular collision kernel as [59]:

$$P_{collision} = \frac{K_{i,j}}{K_{max}} \tag{2.12}$$

where K_{max} is the maximum value of the kernel among all clusters. Mathematically, it can be inferred that the maximum kernel occurs when i=1 and j=i_{max} where i_{max} is the maximum cluster size in the system. Theoretically in eqn. (2.12), $K_{i,j}$ should be normalized by the sum of all kernels. However, normalizing to K_{max} makes the computational cost less intensive without affecting the accuracy noticeably [60, 61].

Condensation:

Condensation refers to collisions between a monomer and an i-mer. Based on the Metropolis algorithm, the probability of condensation is defined as:

$$P_c = \begin{cases} e^{\frac{-\Delta G^r_{i,i-1}}{k_B T}} & \Delta G^r_{i,i-1} > 0 \\ 1 & \Delta G^r_{i,i-1} \leq 0 \end{cases} \tag{2.13}$$

Eqn. (2.13) states that the transition probability between the current state and the trial state has a Boltzmann distribution. It can be realized from Figure 2.1 that the difference in Gibbs free energy

during (R1) ($\Delta G^{r}_{i,i-1}$ as given by eqn. (2.7)) is always positive for the clusters smaller than the critical cluster ($\Delta G^{r}_{i,i-1} > 0$), and is negative for the clusters/particles larger than the critical cluster ($\Delta G^{r}_{i,i-1} < 0$), where the critical cluster size is denoted as i*.

After the nucleation burst, a barrier-less condensation on critical clusters will result in spontaneous particle growth with a probability of unity ($P_c = 1$) as seen from eqn. (2.13). However, now the driving force for monomer condensation on a particle is the difference between n_1 and the saturated monomer concentration (or the saturated vapor pressure) on an i-mer ($n_{s,i}$) droplet. Hence, based on the reaction rate for condensation driven by Kelvin relations, the probability of surface growth ($P_{surf\ growth}$) after the nucleation burst (for i>i*) is modeled as:

$$P_{surf\ growth} = \frac{K_{1,i\ 1}}{K_{max}}\left(1 - \frac{n_{s,i\ 1}}{n_1}\right) \tag{2.14}$$

where, $n_{s,i}$ over an i-mer is obtained from the Kelvin relations as :

$$n_{s,i} = n_s \exp\left(\frac{4\sigma v_1}{d_i k_B T}\right) \tag{2.15}$$

where, d_i is the diameter of an i-mer.

Evaporation:

The probability of evaporation (P_e) for reaction (R1) is derived from the probability of condensation (P_c) using detailed balancing as:

$$P_e = \begin{cases} 1 & \Delta G^{r}_{i,i-1} > 0 \\ e^{\frac{\Delta G^{r}_{i,i-1}}{k_B T}} & \Delta G^{r}_{i,i-1} \leq 0 \end{cases} \tag{2.16}$$

Eqn. (2.16) indicates that for the left side of the nucleation barrier (where $\Delta G^{r}_{i-1,i} = -\Delta G^{r}_{i,i-1} \leq 0$), evaporation always happens successfully. However, for the right side of the nucleation barrier

(where $\Delta G^{r}_{i-1,i} = -\Delta G^{r}_{i,i-1} > 0$), evaporation should be restricted by the Boltzmann factor. However, as also explained earlier, the evaporation of particles during the relaxation after the nucleation burst is also driven by the relative difference between n_1 and $n_{s,i}$. Hence, driven by the Kelvin relations (as explained earlier), the probability of evaporations after the nucleation burst (P_{diss}) (for $i>i^*$) is modeled as:

$$P_{diss} = \frac{K_{1,i}}{K_{max}}\left(1 - \frac{n_1}{n_{s,i}}\right) \tag{2.17}$$

KMC Time step:

For the growth processes, the KMC time is inversely proportional to the sum of the rates of all possible growth events as:

$$\Delta T_f = \frac{V}{\sum R} = \frac{2V}{\sum_{i=1}^{M}\sum_{j=1,j\neq i}^{M} K_{i,j}} \tag{2.18}$$

where V is the MC volume calculated from the initial monomer concentration and number of clusters ($V = \frac{M_0}{n_0}$). Considering the stochastic equilibrium for the KMC system, the summation in eqn. 2.18 is estimated from the collision kernel of the selected pair for the sake of computational efficiency [53, 61]:

$$\Delta T_f \approx \frac{2V}{M(M-1)K_{ij}} \tag{2.19}$$

where K_{ij} is the collision kernel of the selected pair.

Moreover, from eqn. (2.11) the MC time step for evaporation events can be calculated from:

$$\Delta T_b = \frac{1}{\sum k_b} \approx \frac{1}{K_{1,i-1} e^{\theta[i^{2/3}-(i-1)^{2/3}]} n_s M} \tag{2.20}$$

Thus, the final MC time step is given by:

$$\Delta T = \frac{1}{\frac{1}{\Delta T_f} + \frac{1}{\Delta T_b}} \tag{2.21}$$

Nucleation, a rare event:

Nucleation is a rare event that is difficult to capture numerically through direct brute force simulations [62]. For the condensation, it can be easily realized from the P_c distribution in Figure. 2.2 that indicate that larger clusters have higher probabilities of being sampled than smaller ones in the system. To avoid this stochastic bias towards the larger clusters in condensation events, one needs to account for their relatively lower concentrations in the system during the growth process. Thus, a cluster needs to have a relatively high probability (P_c) as well as concentration to grow successfully. To overcome such issues in our MC system, we define the probability of choosing a cluster size as:

$$P_{choose} = \frac{N_i}{M} \tag{2.22}$$

where N_i is the number of clusters with size i in the simulation box and M is the total number of clusters in the MC. Figure 2.2 depicts the distributions of P_c and P_{choose} assuming equilibrium cluster distributions. For any particular temperature and saturation ratio, P_c increases and P_{choose} decreases with increasing cluster sizes in the system. As an example, the relatively elevated concentrations of monomers result in them exhibiting the minimum values for P_c and maximum values for P_{choose} in the system. On the other hand, the maximum cluster sizes (i_{max}) in the system

have the lowest P_{choose}, alone with highly elevated values for P_c. To account for the role of P_{choose} in our KMC model, we employ the following sampling scheme for condensation events.

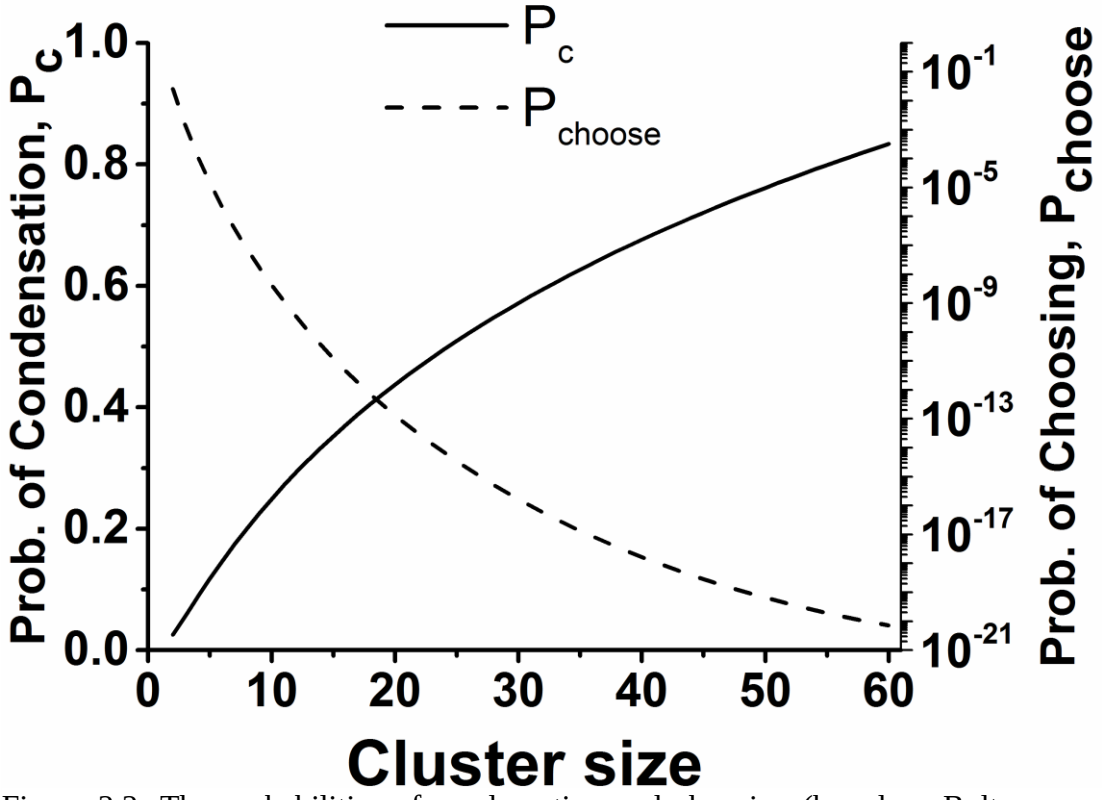

Figure 2.2: The probabilities of condensation and choosing (based on Boltzmann equilibrium distribution) as a function of cluster size.

Sampling scheme:

The sampling scheme is implemented in two steps: 1) identifying a "possible trial" and 2) comparing it to the "best trial". Identification of a "possible trial" is performed by randomly choosing two clusters, and then deciding on the success of the event by comparing its condensation probability (P_c) to a random number. If P_c is larger than the chosen random number ($P_c \geq \Re \in [0, 1]$), it is considered as a "possible trial" move. Otherwise, the system searches for another possible trial. To determine the "best trial" move, all existing growth paths in the system are considered and their probabilities of condensation (P_c) are calculated. Then, the probability of each path is

compared to a random number ($\Re$) to determine the paths that satisfy $P_c \geq \Re \in [0, 1]$. Among these paths, the path with the greatest P_c is identified as the "best trial" candidate. This random procedure for selecting the "best trial" ensures unbiased sampling in the system. Finally, we require the product of P_c and P_{choose} for the "possible trial" $(P_{choose}.P_c)^{possible}$ to be larger than the corresponding probability product for the "best trial" $(P_{choose}.P_c)^{best}$ in the system for a successful growth to proceed, that is:

$$(P_{choose}.P_c)^{best} \leq (P_{choose}.P_c)^{possible} \tag{2.23}$$

The algorithm flowchart and a schematic representation of the sampling technique are demonstrated in a step-wise fashion in Figures. 2.3 and 2.4 respectively. This strategy ensures that the acceptance of the growth reaction is not only based on the probability of condensation but also on the probability of choosing (driven by cluster concentrations).

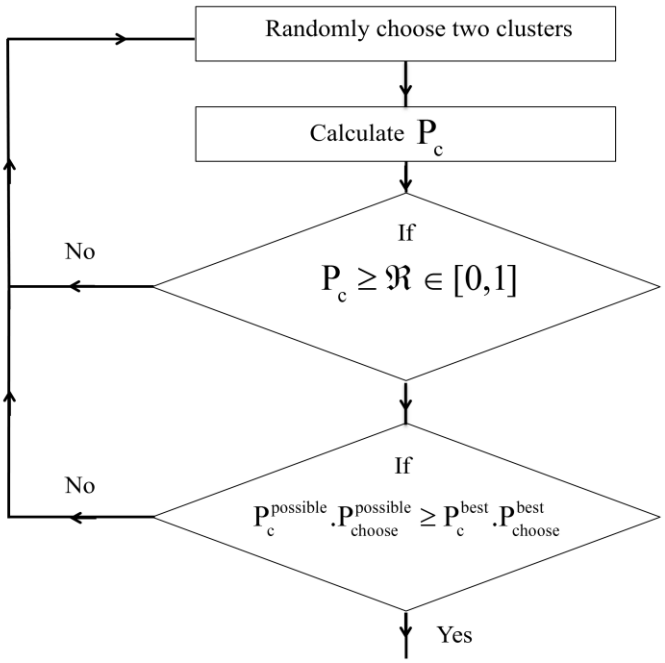

Figure 2.3: Schematic of the developed algorithm adopted for the current KMC model).

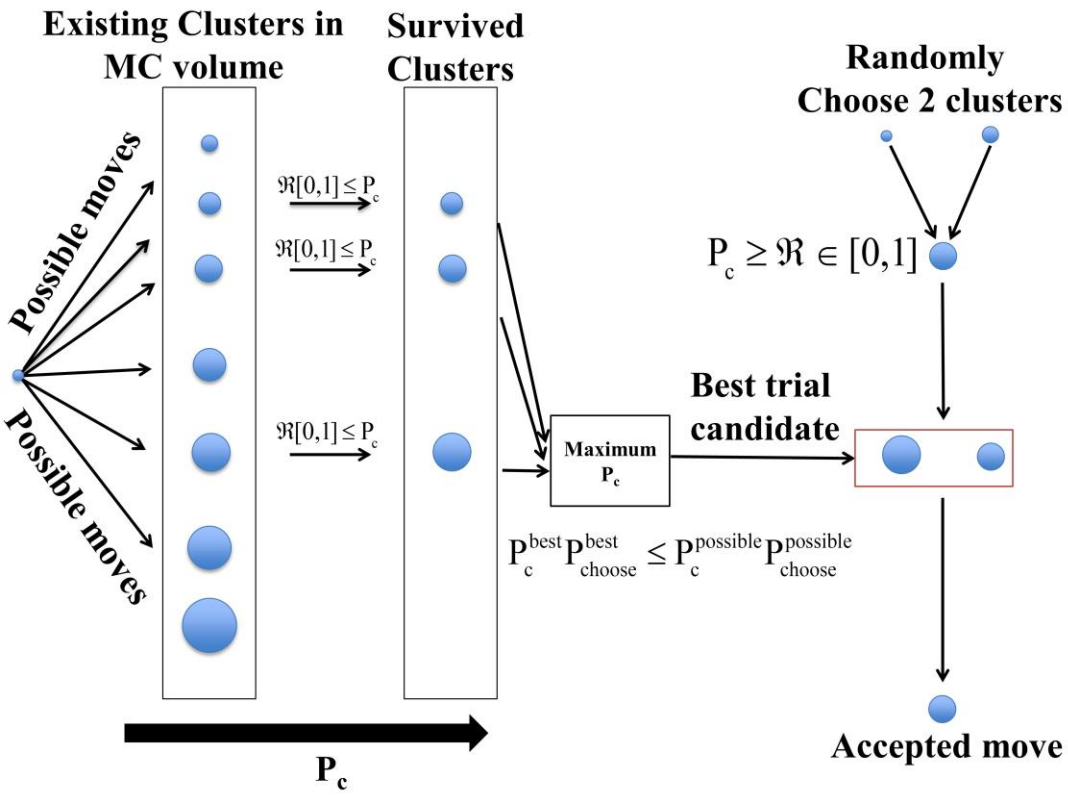

Figure 2.4: The schematic of the pseudo sampling technique employed for capturing rare nucleation event in the KMC model.

Also described earlier, the probability criteria for backward evaporation processes are accordingly derived from detailed balancing.

2.3 Results and discussion

The current KMC model specifically studies the vapor phase nucleation of Al NPs. The choice of Al NP stems from the growing interest in diverse applications of Al nanomaterials in semiconductors [63], nanocomposites [64, 65], and specifically, in energetic nanomaterials for solid-state combustion studies carried out by numerous earlier experiments [66-68] and simulations [69-71]. Table 2.1 shows the thermophysical properties of Al used for the simulations. The choice of Al NPs also enables the model validation via comparisons with previous phenomenological studies using Nodal General Dynamic Equation (NGDE) model [29] under

identical synthesis conditions (indicated as case (a) below). Additionally, we implement the model to simulate the process under two different initial conditions as depicted by cases (a) and (b) below.

Table 2-1. Thermophysical properties of Aluminum.

Properties	Value
Density, ρ [kg/m^3]	2700
Atomic mass unit, m [u]	27
Monomer volume, V_1 [m^3]	1.657×10^{-29}
Saturation vapor pressure, P_s [Pa]	$\exp(13.07 - \frac{36373}{T})P_g$*
Surface tension, σ [N/m]	$(948-(0.202 \times T_g) \times 10^{-3}$

*P_g: Pressure of gas medium [Pa]

Simulation jobs were run at the Newton cluster machines operated by the University of Tennessee. The machine consists of over 300 Linux compute nodes, 4,200 x86_64 architecture processors, and 8000 Gbytes of RAM with 48 of the compute nodes featuring Tesla GPU compute accelerators. Typical CPU run time for jobs run on one node with 10000 particles is ~2 hours, that can slightly change based on the type of processor that the machine decides to assign the job to. The following synthesis parameters are chosen for the simulation results presented in this study:

a) Initial temperature, T_0 = 1773K and cooling rate = 1000K/s.

b) Initial temperature, T_0 = 1973K and cooling rate = 1000K/s.

Model Verification:

The temporal evolution of ΔG_i^f as a function of cluster size is plotted for the representative case (a) in Figure 2.5. Initially, the saturation ratio in the system is approximately one (S~1). As seen from Figure 2.5, the initial nucleation barrier, as calculated from the CNT expression (eqn. 1), is extremely elevated. Thus, the chance of clusters surmounting this barrier is significantly low.

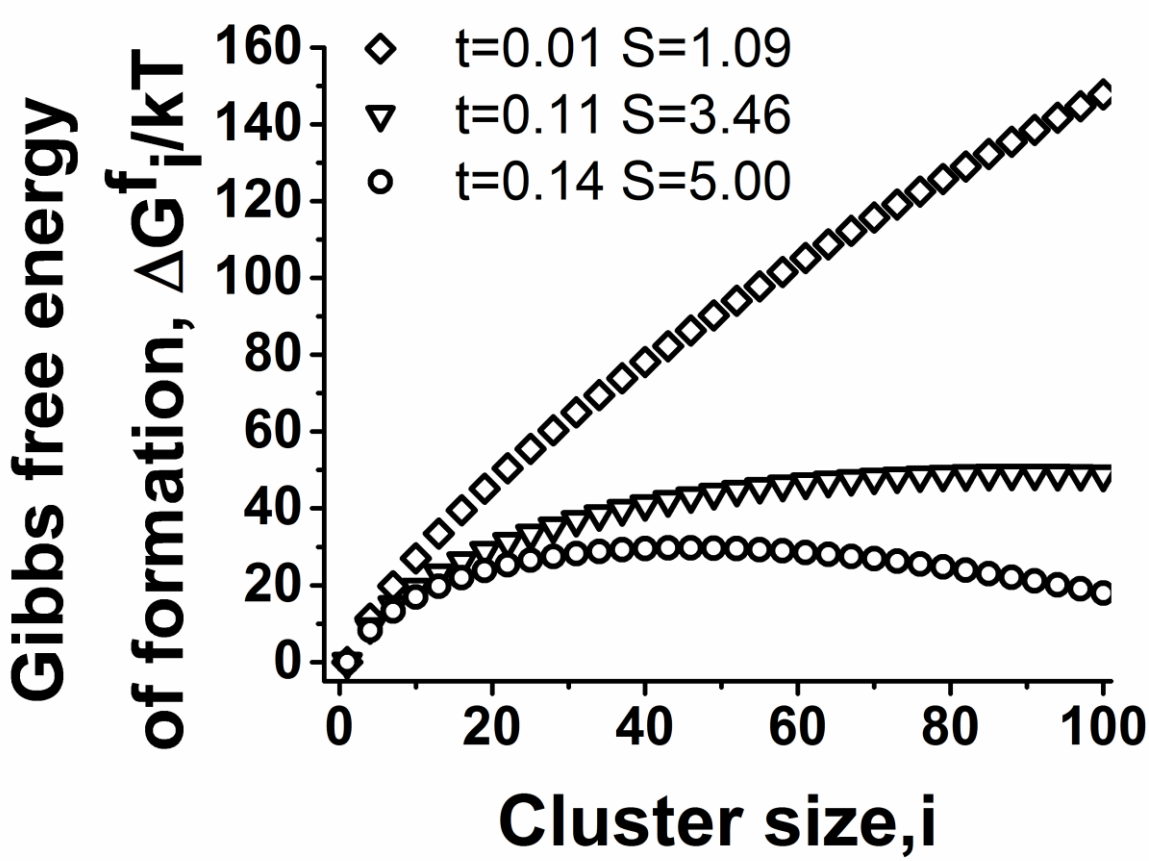

Figure 2.5: Temporal variation of the Gibbs free energy of formation with cluster size.

The nucleation barrier reduces over time as the background temperature (T) decreases and the saturation ratio (S) increases.

To verify the model, the temporal evolution of S and monomer concentrations (n_1, #/m^3) from the current KMC simulations, as depicted in Figures 2.6 (A) & (B) respectively, indicate good agreement with the corresponding results from previous NGDE simulations [29]. Due to high cluster evaporation rates in early stages, the KMC monomer concentration demonstrates a uniform and slow decay until the point of nucleation (Figure 2.6 (B)). This also corresponds to a steady increase in the saturation ratio from S~1 to S~5.4 at the onset of nucleation (t~0.145 sec). A negative Gibbs' free energy change for the evaporation reactions before the onset of nucleation ($\Delta G^{r}_{i-1,i} \leq 0$) results in the maximum evaporation probability (P_e=1 from eqn. (2.16)). Thus, a

majority of the generated clusters undergo enhanced evaporation leading to low cluster concentrations and minimal decay in monomer concentrations. Figures 2.6 (A) & (B) show a drastic drop in S and n_1 respectively at the onset of nucleation. This can be explained by the formation of a critical cluster with size i* as a new phase. The birth of the critical clusters initiates rapid consumption of monomers by condensation, and surface growth that leads to the formation of larger particles. Subsequently, the supersaturated vapor relaxes back to the saturated state (S~1) as the monomer vapor pressure equilibrates with the saturated vapor pressure on surfaces of the formed particle (Figure 2.6 (A)). It can be observed that the relaxation of S form the KMC model is slightly different as compared to that from NGDE. This can be related to the numerical diffusion involved in NGDE, especially when the nucleation outburst occurs and larger bins start to get occupied.

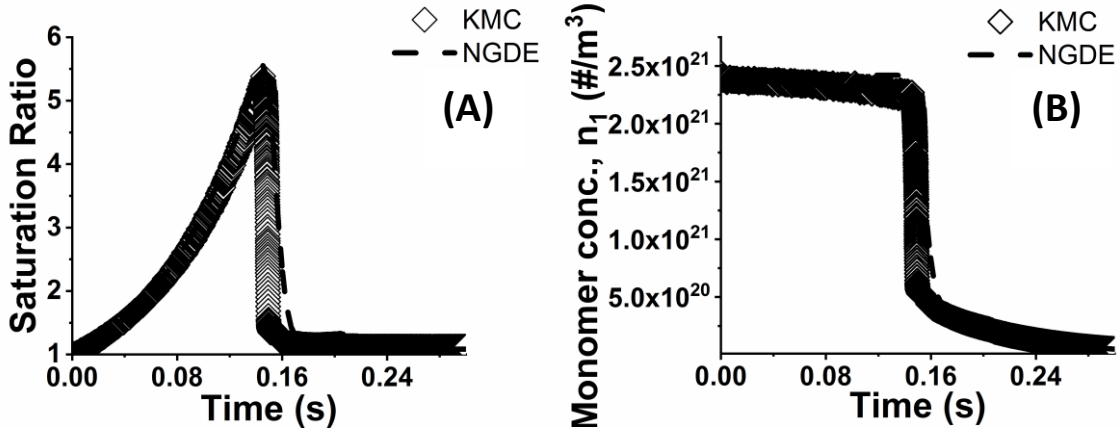

Figure 2.6: Temporal evolution of (A) saturation ratio S and (B) monomer concentration n_1 (#/m^3) for case T_0=1773 K.

The plots for P_{choose} and P_c as a function of cluster size in Figure 2.7 for case (a) at t=0.111s, 0.126s, and 0.14s indicate the inverse relations of P_c and P_{choose} with increasing cluster sizes which is characteristic of rare events. The qualitative trends in these characteristic variations have been corroborated earlier for theoretical P_{choose} and P_c values in Figure 2.2 under equilibrium size distribution considerations. This further supports our rationale behind the choice of P_{choose} as an

additional parameter in the sampling technique described earlier in the modeling section to account for the rarity of the nucleation event. In addition, higher S and lower T may result in the appearance of larger clusters with higher surface areas. This, in the presence of excess monomer concentrations, increases the likelihood of monomer condensation on clusters significantly. As the cluster sizes increase, the favorable bulk free energy difference due to chemical potential changes arising from phase transitions dominate over the unfavorable formation of an interface between the phases. Thus, the forward rates of the reaction R(1) is enhanced as the cluster sizes increase in the system. This phenomenon can be observed in Figure 2.7 where the P_c values increase rapidly as the cluster sizes in the system increase between t = 0.111 s and t = 0.14 s. Despite the qualitative similarities between the variations of P_c and P_{choose} in Figure 2.2 and Figure 2.7, a distinct quantitative difference is observed in the P_{choose} values for the larger clusters. The P_{choose} variations obtained from the KMC simulations (Figure 2.7) shows a well-defined plateau for larger cluster sizes as compared to the uniformly exponential decay in the equilibrium size distribution in Figure 2.2. Hence, Figure 2.8 compares the cluster concentration distributions for sizes $i < 10$ based on KMC simulations for case (a) at t = 0.111s with the corresponding equilibrium concentration distributions as depicted by eqn. (2.4) earlier. The comparison indicates that the deviations from equilibrium conditions are initiated as early as cluster sizes ranging between i = 4-8. Such observations indicate that while equilibrium size distributions can approximately predict the concentrations of smaller clusters, the prediction fails drastically for larger clusters. These larger clusters, ultimately, play a primary role in formation of critical clusters when the process approaches the onset of nucleation burst. Similar results have also been observed in cluster size distributions from MD simulations [72, 73], as discussed extensively in the following section.

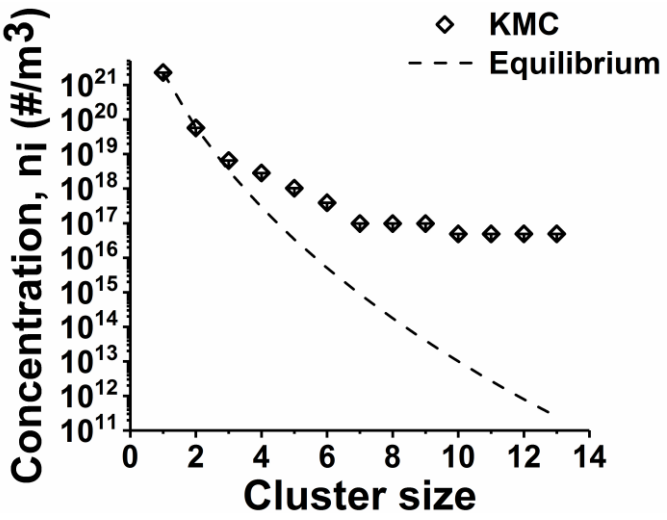

Figure 2.7: Cluster size distribution for i<15 showing deviation from equilibrium size distribution for case T_0=1773 K at t=0.11s.

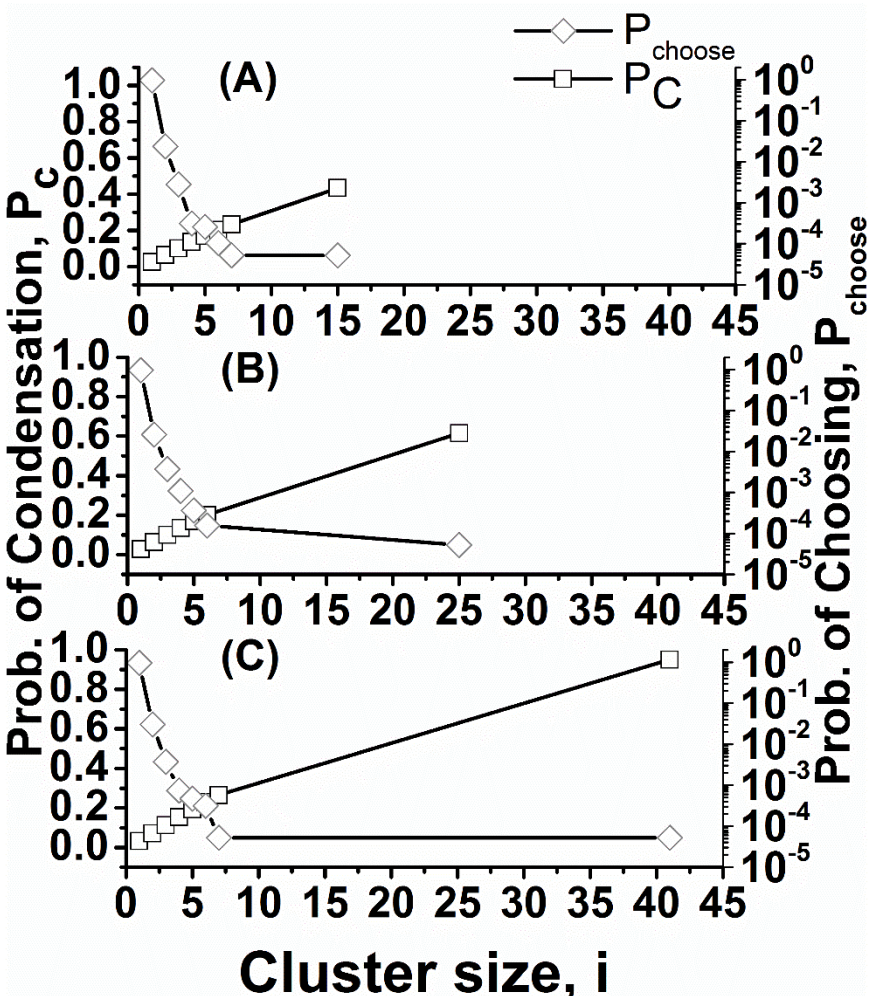

Figure 2.8: Probabilities of condensation (P_c) and choosing (P_{choose}) for case T_0=1773 K at (A) t=0.111s, (B) t=0.126s and (C) t=0.14

Nucleation Rate: A Discussion

The nucleation rate for cluster size of i (Ji) is defined as the net rate of transition from size i to the next size (i+1). In order to calculate the nucleation rates from our current KMC simulations, we employ two different methods commonly adopted in earlier MD simulations: 1) Yasuoka-Matsumoto (YM) method, and 2) mean first passage time (MFPT) method.

Yasuoka-Matsumoto method:

This method, introduced by Yasuoka et al. [73] was implemented in their MD simulations on Lennard-Jones fluid. In that study, the numbers of clusters equal or above a certain size threshold were counted and nucleation rates were estimated based on the slopes of the number of counts over time. Figures 2.9 (A) & (B) illustrate the nucleation rates $\langle J_i \rangle$ for various cluster sizes (i = 2,3,5 in (A) and i = 10, 15, 20 in (B)) as a function of time generated from our KMC simulations based on the YM method.

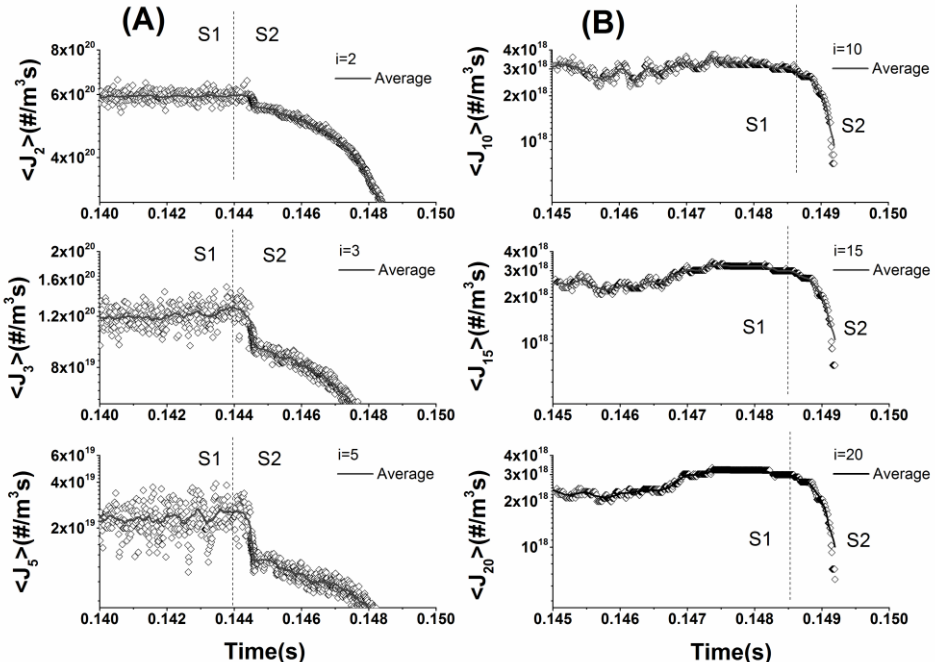

Figure 2.9: Nucleation rates $\langle J_i \rangle$ for (A) i=2, 3, 5 and (B) i= 10, 15, 20 as a function of time for case T_0=1773 K.

Two distinct stages, S1 and S2 can be observed as it was also shown by Yasuoka *et al*'s work. It is evident from Figure 2.9 (A) that the $<J_i>$ for i = 2-5 indicate relatively high values that diminish with increasing cluster sizes (i.e., $<J_2>$~5.9 x 10^{20} #/m^3.s and $<J_5>$~2.5 x 10^{19} #/m^3.s) in stage S1 up to t ~ 0.144 s. Additionally, the $<J_i>$ values decay rapidly in stage S2 beyond t = 0.144 – 0.145 s. In contrast, the $<J_i>$ for cluster sizes i = 10-20 in Figure 2.9 (B) show lower values than those observed for i=2-5, while no significant change in nucleation rates is observed for the increasing cluster sizes. The $<J_i>$ values decay rapidly beyond t ~ 0.1485-0.149 s in stage S2, that also marks the onset of nucleation.

It suggests that although in stage S1 significant numbers of clusters are formed with sizes smaller than the threshold value (i < 10), only clusters larger than the threshold value (i ≥ 10) are able to grow through this stage and up to the nucleation outburst. To provide a detailed insight, Figure 2.10 shows that nucleation rates for smaller clusters (i = 2-9) are significantly higher than those for the larger ones (i ≥ 10), and they decay to a lower but unified value for the larger clusters.

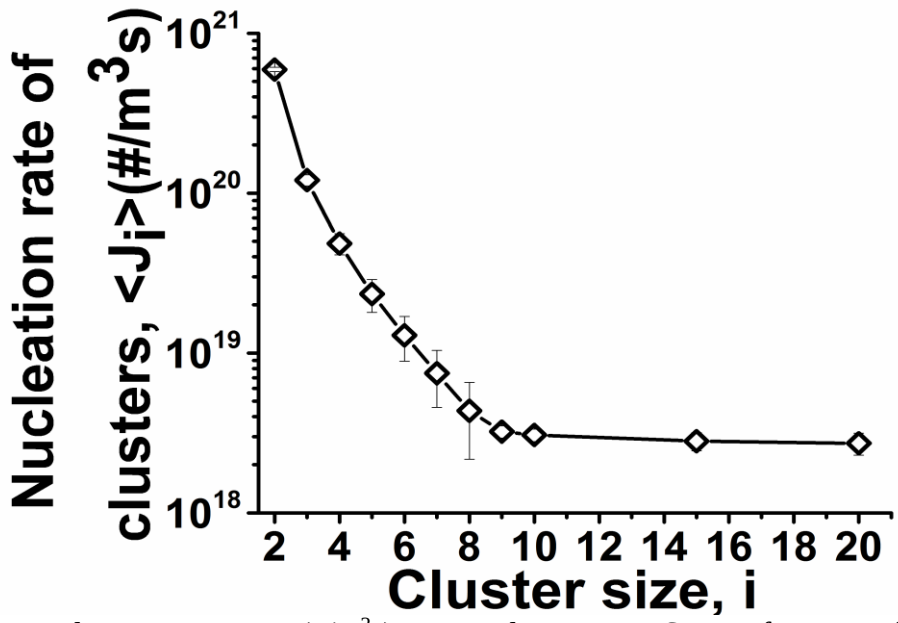

Figure 2.10: Nucleation rates $<J_i>$ (#/m^3s) averaged over stage S1 as a function of cluster size for case T_0=1773 K.

Therefore, the KMC-based nucleation rate for cluster sizes ≥ 10 are estimated to be J_{KMC}=2.7 x 10^{18} (#/m^3.s). Comparing this result to the theoretical CNT-derived value of J_{CNT}=1.81 x 10^{14} (#/m^3.s), we observe almost 4 orders of magnitude differences between the two nucleation rates.

Mean first passage time method (MFPT):

Mean first passage time method has been extensively studied in literature for calculating nucleation rates [62, 74, 75]. The method analyzes the time required for a cluster to reach to a particular size for the first time. By tracking the maximum cluster size of the system over time the nucleation rate can be obtained. It has been shown that in presence of nucleation barrier, the required time for maximum cluster size to reach a particular size is given by [75]:

$$\tau(i) = \frac{\tau_J}{2}[1 + \mathrm{erf}(b(i - i^*))] \tag{2.24}$$

where "erf" represents error function, and b is related to the Zeldovich factor: $Z = \frac{b}{\sqrt{\pi}}$. Using a curve fit to the direct simulation results, it is possible to obtain critical cluster size and nucleation time. Finally, the nucleation rate can be calculated as:

$$J_{KMC} = \frac{1}{V\tau_J} \tag{2.25}$$

where τ_J is obtained from curve fit and V is the MC volume. Figure 2.11 shows the MFPT curve obtained from tracking the evolution of maximum cluster size in our KMC system run for the case study (a). It can be observed that the data has a sigmoidal shape and represents a well-defined plateau. Therefore, the nucleation rate obtained from MFPT is estimated to be J_{KMC}=3.7 x 10^{18} ± 3.8 x 10^{16}.

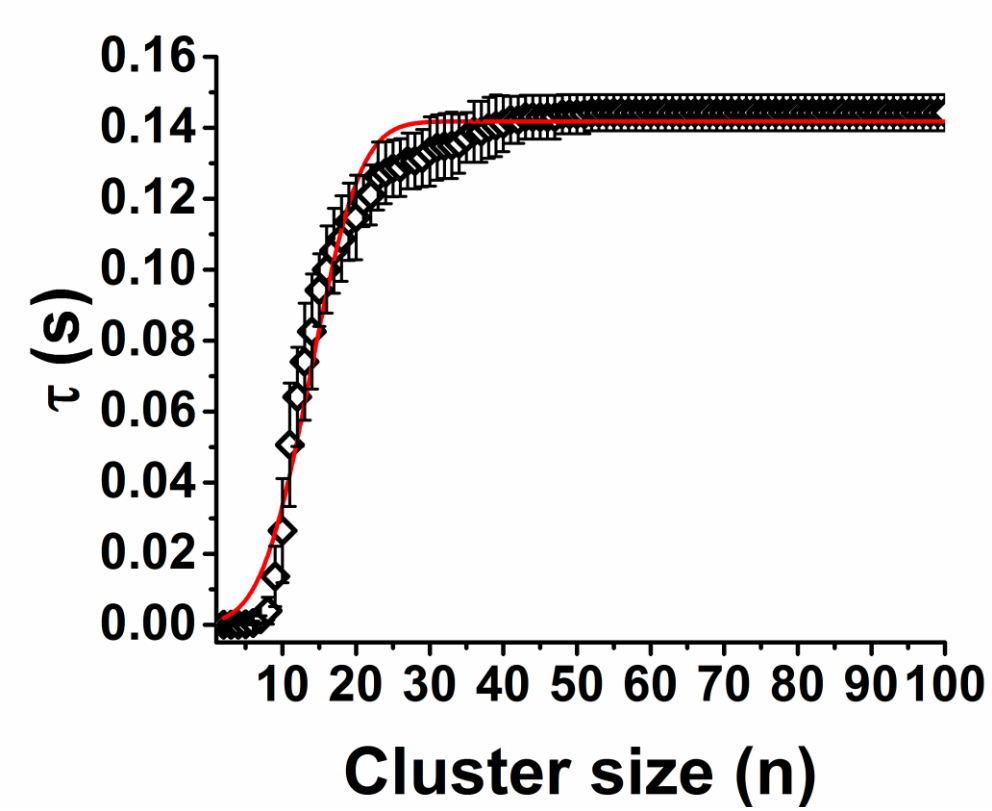

Figure 2.11: Mean first passage time analysis for case T_0=1773 K.

From eqn. (2.25) it can be realized that the nucleation rate depends on the nucleation time (τ_J) and the error is calculated based on the error in the nucleation time. By comparison, there is a good agreement between the nucleation rates obtained by YM and MFPT methods.

Effect of initial temperature:

The KMC model is used to investigate the effect of initial background temperature on the nucleation process for two different values: T_0 = 1773K, and 1973K. Figure 2.12 shows the evolution of saturation ratios as a function of reduced temperature (defined as the instantaneous system temperature T normalized by the initial temperature T_0). As the T_0 values for the nucleating system are increased, the nucleation process is accelerated. Thus, the maximum saturation ratio is decreased from S=5.4 in case (a) to S=2.7 in case (b) and subsequently earlier onset of nucleation is resulted.

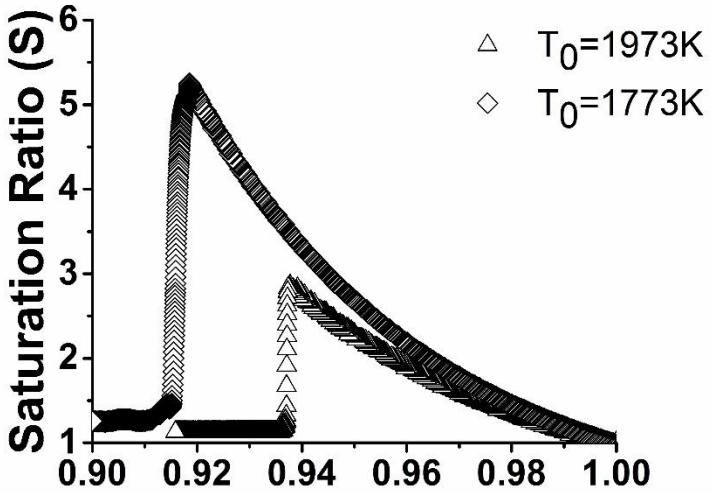

Figure 2.12: Saturation ratio (S) as a function of reduced temperature (T/T0) for cases T0=1773K and 1973K.

Figure 2.13 shows the critical cluster sizes of i* = 43 (~1 nm) for case (a) as compared to i*= 105 (~ 2 nm) for case (b). Thus, a reduction of the initial system temperature assists in the formation of smaller primary particles. Furthermore, larger fluctuations in the i_{max} values are also observed for higher initial temperature in case (b) (i.e., T_0 = 1973K in Figure 2.13 (A)). Analyzing these fluctuations, Figure 2.13 (A) for T_0 = 1973K shows a wide and uniform variance over time, as compared to Figure 2.13 (B) for T_0 = 1773K where the variance is initially narrow for T/T_0~1 but increases over time demonstrating a non-uniform trend. This implies that for T_0 = 1973K, the i_{max} in the system can attain larger values in the earlier stages as compared to the corresponding i_{max} values for T_0 = 1773K case. Moreover, for higher T_0 values the maximum cluster size in the system has a higher probability to grow and survive in spite of the high evaporation rates. To analyze these fluctuations in the nucleating systems, the Gibbs' entropy of mixing is calculated based on the probability distribution over cluster sizes as:

$$\mathscr{S} = -k_B M \sum_{i=1}^{i=i_{max}} \frac{N_i}{M} \ln\left(\frac{N_i}{M}\right) = -k_B M \sum_i P_{choose} \ln(P_{choose}) \qquad (2.26)$$

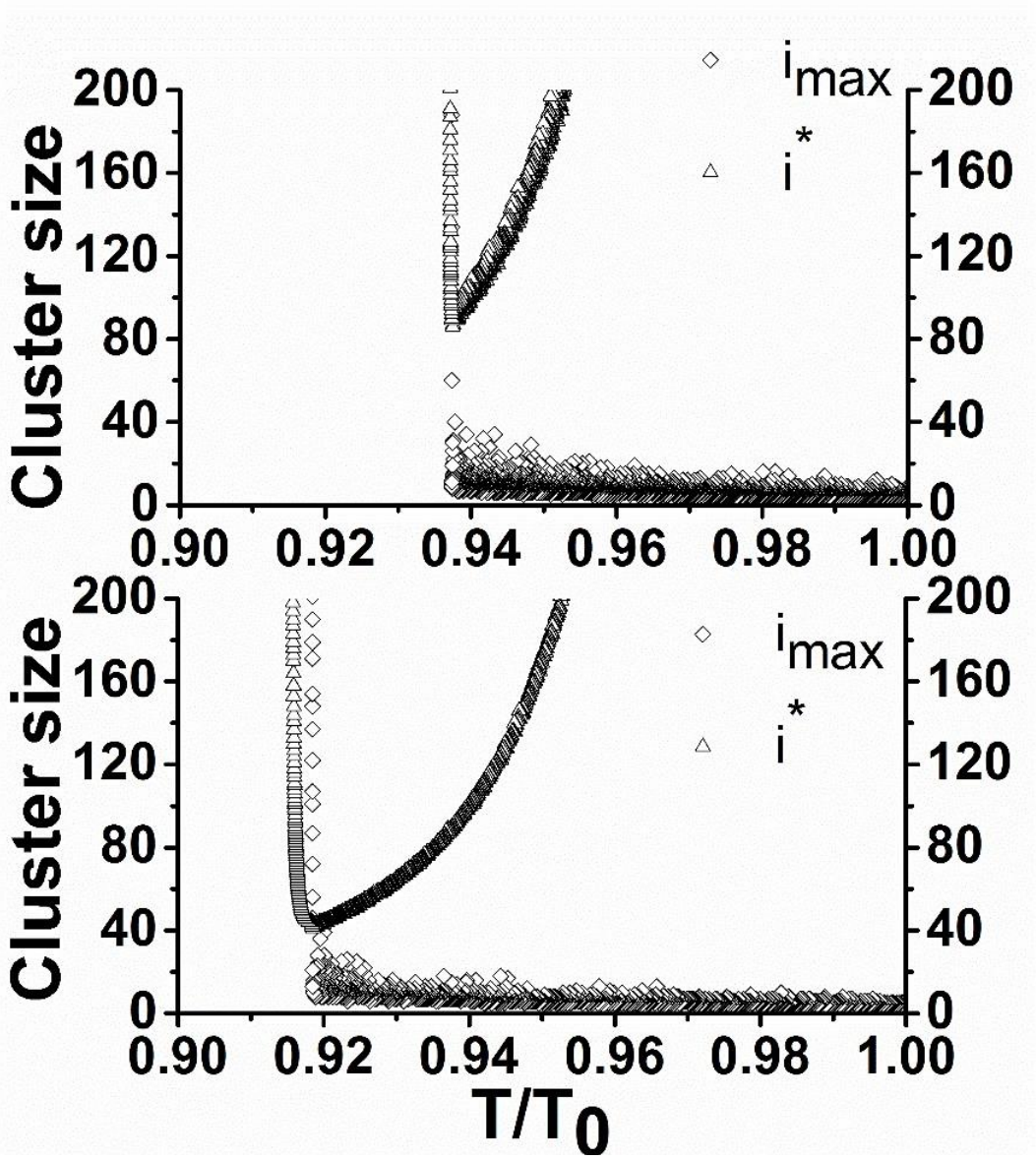

Figure 2.13: Variation of maximum cluster size (imax) and critical cluster size (i*) in the system as a function of reduced temperature (T/T0) for case (A) T0=1973K and (B) T0=1773K.

For further clarification, eqn. (2.26) represents the system entropy of mixing where different cluster sizes are considered as independent entities, and clusters within each size are identical. At each time step, the state of the system is determined by the cluster size distributions and the corresponding system temperature. Appearance of other cluster sizes increases the disorder, and consequently the entropy of mixing in the system. Clusters that cross the nucleation barrier form a more organized phase and hence, the entropy of mixing in the system should ideally decrease. These phenomena are clearly depicted by Figure 2.14 where the entropies for case (a) (T_0 = 1773 K) and case (b) (T_0 =1973 K) are plotted as a function of the reduced temperatures (T/T_0). As expected, the higher entropy of mixing along with the large variabilities and spread in the entropy data as seen in case (b) indicate higher disorder and fluctuations in the system as compared to the case (a). These disorders and fluctuations cause a number of larger clusters to survive during the cluster evaporation that go on to attain the critical cluster size by crossing the nucleation barrier.

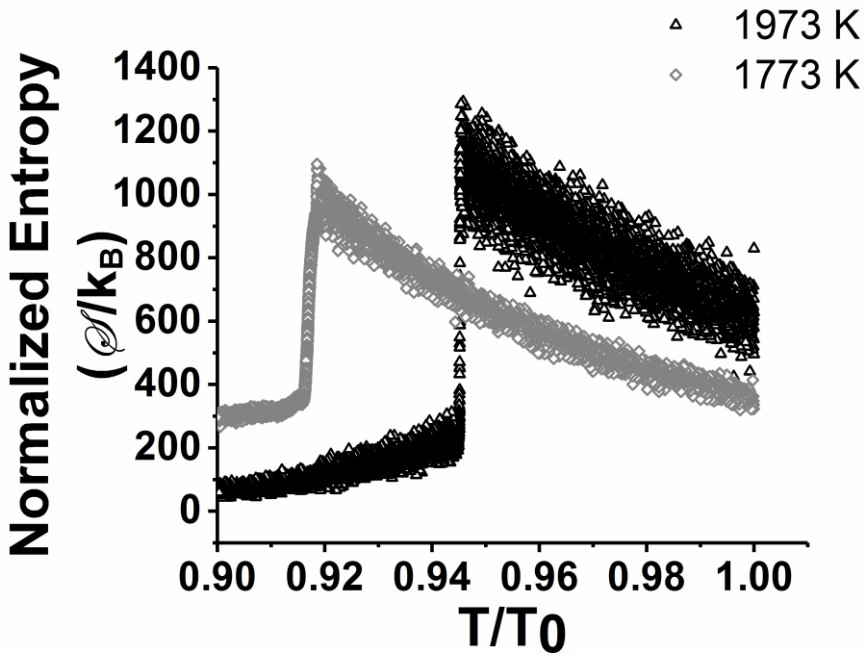

Figure 2.14: Evolution of normalized entropy ($\mathscr{S}/k_B$) as a function of reduced temperature (T/T_0) for cases T_0=1773K and 1973K.

They initiate the nucleation process. A comparison of the cases (a) and (b) in Figure 2.14 reveals that higher fluctuations in case (b) result in an earlier outburst of nucleation.

2.4 Conclusion

We have developed a hi-fidelity Gibbs' free energy driven KMC model to simulate homogeneous nucleation of metal NP's. The model captures the ensemble stochastic processes of monomer-cluster (condensation), cluster-cluster collisions, as well as cluster evaporations via detailed balancing during gas phase synthesis process. A novel and statistically unbiased pseudo sampling technique has been proposed to effectively address the computational challenges of capturing the rare and non-equilibrium nature of nucleation events in a time-efficient manner. The simulation results from the current KMC model indicate good agreement with previously obtained results from phenomenological models for similar case-studies [29, 49]. Our results indicated that the onset of nucleation outburst is accelerated by increasing the initial vapor temperature (T0) resulting in the formation of critical clusters with sizes ~ 1 nm and 2 nm for T0 = 1773 K and 1973 K respectively.

Nucleation rates calculated by the YM method indicate higher values for cluster sizes smaller than a threshold value ($i \leq 10$), above which the rates drop off to a relatively lower but unified value. The nucleation rates obtained from YM method compared well with that from MFPT method, while being almost 4 orders of magnitude larger than the CNT steady-state value. The variations in the ensemble entropy of mixing indicated an increasing trend in the system leading up to the onset of nucleation where it eventually undergoes the expected drastic loss due to the emergence of a more organized new nanophase. The current work paves the path for our future introduction of more accurate cluster size-dependent free energy formulations into our current nucleation model. Such a robust model development will facilitate the easy and unified incorporation of the

nucleation process into our previously developed KMC-based collision-coalescence [59] and morphology-driven surface oxidation models [69] that can investigate the impact of nucleating critical cluster sizes on the general dynamics of NP growth and evolution without any capillarity and/or, isothermal assumptions.

Chapter 3 Laser Ablation Synthesis in Solution (LASiS): A Facile Technique for the Synthesis of Energetic Nanoparticles

This chapter is based on the following publications:

- Mukherjee D., **Davari S.A.** (2017) Computational Modeling for Fate, Transport and Evolution of Energetic Metal Nanoparticles Grown via Aerosol Route. In: Shukla M., Boddu V., Steevens J., Damavarapu R., Leszczynski J. (eds) Energetic Materials. Challenges and Advances in Computational Chemistry and Physics, vol 25. Springer, Cham

- **Davari S.A.**, Gottfried J., Tian M., Ribeiro E. L., Duscher G., Mukherjee D. "Synthesis of graphite coated Aluminum nanoparticles using laser ablation in organic solutions", in prep.

3.1 Introduction

The last few decades have seen a large volume of research work focus on a class of novel materials that demonstrate enhanced energetic property and reactivity thereby finding application in the development of propellants, explosives and pyrotechnics. To this end, past studies involving various forms of aluminized solid propellants prepared with different mixtures of aluminum powders and oxidizers as heterogeneous, composite solid propellants have indicated high burning rates and enhanced ignition [76-80]. A substantially larger surface area arising from fuel-oxidizer interfaces in nanoscale regime promote kinetically controlled ignition processes. In this regard, the first generation of energetic nanomaterials had increasingly invested in research efforts towards the use of nanoaluminum in explosives [81-83]. Rational design and synthesis of metal (fuel) nanoparticles with tailored size, morphology and compositions play a pivotal role in tuning the reactivity of these classes of nanomaterials with high accuracy. Moreover, usually the structures at these length scales are unbalanced and metastable due to their fast formation during manufacturing processes. Thus, while existing in their metastable state for long times under normal

conditions, any perturbations sufficient enough for structural changes may result in the release of excess energy in the form of heat in an effort to relax to stable structural arrangements. Traditionally, Aluminum (Al) with its large enthalpy of combustion (~1675 kJ/mol for bulk Al) has always been considered in the class of solid-state propellants and explosives [84]. But, considering that the enthalpy of combustion of an isolated Al atom is ~ 2324 kJ/mol and the aforementioned interfacial energetic properties at nanoscale, nano-Al has been the center of attention in energetic nanomaterials till recently. To this end, one of the first methods proposed for the production of nano-Al was based on the condensation of metal vapors generated by explosion of electrically induced wire [85]. Sol-gel approach has been employed by researchers at Lawrence Livermore National Lab for the synthesis Al/Fe2O3 for the first time [86]. The lab-scale and industrial synthesis of metal nanoparticles typically employ rapid condensation of supersaturated metal vapor (monomer) that are generated from thermal evaporation of the bulk metal, electric arc discharge, laser ablation, flame reactors, plasma reactors, etc. During these gas-phase synthesis processes, rapid cooling (~10^3-10^5 K/s) of the metal vapor initiates the saturated vapor to undergo the free-energy driven collisional process that finally leads to nucleation and the birth of a stable cluster. This critical cluster subsequently grows via coagulation/coalescence and undergoes various interfacial reactions. The thermodynamics and kinetics of each of the aforementioned events during the vapor-phase production of nanoparticles play significant role in tailoring their sizes, morphology, composition and structure. In fact, it soon became apparent that a significant drawback of the gas-phase synthesis routes for these metal nanoparticles was in the kinetics of the process leading to high collision-calescence rates of the particles that resulted in rapid aggregation. And the very energetic behaviors in these materials being largely driven by their excess interfacial

area and small diffusion length scales, such large-scale aggregation led to rapid loss of surface area and activity for these nanomaterials.

On the other hand, in relation to the reaction kinetics and the oxidation mechanism in these metal nanoparticles, the conventional wisdom called for stoichiometric mixing of the fuel and oxidizer to maximize their energy density. But, the overall kinetics of the process demands an atomistic mixture of the two components to minimize the fuel-oxidizer diffusion length during the reaction. Thus, for larger particle grain size, and hence lower interfacial area between the oxidizer and fuel, the overall reaction speed reflects mass-transfer limitations. Additionally, the diffusion length being exceedingly small in the nanoscale regime, the reaction rates are further increased by many orders of magnitude as compared to those the bulk state. For a better understanding, the evolution of Al particles during oxidation is needed. The Al oxidation and its energy release can be described by few mechanisms related to the transport of species and surface reactions:

1-Reaction between O2 and Al

2-Formation of oxide layer

3-Diffusion of O2 and Al through the oxide layer for further reaction

It has been shown that the morphology of the particles, especially the oxide layer thickness changes the energetic properties of Al nanoparticles drastically [69]. Any unwanted oxide layer such as native oxide layer would affect the surface reactivity of the Al nanoparticles significantly.

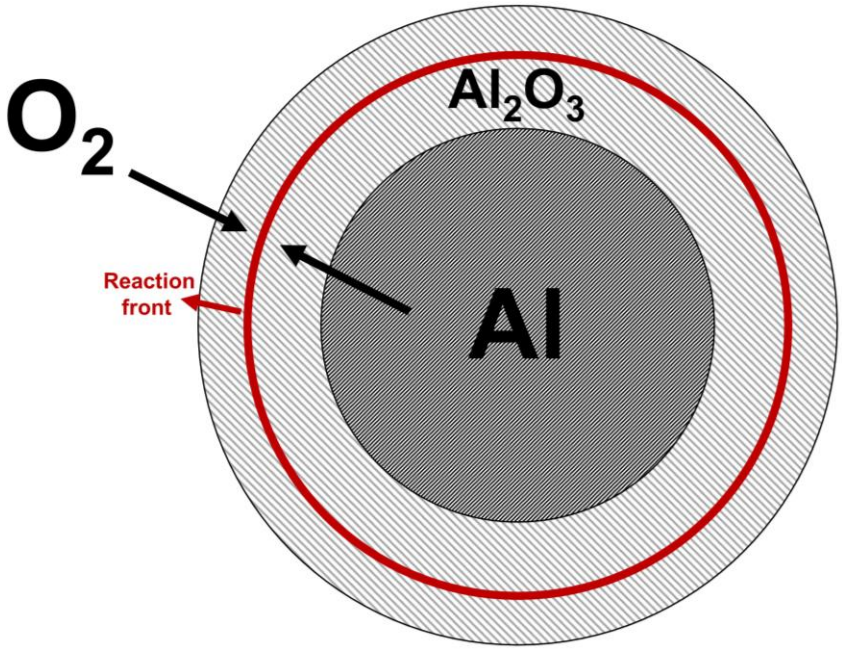

Figure 3.1: Schematic of oxidation mechanism of Al nanoparticles.

Therefore, it could be both beneficial and detrimental to the design of these energetic nanoparticles either in the use of the optimal oxide shell to passivate the Al nanoparticle surface for safety reasons or to tune their surface oxidation rates. Increasing research efforts in the design of next-generation energetic nanomaterials have been directed towards the basic idea that the coatings should not retard the activity, but promote safety while enabling to, in fact, further enhance their performances. Hence, various scenarios have been suggested to preserve the surface activities using noble metals [87] and metal oxides [88]. Carbon coatings have been demonstrated to show similar features [89] so that while the coating itself can be oxidized into gaseous products, they also retard the particle aggregation rates due to the presence of the carbon shell. To this end, various techniques such as plasma-enhanced chemical vapor deposition (PECVD) [90], photopolymerization [91] and wet chemistry [92].

While chemical synthesis routes are powerful and have been extensively used till date, they inevitably suffer from residual chemical contaminations and equilibrium growth pathways for the

particles in the absence of unwanted surfactants and ligands during the synthesis [15]. In this regard, laser ablation synthesis in solutions (LASiS) has been considered as a "green chemistry" route that can prevent the use of surfactants and residues from the reducing agents that typically poisons the active surface areas [10, 11]. Moreover, from the industrial perspective this technique is more economical for facile, rapid and large-scale production as compared to wet chemistry techniques [15]. Typically in LASiS, a target is immersed into a solution and irradiated with high-energy laser beam. The laser ablates the target and creates a local plasma with high pressure and temperature sufficient for triggering nucleation and subsequent growth of nanoparticles. By tuning the laser energy, wavelength, target metals of choice, solution chemistry etc. various nanostructures are obtained with different size, morphology and chemical compositions [17]. To this end, laser ablation has been employed in the past for production of Al nanoparticles [93]. A few studies have looked into the size and morphology of Al nanoparticles made from Al target ablation in organic solution [94, 95]. But, they fail to address the uncertainties in the size, morphology and structure of the Al nanoparticles thereby not enabling them to develop into reliable and tunable systems that can tailor the surface functionalities of these nanoparticle effectively. In fact, a vast majority of these studies have largely focused on the mere synthesis of these materials, and have failed to provide any comprehensive investigations into the energetic and other surface functional activities of these materials.

In this chapter, we focus on the synthesis of Al nanoparticles coated with carbon shells by using LASiS in various organic solutions and using different laser properties. The size/morphology, interfacial structures and compositions of the shell-core Al nanoparticles will be analyzed in light of their energetic activities when compared to each other as well as with commercial micron size Al powders and other well-known energetic materials.

3.2 Experimental set-up and procedure

3.2.1 LASiS Set-up

The LASiS experimental set-up is illustrated in Figure 3.2. A Q-switched Nd-YAG pulsed laser operating at 1064 nm with 4 ns pulse width, 10 Hz repetition rate and maximum energy 330 mJ/pulse is used for ablating the target in the cell. The cell is provided with two side-viewing windows to monitor and adjust the laser focal point. A gas inlet and outlet on the cell allows for suitable purging with inert gases if needed. The Al target is mounted on a stepper motor and rotates continuously to enable uniform ablation from the surface. The reactor cell is also provided with heating rods along with a thermocouple for accurate monitoring of solution temperature and a sonic dismembrator for in situ de-agglomeration of the synthesized NPs. Additionally, a programmable injection unit is attached to the cell that allows for simultaneous introduction of solutions for chemical reaction incorporation.

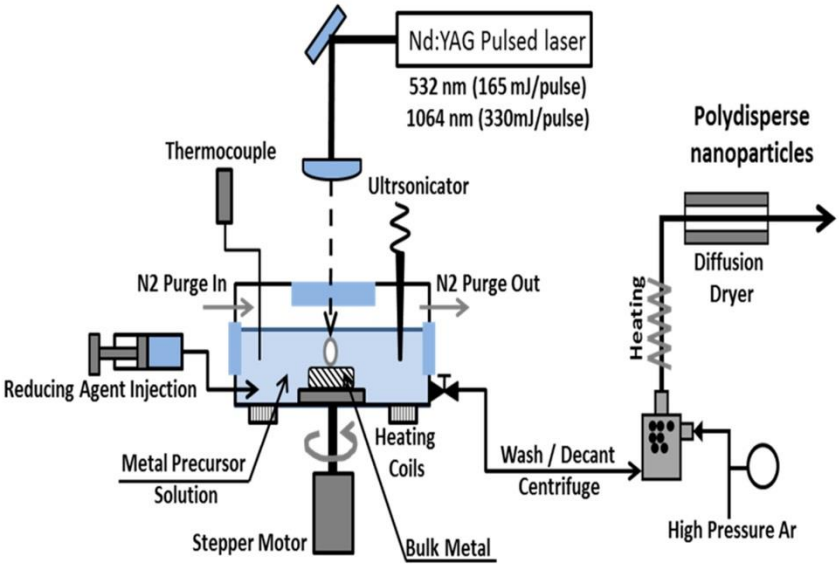

Figure 3.2: Schematic of LASiS set-up.

3.2.2 Synthesis of Al nanoparticles

The Al pellet was bought from Kurt J. Lesker (99.99% purity, 1" diameter and 1/4" height) and immersed into organic solvents. Two different organic solvents were used in this study for ablation of Al in solution. Both acetone (99.95% purity) and toluene (99.9% purity) were bought from Sigma-Aldrich. Al target was placed in ~ 8 ml of organic solvents and ablated for 4 min at room temperature. For all the experiments the original laser beam was used (~ 4 mm diameter) and laser energy was set to 330 mJ/pulse.

3.2.3 Characterization techniques

3.2.3.1 Laser-induced air shock from energetic materials (LASEM)

Recently a new technique similar to laser-induced shock wave and blast wave has been developed at our collaborator, US Army Research Laboratory (ARL) facilities at Aberdeen Proving Ground, MD for measuring energetic properties of exothermic and explosive materials [96-98]. Briefly, a shock wave is generated in air using laser-induced plasma on the surface of energetic materials. Through tracking the subsequent expansion of the ablated materials using schlieren and shadowgraph techniques the velocity of the laser-induced shock wave is measured and correlated to the blast wave velocity and pressure. In this chapter, all energetic property analyses for the as-synthesized nanoparticles have been carried out by laser-induced air shock from energetic materials (LASEM) at the US ARL facilities.

3.3 Results and discussion

Figure 3.3 illustrates the STEM images of the Al pellets ablated for 4 min in acetone and toluene at laser fluence of 2.6 J/cm^2. The samples were centrifuged and washed with methanol prior deposition on the grid for imaging. It can be observed the samples are comprised of nanoparticles embedded in a carbon matrix in both cases.

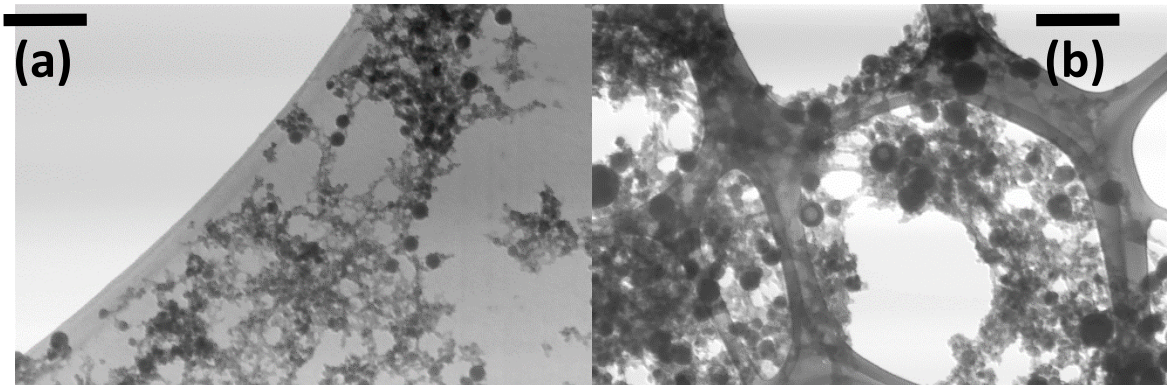

Figure 3.3: STEM images of Al target ablated in (a) acetone and (b) toluene for 4 min under 2.6 J/cm^2 laser flux. The bars correspond to 100 nm.

The ablation in toluene resulted in larger particles in comparison to the ablation in acetone. To confirm the observation, the particle size distribution for both cases were analyzed. To this end Figure 3.4 shows the size distribution of the particles synthesized in acetone and toluene under 2.6 J/cm^2 laser fluence. Both samples indicating a lognormal distribution. Based on the size distribution, it can be observed that the synthesized sample in acetone shows a unimodal distribution with the peak value at 15.7 ± 0.2 nm. On the other hand, the sample synthesized in toluene indicates a bimodal distribution with a peak at 25 ± 0.8 nm and another at 77.2 ± 1.7 nm. In this regard, the effect of ablation time on the particles size distribution has been carried out in toluene.

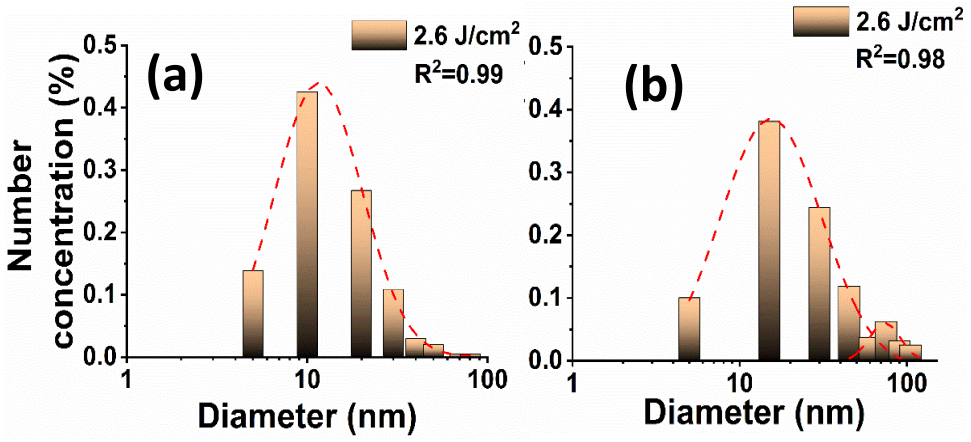

Figure 3.4: Size distribution of Al target ablated in (a) acetone and (b) toluene for 4 min.

Figure 3.5 shows the particle size distribution of Al pellets ablated in toluene for 2, 4, 6, and 8 mins. The size distribution seems to shift from unimodal (or biomodal with an insignificant second peak) with a relatively narrow full width half maximum (FWHM) at 2 min to almost unimodal at 8 min with a large spread for the FWHM. The observation indicates that as the ablation time increases, the difference between the first and second peaks in terms of the modal size and concentration decreases, while the particles systematically shift to larger sizes. Further investigations have been carried out on the effect of laser fluence on the particles size distributions. Figure 3.6 illustrates the particle size distributions from Al targets ablated in acetone and toluene at 2.6 and 10.5 J/cm^2 laser influences for 4 min. It is observed that as the laser fluence increases, the nanoparticle sizes become smaller.

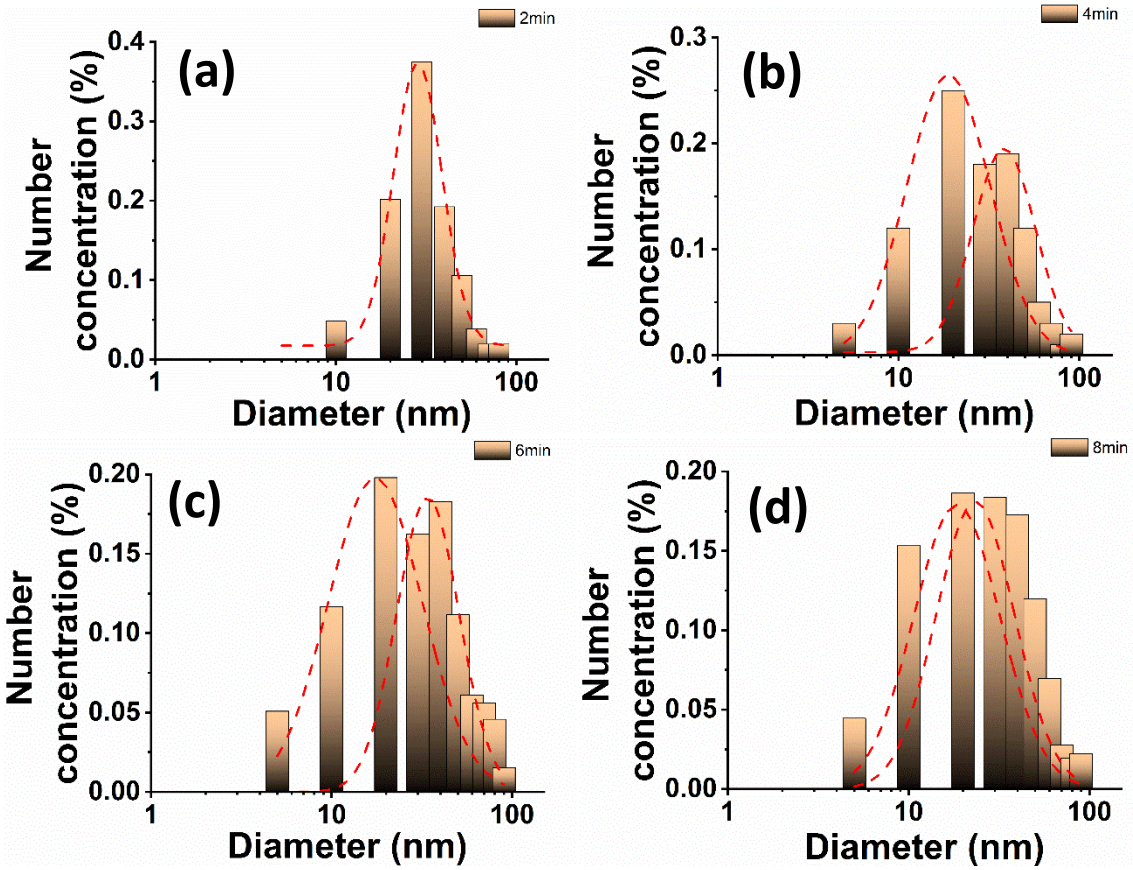

Figure 3.5: Size distribution of Al target ablated in toluene for (a) 2min, (b) 4min, (c) 6min and (d) 8min.

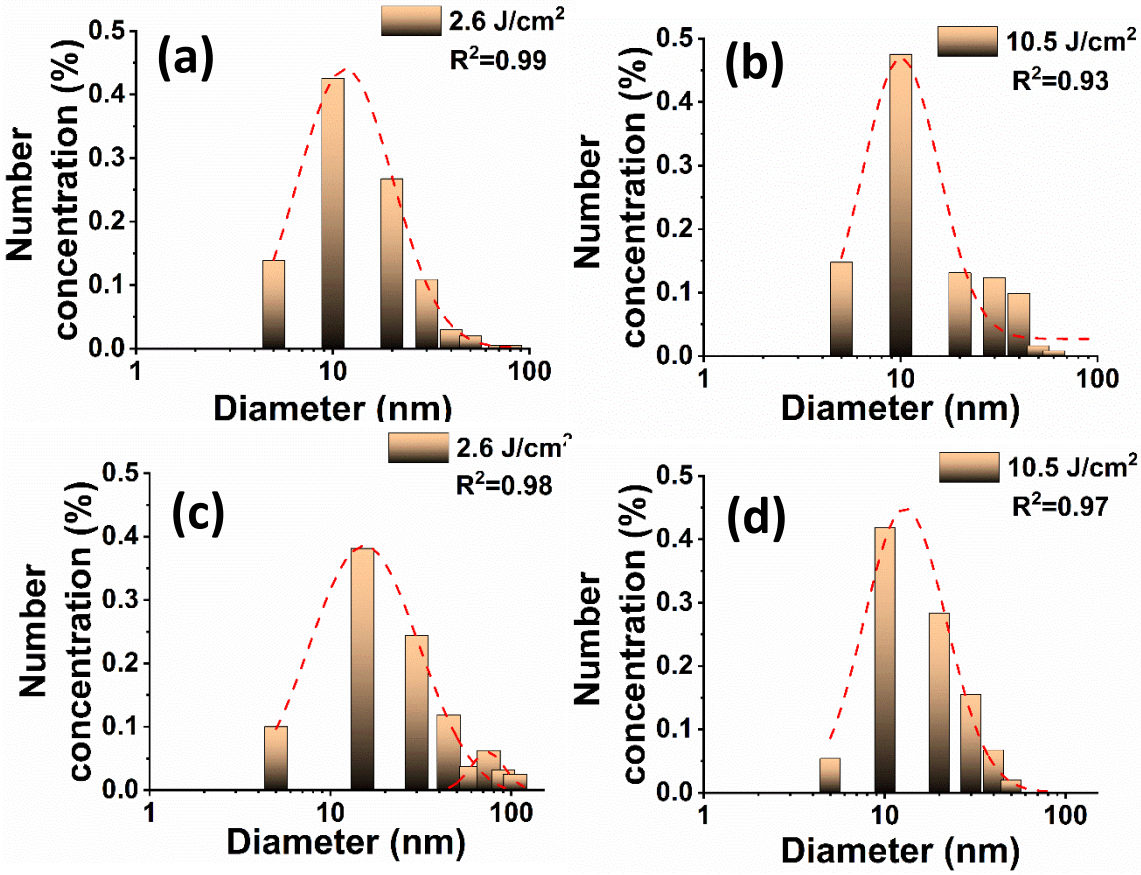

Figure 3.6: Effect of laser flux on the size distribution of Al target ablated for 4 min in acetone at (a) 2.6 J/cm^2, (b) 10.5 J/cm^2, and in toluene at (c) 2.6 J/cm^2 and (d) 10.5 J/cm^2.

In the case of acetone, the distribution peak at 15.7 ± 0.2 nm at 2.6 J/cm^2 reduces to 12.3 ± 1.0 nm for laser influence 10.5 J/cm^2. The same results can be seen in toluene with laser fluence of 2.6 J/cm^2 where a bimodal distribution with peak sizes at 77.2 ± 1.7 nm and 25 ± 0.8 nm shifts to a unimodal distribution with peak size at 17.03 ± 0.8 nm. These results are also in agreement with previous studies from our group [99]. For analyzing the activity, two samples were prepared by ablating Al target for 4 min under 2.6 J/cm2 laser flux in acetone and toluene. The samples were tested in US Army facilities using LASEM. To this end, Figure 3.7 illustrates the laser-induced shock velocities for these samples and compares them to commercial micron size Al powders. The blank indicates the shock velocity of air induced by laser.

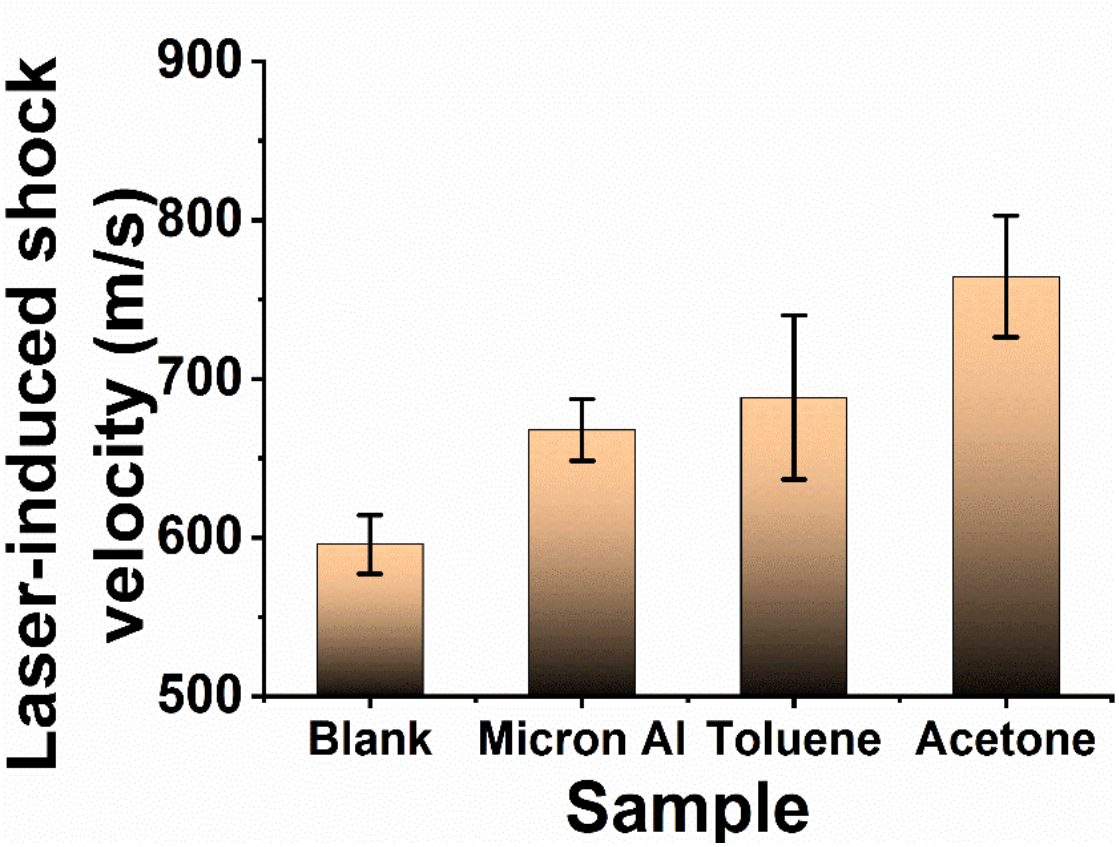

Figure 3.7: Laser-induced shock velocity measurements for synthesized samples and compared to micron size Al powder and air.

Comparing the results of LASEM from blank to other samples, the shock velocity is greater once the samples contain energetic materials such as Al. This observation confirms the resolution of the LASEM technique to detect energetic behaviors via shock wave velocity increases from known energetic material analytes. Moreover, it can be seen that both the specific samples prepared in toluene and acetone show greater activities as compared to the micron sized Al powder. Greater activity recorded from the synthesized samples can be correlated to the protective shells that prevent the Al nanoparticle surface from forming native oxide layers that stymies the oxidation kinetics due to the onset of diffusion limited oxidation pathways through the oxide shell layers. Added to this, the smaller sized carbon coated Al nanoparticles produced in acetone obviously exhibit higher activity as expected due to smaller diffusion length scales. Analyzing the shock

velocities of Al synthesized in acetone and toluene indicates improved activity and greater shock velocity of acetone over toluene. This can be attributed to the fact that particles prepared in acetone have smaller size in compare to particles synthesized in toluene. It is known as the size of the particles decreases the burning and oxidation process becomes more efficient. In case of toluene, particles show a bimodal size distribution with two classes at 25 nm and 77.2 nm. It is possible that the second class (77.2 nm) does not become fully oxidized due to larger size. Therefore, it acts as a dead load during the energy release and retards the energetic activity. Recently, LASEM has been employed for various energetic materials such as TNT (trinitrotoluene), PETN (pentaerythritol trinitrate) etc. to correlate laser-induced shock velocity to detonation velocity, pressure and classification of exothermic and explosive materials [96]. Comparing the shock velocity of Al particles prepared in toluene and acetone with previous studies [100, 101], we realized that the synthesis of Al in toluene results in exothermic rather than explosive properties, while preparation in acetone lies in explosive range. Moreover, the calibration curves based on the previous studies [96] have been used to estimate detonation properties of Al synthesized in acetone (Figures 3.8 a and b).

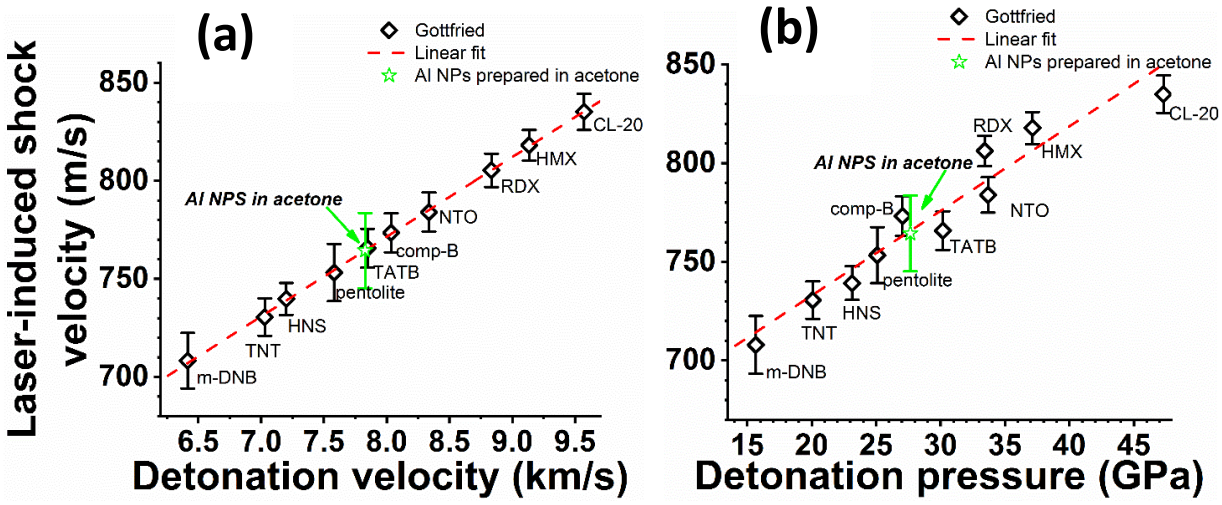

Figure 3.8: Correlation between laser-induced shock velocity and detonation velocities and pressure.

Based on the calibration curves the detonation velocity and pressure of Al nanoparticles synthesized in acetone is estimated as 7.83 km/s and 27.66 GPa respectively. These results indicate superior detonation velocity and pressure of Al nanoparticles synthesized in acetone over common explosive materials such as TNT, HNS (hexanitrostilbene), pentolite (50% PETN, 50% TNT).

3.4 Conclusion

Laser ablation synthesis in solution (LASiS) has been employed for synthesizing carbon shell coated Al nanoparticle as energetic materials to prevent the unwanted growth of native oxide layers on the active nanoparticle interface. The objective here was to preserve the pristine and reactive Al surfaces to prevent the domination of diffusion-limited oxidation through the oxide layers that are known to stymie the surface reaction rates. The shell-core Al nanoparticles have been prepared through laser ablation in different organic solvents such as acetone and toluene. The size and morphology of these particles have been investigated using scanning transmission electron microscopy (STEM). The effects of various organic solvents, laser flux and ablation time on particles size distribution have been investigated. It has been observed through controlling the LASiS medium, laser flux and ablation time the size distribution of particles is tunable. The energetic activities of the synthesized samples have been estimated through laser-induced air shock from energetic materials (LASEM) and compared to uncoated micron size Al powders and explosive materials. It has been observed that both samples prepared in acetone and toluene show greater energetic activities as compared to their micron sized Al powders due to the protection of the Al surface from unwanted oxide ash layer growths. Specifically, the as-prepared Al nanoparticles in toluene could be more categorized as exothermic materials when compared to their counterparts grown in acetone that exhibit more explosive properties. Thus, the results presented here provide preliminary indications that the nanostructures of carbon shell coated metal

nanoparticles can be effectively tailored via LASiS-based techniques to tune their energetic behaviors from solid-state flame additives to self-standing explosive materials. The as-synthesized samples in acetone indicated superior energetic activities as compared to the samples grown out of toluene. The superior activity was correlated to smaller particles size resulted from ablation in acetone. Finally, the explosive properties such as detonation velocity and pressure of the carbon shell coated Al nanoparticles synthesized in acetone were compared to a wide range of explosive materials. The results indicated superior detonation velocity and pressure as compared to well-known explosive materials such as TNT, HNS, and pentolite. The research developed through this work pave the path for future design and synthesis of the next-generation nano-energetic materials whose interfacial structures can be optimally tuned to outperform as well as regulate the reactivity of the first-generation energetic materials. Specifically, on-going efforts between our research group and the US ARL continue to investigate the abilities to tune excess interfacial stresses and internal pressures, and in turn, melting points of the core metal nanoparticle in these shell-core nanostructures to design them to behave as high pressure nano-reactor cells that can exhibit excessive pyrophoric behaviors under suitable external stimulation in the form of heat or pressure.

Chapter 4 Laser-Induced Breakdown Spectroscopy (LIBS): A Calibration-Free Analytical Technique for Quantitative Chemical Characterizations of Nanoalloys and Nanocomposites with Interfacial Activities

This chapter is based on the following publications:

- **Davari, S. A.**; Hu, S.; Mukherjee, D. "Calibration-free quantitative analysis of elemental ratios in intermetallic nanoalloys and nanocomposites using Laser Induced Breakdown Spectroscopy (LIBS)", Talanta, 2017, 164, 330–340.

- **Davari, S. A.**; Hu, S., Ribeiro, E. L., & Mukherjee, D. "Rapid elemental composition analysis of intermetallic ternary nanoalloys using calibration-free quantitative Laser Induced Breakdown Spectroscopy (LIBS)", MRS Advances, 2017, 1-6 ***[Invited Paper]***.

- Hu, S.; Ribeiro, E. L.; **Davari, S. A.**, Tian, M.; Khomami, B.; Mukherjee, D. "Hybrid nanocomposites of Co_3O_4 nanoparticle embedded reduced/nitrogen-doped graphene oxides for the selective improvement of electrocatalytic and/or supercapacitor functionalities", RSC Advances, 2017, 7, 33166–33176

4.1 Introduction

A critical bottleneck in the research and development of state-of the-art electrochemical energy conversion and storage systems (including fuel cells and metal–air batteries) remains in the design of intermetallic nanoalloys (NAs) and nanocomposites (NCs) as efficient catalysts – the main goal being the replacement of precious metals (Pt, Au, Pd etc.) with cheaper transition metal oxides. Specifically, due to the unique physicochemical, structural and electronic characteristics, Pt/Pd-M (M stands for transition metals such as Co, Ni, Fe, Cu, etc.) NAs are regarded as highly promising electrocatalysts for oxygen reduction reaction (ORR) [20, 102-104] and methanol/ethanol/formic

acid oxidation reaction [105-107] in fuel cell applications. On another hand, NCs of transitional metal oxides, metal/intermetallic nanoparticles (NPs) in metal oxide matrices (including perovskites) are known to exhibit outstanding bifunctional activities for both ORR and oxygen evolution reactions (OER) [17, 108-110]. However, the critical challenge remains in tailoring the elemental compositions of these NAs and NCs in an effort to tune their atomic lattice properties and in turn, their interfacial catalytic activities as well as precious metal loadings [111-114]. Thus, facile, efficient and, yet accurate chemical characterizations of a wide class of NAs and NCs become imperative for robust and rapid screening of superior catalysts. Inductively Coupled Plasma Optical Emission Spectroscopy (ICP-OES), and X-ray photoelectron spectroscopy (XPS) have been the conventional analytical techniques of choice for chemical composition characterizations. In spite of the well-established analytical capabilities of ICP-OES and XPS due to the robust instrumentation development and accuracy, they have their own pitfalls in terms of experimental protocols. In the case of ICP-OES, considerable sample preparations including external calibration standard requirements and rigorous acid digestions for many samples (including intermetallic NPs) prove to be highly problematic and time consuming [115-117]. Besides, many strong acids required for the sample digestions prove to be hazardous and incompatible with the instruments.

Laser Induced Breakdown Spectroscopy (LIBS) is a relatively nondestructive spectrochemical characterization technique, which can address the aforementioned issues in a facile, yet effective manner. Typically, LIBS involves the collection and processing of optical emissions emanating from a high-irradiance pulsed laser tightly focused to generate a high temperature, high pressure micro-plasma containing the analyte of interest [118]. These emissions (ionic, atomic and molecular), collected as spectral signatures, can reveal the constituents and properties of the

plasma and hence, the sample. The relatively simple set-up, and minimal sample preparations for LIBS have drawn the attention of analytical researchers in recent years [119]. Moreover, the fast operation and easy data collection of LIBS make it an ideal analytical tool for in-situ studies [120].

In the past, LIBS has found a vast amount of applications in diverse spectral, and elemental studies ranging from nanomaterials [121-123], and environmental/bio-hazard analysis [124-126], to forensics [127], explosives detection [128, 129], semiconductor and thin films [130], pharmaceutical [131], and biomedical [132] applications. Specifically, LIBS has been used for elemental analysis in bulk metallic alloys and composites include bulk steel sample analysis using single and double pulsed lasers [133], and identification of aluminum impurities in zinc-based alloys [134], both of which involve the use of calibration standards. Additionally, analytical measurements combining LIBS and laser-induced fluorescence [135] have been used to establish low detection limits for cobalt in low-alloy steels. In spite of the extensive use of LIBS on bulk alloy analysis, there appears to be a noticeable dearth in its extension toward quantitative analysis of intermetallic NPs, including NAs and NCs. Recent years have seen a growing interest in the use of LIBS for detailed nanoparticle characterizations that include the exhaustive research by Hahn and his co-workers in the past on the sizing and elemental analysis of aerosolized metal/metal oxide NPs [136-138]. Such works have led to continued efforts on the application of LIBS for detecting impurities in iron oxide nano-powders/NCs for both industrial and biomedical applications [139], as well as in identifying volume fraction of flame synthesized titania NPs using phase-selective LIBS [140]. More recently, LIBS was also used in distinguishing nanosized carbon materials based on molecular emissions from different graphitic lattices [141]. But, only a handful of works have employed LIBS for elemental analysis of complex intermetallic NPs. These include the in-situ confirmation of CuAg NP synthesis during laser ablation synthesis [142], and detection

of Ytterbium (Yb) in cobalt antimony (CoSb3) skutterudite voids [143]. While the aforesaid studies carried out some of the foremost spectrochemical characterizations of NPs and nanostructured materials, they have been largely limited to qualitative studies, or at the most, quantitative analysis based on external calibration standards. To this end, Mukherjee et al. [120] had carried out one of the formative studies in developing the calibration free quantitative LIBS methodology to measure the extent of oxidation on Al nanoparticles. This methodology was later extended and verified for detailed quantitative LIBS characterizations of carbonaceous aerosols and aerosolized drugs [126, 131]. To the best of our knowledge, no studies till date have successfully employed LIBS for quantitative elemental analysis of intermetallic NPs that can provide new directions toward future rapid and facile analytical techniques for in-situ chemical characterizations of complex heterogeneous nanomaterials during their large scale synthesis.

We address the aforesaid lapse in the application of LIBS toward rapid and high accuracy elemental characterizations of intermetallic NPs through our current work. It needs to be brought to attention that various calibration-free LIBS techniques have been developed in the past [144, 145]. But the current study is specifically built on the earlier studies of Mukherjee et al. [120] to employ the calibration-free quantitative LIBS toward rapid and facile analysis of compositional variations in complex intermetallic NAs/NCs. Specifically, we focus on the elemental composition analysis of PdCo and PtNi NAs, and PtCo NCs synthesized via our recently developed Laser Ablation Synthesis in Solution-Galvanic Replacement Reaction (LASiS-GRR) technique as part of our ongoing research efforts on directed design of intermetallic nanomaterials with low precious metal loadings as efficient ORR electrocatalysts [17, 20]. The accuracy of our results from the LIBS measurements will be verified by comparing against the corresponding results from ICP-OES analyses.

4.2 Experimental details

4.2.1 Experimental set-up

The experimental set-up is illustrated in Figure 4.1. The laser-induced plasma is generated with a Q-switched Nd-YAG laser of nominal wavelength 1064 nm operating at 200 mJ/pulse, and a pulse width of 8 ns (Make: Insight Model: 122551-R). As seen in Figure 4.1, the laser is focused with a 25 mm diameter fused silica lens (focal length=35 mm) that generates ~10–15 GW/cm^2 flux at the focal point on the target surface. The resulting high-energy plasma plume produces a high temperature that can reach up to ~30,000 K. The spot size on the sample is set to 75 μm diameter, which creates a plasma volume with size 1–2 mm3 approximately. Due to the thin film of deposition, one laser shot per spot is collected.

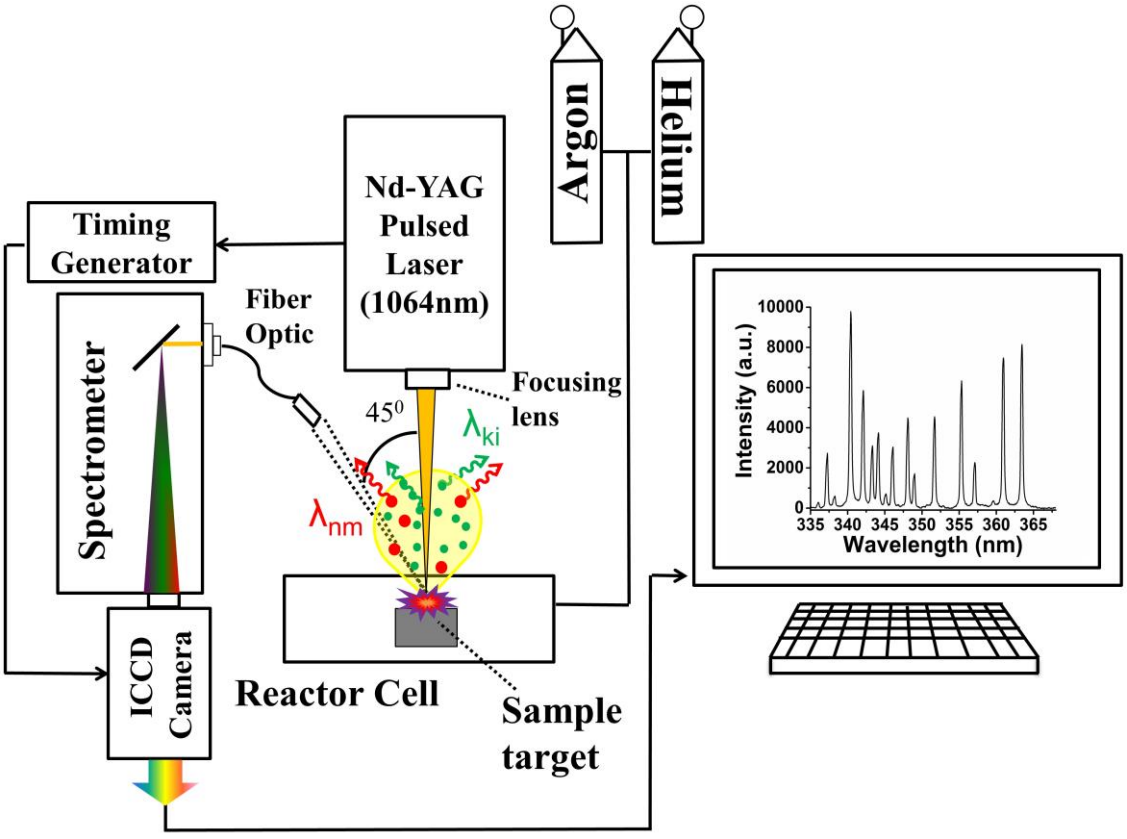

Figure 4.1: Schematic for LIBS experimental set-up used in this chapter.

But, in order to improve the statistical average of the signal intensity for each analyte of interest, spectral data over approximately 100–150 spots are collected.

The plasma emission is collected with a fiber optic port carrying a collimation-focusing lens pair and placed at 45 degree collection angle (see Figure 4.1), which yields the optimum intensity from the plasma volume. The focused light collected via a fiber optic cable is transmitted to a Czerny-Turner spectrometer (Make: Andor Technology; Model: Shamrock - SR-303i-A) with 1200 grooves/mm grating (resolution of 0.1 nm at 500 nm), and a nominal dispersion of 2.58 nm/mm. The slit width is fixed at 100 μm for all experiments carried out here in order to have the optimum spectral line intensity and resolution. A time-gated intensified charge-coupled device (ICCD) detector array (1024×1024 CCD) (Make: Andor Technology; Model: DH334T-18U-E3) detects the spectral lines at the spectrometer exit focal plane. The time gating is synchronized with the laser Q-switch through an in-built timing generator in the ICCD camera set-up.

4.2.2 Synthesis of nanoalloys (NAs) and nanocomposites (NCs)

All the metallic pellets were provided from Kurt J. Lesker (99.95% purity, 1/4″diameter×1/4″height). K_2PtCl_4 (> 99.9%), Na_2PdCl_4 (>99.9%) and HCl (37%) samples were purchased from Sigma-Aldrich. All NA and NC samples for the present study were synthesized using our recently developed LASiS-GRR technique and described elsewhere [17, 20]. For the preparation of binary PtNi and PdCo NAs, K_2PtCl_4 (250 mg/l) and Na_2PdCl_4 (125 mg/l) were used as the salt solutions, while Ni and Co were used as the targets separately. The ternary alloys, the PtCuCo NAs, are synthesized by ablating Co targets with a pulsed laser (1064 nm; 10 Hz with 360 mJ/pulse energy and 4 ns pulse width) in a mixture of K_2PtCl_4 and CuCl solutions. The colloidal solutions are then treated with HCl acid at pH2 for 12 hours followed by centrifugation at 4700 rpm for 8 mins. The resultant samples (precipitates) are marked as PtCuCo-1, PtCuCo-2, and

PtCuCo-3 respectively. The LASiS-GRR technique was carried out for preparation of NCs as well. In specific, for the synthesis of PtCo/CoOx NCs, Co target was ablated by the pulsed laser in K_2PtCl_4 solutions with different concentrations of 25, 60, 120 mg/l, with the resultant samples marked as PtCo1, PtCo2 and PtCo3 respectively. Finally, the precipitates from centrifugation were collected and deposited on silicon wafers that were pre-washed with water and ethanol to remove any residues for LIBS analysis. Specifically, around 20μ of the NP colloidal solutions (50 mg/l) were dropped casted to make the material loading densities of 1 mg/cm^2 for all the samples. All LIBS tests were carried out at ambient conditions that facilitate a simple and easy execution of the experiments.

4.2.3 Quantitative LIBS Methodology

In this study, atomic transition lines are chosen from the NIST Atomic Energy Levels Data Center [146] (wherever available) or from other sources otherwise (as referenced) based on the relative lines strength, and transition probabilities. As Tognoni et al. [147] and Hahn et al. [119] had extensively discussed in previous LIBS studies, generally there are two quantities describing the quality of measurements in LIBS practice, signal-to-noise ratio (SNR) and peak-to-base ratio (PTB). For all samples, the optimum gate delays are determined based on the variations of the signal-to-noise ratio (SNR) as a function of gate delays for the respective elemental species to gain maximum accuracy in our results. The SNR is calculated by measuring the peak signal value at the specific wavelength of interest for a spectral line divided by the noise of the spectra. The noise is defined as the root mean square over the baseline (~ over 40 pixel) adjacent to the analyte peak. Then, the optimum signal-to-noise ratio (I_{em}) is used as the effective emission for the population density calculations of the respective atomic species based on the Boltzmann distribution:

$$I_{em} = hc \frac{A_{ki}}{\lambda_{ki}} N_i \frac{g_k}{g_i} \exp\left(-\frac{\Delta E_{ki}}{k_B T_{exc}}\right) \quad (4.1)$$

where I_{em} is the optimal SNR, and N_i, A_{ki}, λ_{ki}, g_k, g_i are atomic number densities at the lower energy state, Einstein's transition probability, emitted wavelength, and statistical weights for the higher (k), and lower (i) energy states respectively for the specific atomic transition of interest. ΔE_{ki} is the energy difference between the k, and i states, and T_{exc} is the plasma temperature at the optimal gate delays determined for the species of interest. Boltzmann, and Planck's constant are indicated by k_B (1.38064×10^{-23} m^2kg/s^2K), and h (6.62607×10^{-34} m^2kg/s) respectively, and c (3×10^8 m/s) is the speed of light in vacuum.

Typically, plasma temperatures are calculated based on the slope of the linear fit to the Boltzmann plot of $\ln(I_{em}\lambda_{ki}/A_{ki}g_k)$ as a function of normalized upper energy level (E_k/k_B) (derived from eqn. (4.1) for multiple strong lines with sufficiently widespread upper energy levels. The validity of eqn. (4.1), and the linear Boltzmann plot for plasma temperature calculations is based on the assumption of local thermodynamics equilibrium (LTE) conditions for the laser induced plasma. LTE requires that the plasma quenching processes are predominantly collisional rather than radiative. Typically, such conditions are established within at longer times of plasma evolution (> 1 μs) [148]. Thus, all our emission lines are measured at gate delayed beyond 1 μs. As Mukherjee et al. [120] had discussed in details, both absolute and relative emission intensities are affected by instrument uncertainty such as optical alignment, slit width etc., and the plasma fluctuations due to laser shot-to-shot variations. Moreover, the plasma temperature changes with time, and its estimation from the Boltzmann plots at different gate delays also result in the estimation of population densities being relative. Therefore, it is essential to calibrate the population densities of the analyte species of interest against those for bulk matrix species at similar plasma conditions

to nullify the aforesaid plasma artifacts. To the end, the stoichiometric ratio between any two species X, and Y of interest is finally estimated through the following normalization technique:

$$R = \frac{[X]}{[Y]} = \frac{[N_i^{XI} / N_i^{BI}]_{@GD=t_1}}{[N_i^{YI} / N_i^{BI}]_{@GD=t_2}} \quad (4.2)$$

where, N_i^X, and N_i^B represents the lower energy state population densities of the analyte X, and the bulk species respectively.

4.3 Other characterizations

In order to verify the attained results from LIBS, we used the same samples and measured the elemental ratio using ICP-OES. The NAs and NCs are digested using aqua regia solution, and diluted to be used in ICP. Standard cobalt dichloride solution (≥99%) and Na_2PdCl_4 solution (>99.9%) are used for calibration of PdCo NA. For the PtCoNC standard cobalt dichloride solution (≥99%) and K_2PtCl_4 solution (> 99.9%), and for the PtNi NA standard nickel dichloride solution (≥99%) and and K_2PtCl_4 solution (> 99.9%) are used to calibrate the ICP with respect to the analytes of interest. Then, the standard samples and LASiS-GRR samples are both analyzed with ICP-OES (Perkin Elmer, Optima 4300 DV). Moreover, the morphology, structure and qualitative chemical composition of all the LASiS-GRR products (NAs and NCs) are analyzed with Transmission Electron Microscopy (TEM) images and Energy Dispersive X-ray Spectroscopy (EDX).

4.4 Results and discussion

4.4.1 PtNi binary nanoalloys

Preliminary analysis for the size, structural and compositional characteristics of the PtNi NA samples synthesized via LASiS-GRR are observed from TEM and XRD measurements in Figure 4.2. The TEM image in Figure 4.2a reveals the largely spherical structures of the PtNi NAs with

mean sizes of ~10 nm. Preliminary EDX results also confirm qualitatively that the NPs comprise Pt, and Ni as the main atomic constituents. The high-angle annular dark-field (HAADF) image and the EDX mappings (Figure 4.2b-d) indicate that both Pt and Ni are uniformly distributed in the bright spherical NPs, which confirm the formation of PtNi alloy. Moreover, absence of O in Figure 4.2e indicates formation of NAs as compared to the metal/metal oxide NCs. The Cu peak in EDX spectrum (Figure 4.2f) for the identified spot corresponds to TEM carbon film with copper grids. The EDX spectrum also confirms that all other residual elements from the salts and other chemicals (such as K_2PtCl_4 and KCl) are washed way during the centrifugation process.

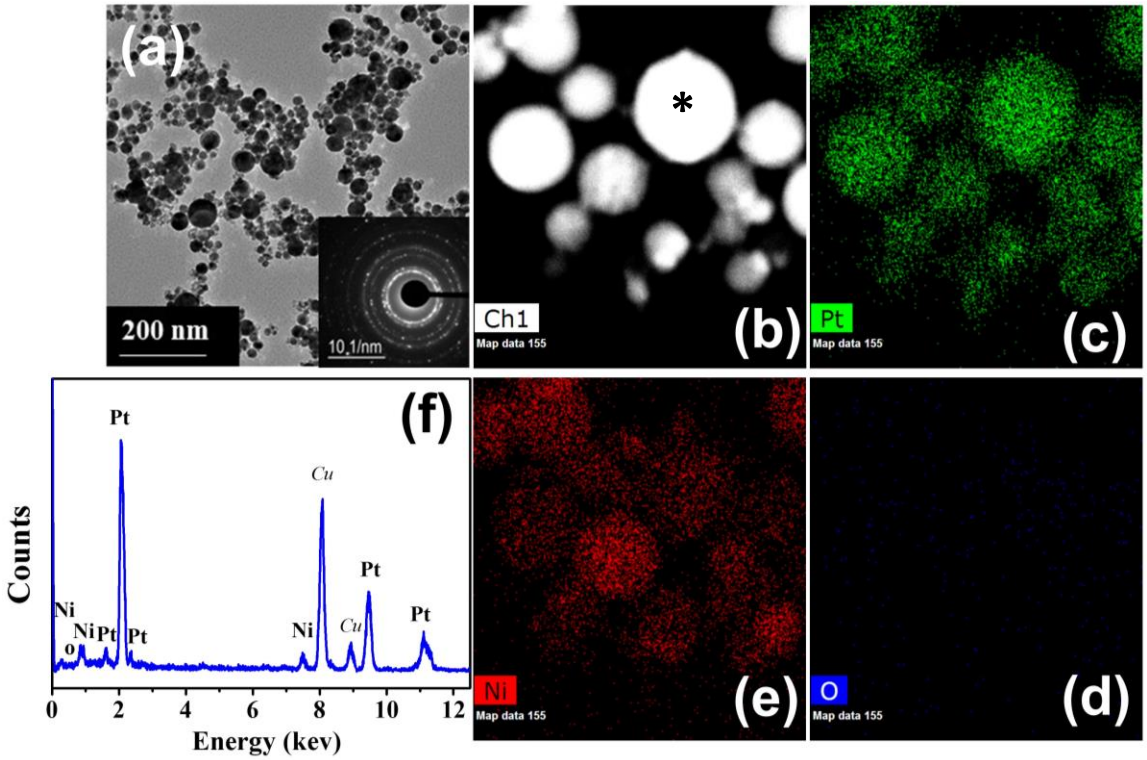

Figure 4.2: (a) Respective TEM image for PtNi NA/ inset indicating electron diffraction pattern. (b) HAADF image and (c-e) EDX elemental mapping for Pt, O, and Ni respectively. (f) EDX spectrum at spot (*) in (b).

Upon qualitative confirmation of the uniform distribution of Pt and Ni from our preliminary characterizations on the NA samples, the sample is drop cast on Si wafers for quantitative LIBS measurements. The atomic emission lines of Pt I (306.47 nm) and Ni I (349.29 nm) used for the

population density calculations from quantitative spectral analysis are shown in Table 4.1. The specific choice of the lines are based on their robust transition probabilities and line strengths, w

hile bearing in mind that their lower energy states are identified as close as possible to the ground states (i.e., Ei~0 eV) (see Table 4.1).

Table 4-1. Atomic spectral database [142] for Pt I and Ni I mission lines used for the population density calculations during quantitative analysis of PtNi NAs.

Species	Wavelength, λ_{ki} (nm)	Transition probability, A_{ki} (10^6 1/s)	Upper energy level E_k (eV)	Lower energy level E_i (eV)	g_k	g_i
Ni I	349.29	98	3.66	0.11	3	5
Pt I*	306.47	67	3.914	0	5	7
O I**	777.19	36.9	10.741	9.146	7	5

* From reference [145]
**Used for the internal calibration standard

Although the aforesaid Pt I and Ni I lines are listed in NIST Spectral Database [146], their detailed properties are referenced from another source [149] due to the lack of detailed information on the Pt lines from the NIST database. The temporal evolution of SNRs for the Pt I (306.47 nm), and Ni I (349.29 nm) transition lines are collected at a fixed gate width of 5 μs, as shown in Figure 4.3a and b respectively. Since the Ni I (349.29 nm) emission line did not show a clear, distinct peak, a curve fit was used to obtain the optimal gate delay. From these plots, the optimal gate delays are estimated to be 3.5 μs and 5.2 μs for the respective Pt I and Ni I lines. The spectral emission lines for Pt I (306.47 nm), and Ni I (349.29 nm) are illustrated in Figure 4.4a & b at the respective gate delays of 3.5 and 5.2 μs respectively.

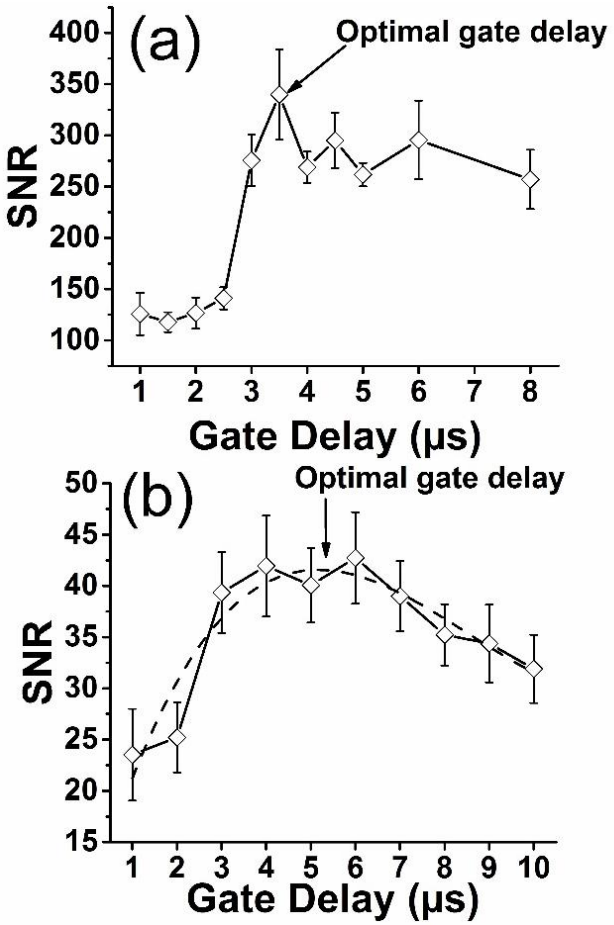

Figure 4.3: Temporal evolution of signal-to-noise ratio for (a) Pt I (306.47 nm) and (b) Ni I (349.29 nm). The optimal delays were determined as 3.5 and 5.2 μs for Pt I (306.47 nm) and Ni I (349.29 nm)

It needs to be pointed out here that the spectral window in Figure 4.4a also indicate the presence of other Pt I transition lines at 292.98 nm and 299.8 nm but the 306.47 nm transition line, being the strongest and devoid of any interference from other plasma emission lines, was chosen for all our spectral analysis here. The corresponding plasma excitation temperatures (T_{exc}) needed for Pt and Ni atomic number density calculations from spectral analyses (eqn. (4.1) described earlier in methodology section) are estimated from the respective linear Boltzmann plots at 3.5 and 5.2 μs gate delays, shown as insets in Figure 4.4 a & b respectively. Here a series of Pt I lines with known robust spectral properties, as listed in Table 4.2, are chosen for the construction of the aforesaid linear Boltzmann plots.

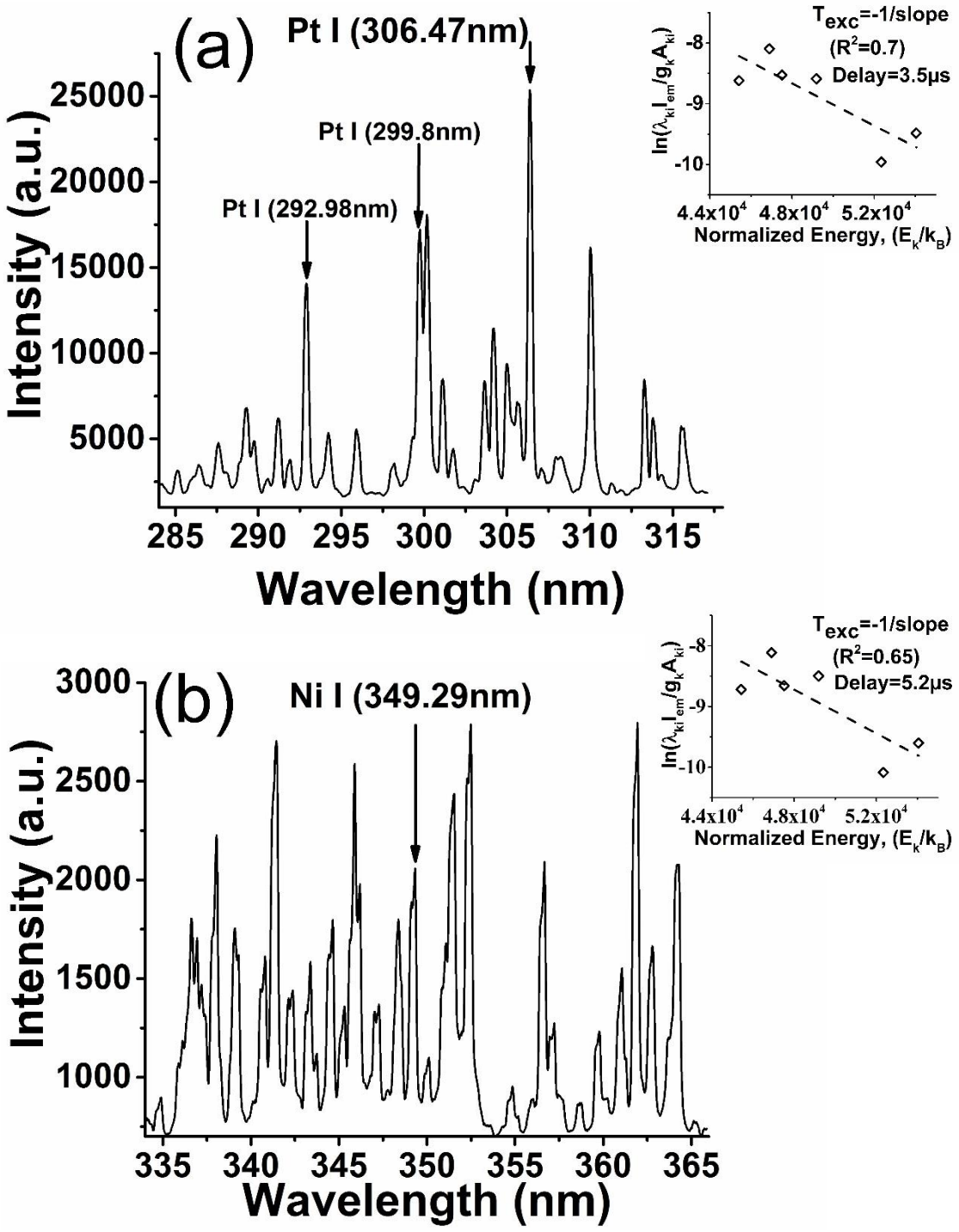

Figure 4.4: Spectral emission signature for (a) Pt I (306.47 nm) and (b) Ni I (349.29 nm) at 3.5 and 5.2 μs respectively. Insets indicate linear Boltzmann plots for calculating Texc at 3.5 and 5.2 μs based on Pt I lines listed in Table 4.2.

Table 4-2. Atomic spectral database [145] for different Pt atomic emission lines used for the plasma temperature calculations at 3.5μs, and 5.2μs for spectral analysis of Pt Ni NAs.

Species	Wavelength, λ_{ki} (nm)	Transition probability, A_{ki} (10^6 1/s)	Upper energy level E_k (eV)	Lower energy level E_i (eV)	g_k	g_i
Pt I	262.803	59	4.65790896	0.09310704	5	5
Pt I	265.945	99	4.51086828	0	9	7
Pt I	283.02	24	4.23859836	0	7	7
Pt I	289.38	7.7	4.23859836	0.09310704	7	5
Pt I	292.97	22.3	4.0946598	0	7	7
Pt I	299.79	33.2	4.0946598	0.09310704	7	5
Pt I	304.26	7.7	4.04164824	0.09884136	11	9
Pt I	306.47	67	3.91440216	0	5	7

Based on the slopes of the Boltzmann plots (indicated in the insets in Figure 4.4a & b), the plasma excitation temperatures are estimated to be 5747 ± 1889 K, and 5556 ± 2019 K at 3.5 and 5.2 μs gate delays respectively. Since our experiments are carried out in ambient conditions, the population densities of the aforesaid analyte species are normalized with those of oxygen atoms estimated from the atomic emission line of O I (777.19 nm). Here, we have considered the background bulk oxygen species as the internal calibration standard as discussed in details in the LIBS methodology section earlier. Thus, using eqn. (4.2), the quantitative estimation for [Pt]/[Ni] is obtained from the following normalizations of Pt and Ni atomic number densities at the respective gate delay times as indicated below:

$$R = \frac{[Pt]}{[Ni]} = \frac{[N_i^{Pt\,I(306.47nm)} / N_i^{O\,I(777.19nm)}]_{@GD=3.5\mu s}}{[N_i^{Ni\,I(349.29)} / N_i^{O\,I(777.19nm)}]_{@GD=5.2\mu s}}$$

Based on the aforesaid expression, the stoichiometric value is estimated to be [Pt]/[Ni]~ 4.56 ± 0.8. The error is calculated based on the error propagation analysis due to uncertainty in SNR, and plasma excitation temperatures (T_{exc}).

4.4.2 PdCo binary nanoalloys

We also extended the aforesaid LIBS technique for investigating palladium cobalt (PdCo) nanoalloys synthesized via the LASiS-GRR process. The TEM and EDX measurements once again indicate the samples to comprise spherical NPs with mean sizes ~5–10 nm (TEM image in Figure 4.5a), while the HAADF image in Figure 4.5b along with EDX mappings for Pd, Co, O indicate that the NPs are mainly composed of Pd (Figure 4.5c) with a very low atomic density of Co. Moreover, unlike the PtCo NCs reported earlier, an extremely low O distribution here confirms the formation of NAs in this case (Figure 4.5e).

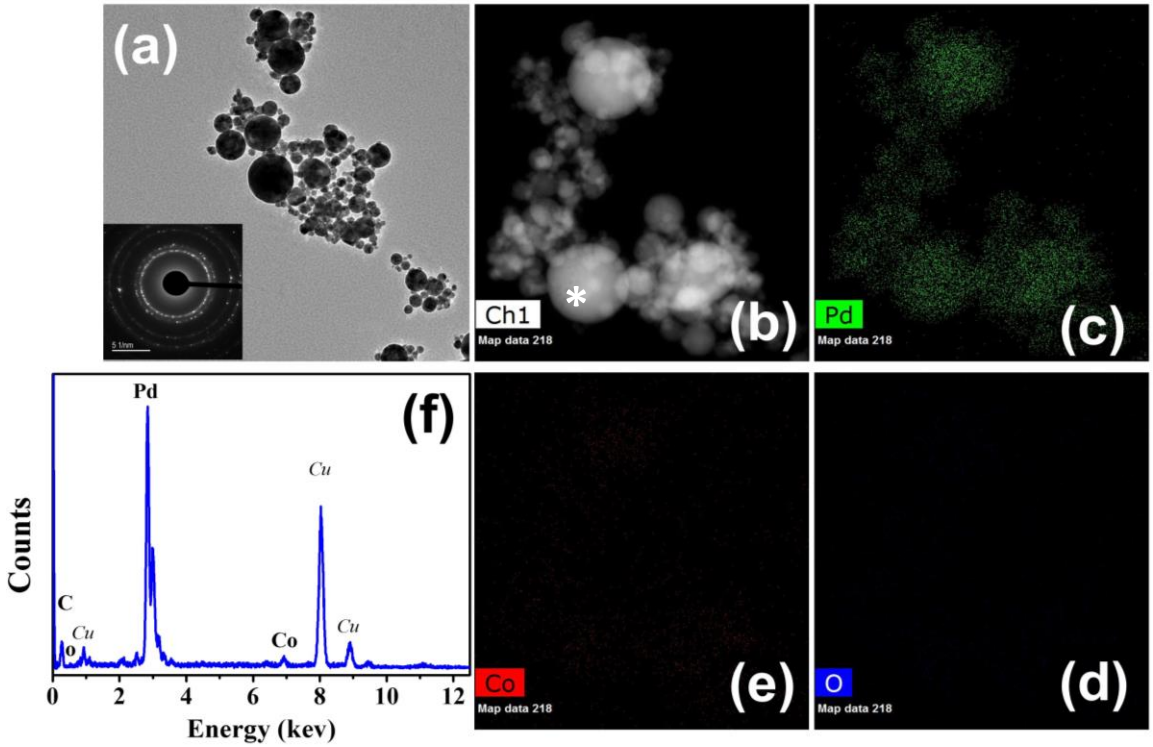

Figure 4.5: (a) TEM image for PdCo NAs, (b) HAADF image and (c-e) EDX elemental mapping for Pd, O, Co and (f)) EDX spectrum at spot (*) in (b).

The almost negligible O peak in EDX spectra also corroborates the same, while the relatively low Co peak (Figure 4.5f), as compared to the Pd peak, qualitatively indicate the low Co to Pd ratios in the PdCo NAs. For the detailed quantitative LIBS analysis, we chose the same Co atomic transition line of Co I (345.35 nm) (X) as also used in our earlier case study of PtCo NAs. On the other hand, the Pd I (360.95 nm) (X) line chosen for the population density analysis is based on the transition probability and line strength as listed in Table 4.3.

Table 4-3. Atomic spectral database [142] for Pd I and Co I emission lines used for the population density calculations during quantitative analysis of PdCo NAs.

Species	Wavelength, λ_{ki} (nm)	Transition probability A_{ki} (10^6 1/s)	Upper energy level E_k (eV)	Lower energy level E_i (eV)	g_k	g_i
Pd I	360.95	82	4.395	0.961	7	5
Co I	345.35	110	4.026	0.432	12	10

In this case, the optimal gate delay values for Pd I (360.95 nm), and Co I (345.35 nm) transition lines, determined from temporal evolution of their respective SNRs, are estimated to be 3 μs, and 7 μs for a fixed gate delay of 5 μs (as indicated Figure 4.6a & b).

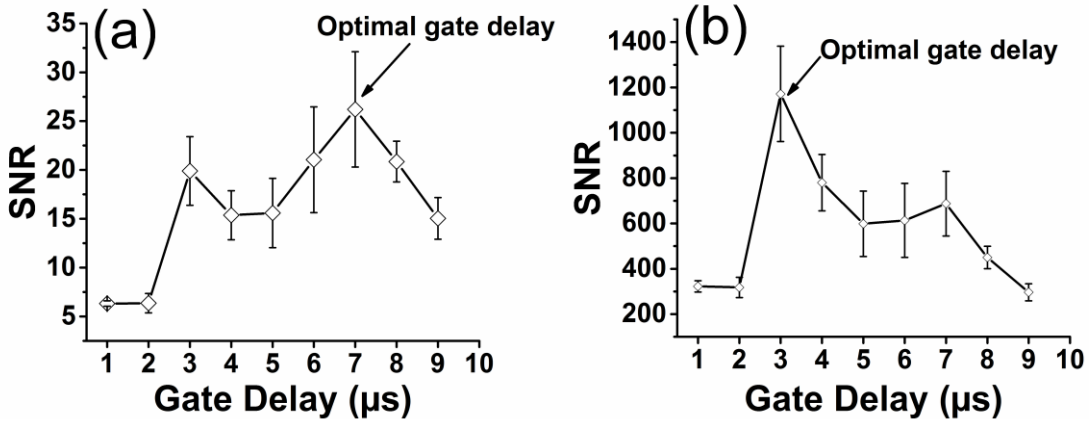

Figure 4.6: Temporal evolution of signal-to-noise ratio for (a) Co I (345.35 nm) and (b) Pd I (360.95 nm). The optimal delays were determined as 3 and 7 μs for Co I (345.35 nm) and Pd I (360.95 nm) respectively.

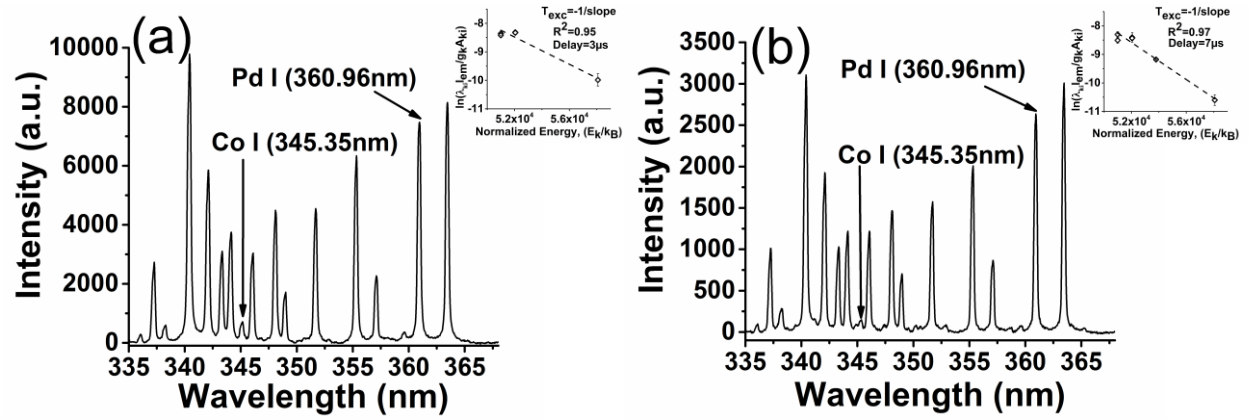

Figure 4.7: Spectral emission signature for (a) Pd I (360.95 nm) and (b) Co I (345.35 nm) at 3 and 7 μs respectively. Insets indicate linear Boltzmann plots for calculating T_{exc} at 3 and 7 μs based on Pd I lines listed in Table 4.4.

As seen from Figure 4.7a & b, Pd I and Co I lines in this case provide the advantage of being situated in the same spectral window. But, as expected here, the LIBS emission lines for Pd I (360.95 nm) at both 3 and 7 μs gate delay times indicate a much stronger spectral signature as compared to those for Co (see Figure 4.7a & b). This clearly indicates the elemental concentration of Pd to be significantly higher than that for Co in the as-synthesized PdCo NAs. It is worth mentioning that although the Co I (345.35 nm) absolute emission intensity at 3 μs is slightly higher than the corresponding value at 7 μs, the SNR is significantly lower due to the higher background noise at earlier delay times. In the choice of emission lines of the analyte species themselves for the normalization process in this case, we had to judiciously use different Pd I lines only due to the weak signatures of the Co I lines. It should also be noted here that the rapid disappearance of oxygen emission lines, O I (777.19 nm) at later delay times made it not possible for us to use atomic densities as estimated from O I (777.19 nm) line at 7 μs gate delay time for the normalization process. Thus, Table 4.4 lists all the Pd I atomic transition lines used for the normalization technique here. The identification of a series of strong Pd I emission lines, as listed

in Table 4.4, also enabled us to use the same lines The corresponding plasma temperatures are reported to 4184 ± 554 K, and 3076 ± 285 K respectively.

Table 4-4. Atomic spectral database [142] for Pd atomic emission lines used for plasma temperature calculations and internal calibrations at 3μs, 7μs for spectral analysis of PdCo NAs

Species	Wavelength λ_{ki} (nm)	Transition probability A_{ki} (10^6 1/s)	Upper energy level E_k (eV)	Lower energy level E_i (eV)	g_k	g_i
Pd I	247.64	11.8	5.0050928	0	3	1
Pd I	276.31	16.9	4.4858322	0	3	1
Pd I	324.26	77	4.6362356	0.8138506	7	7
Pd I	346.07	30	4.3954187	0.8138506	7	7
Pd I	351.69	103	4.4858322	0.9615006	3	5
Pd I	360.95	820	4.3954187	0.9615006	7	5

Finally, similar to the methodology explained earlier, the estimated quantitative stoichiometric ratio of [Co]/[Pd] is obtained as:

$$R = \frac{[Co]}{[Pd]} = \frac{[N_i^{Co\,I(345.35nm)} / N_i^{Pd\,I}]_{@GD=3\,\mu s}}{[N_i^{Pd\,I(360.95)} / N_i^{Pd\,I}]_{@GD=7\,\mu s}}$$

The estimated stoichiometric ratio for PdCo nanoalloys is 0.06 ±0.005. The low amount of cobalt in the nanoalloy is in agreement with the EDX results, which had also qualitatively indicated a low distribution of cobalt in the nanoalloy. Furthermore, the results in this case demonstrate the resolution of our quantitative LIBS methodology in estimating trace level elemental ratios in alloyed nanoparticles.

4.4.3 PtCuCo ternary nanoalloys

Figure 4.8 shows the representative TEM and XRD results for the PtCuCo ternary NAs synthesized using our LASiS-GRR technique. Figure 4.8a indicates that the synthesized ternary NAs are spherical with mean diameter ~20nm. The uniform distribution of Pt, Cu, and Co is confirmed through high-angle annular dark-field (HAADF) image and EDX mappings (Figure 4.8b-e). Figures. 4.8f and 4.8g show the EDX spectra at the identified spots (indicated by * in Figures 4.8d and 4.8e) respectively. The Ni and C peaks in the EDX spectra are resulted from the carbon film with Ni grid. Moreover, comparing the peaks, it can be observed that the amount of Pt is greater than Cu and Co in the synthesized ternary NAs. To quantitatively characterize the elemental ratios in the NA samples, the samples are deposited on silicon wafer for LIBS measurements. Table 4.5 shows the atomic emission lines used for the population density calculations. The lines are chosen based on their high transition probability, line strength, and lower energy states.

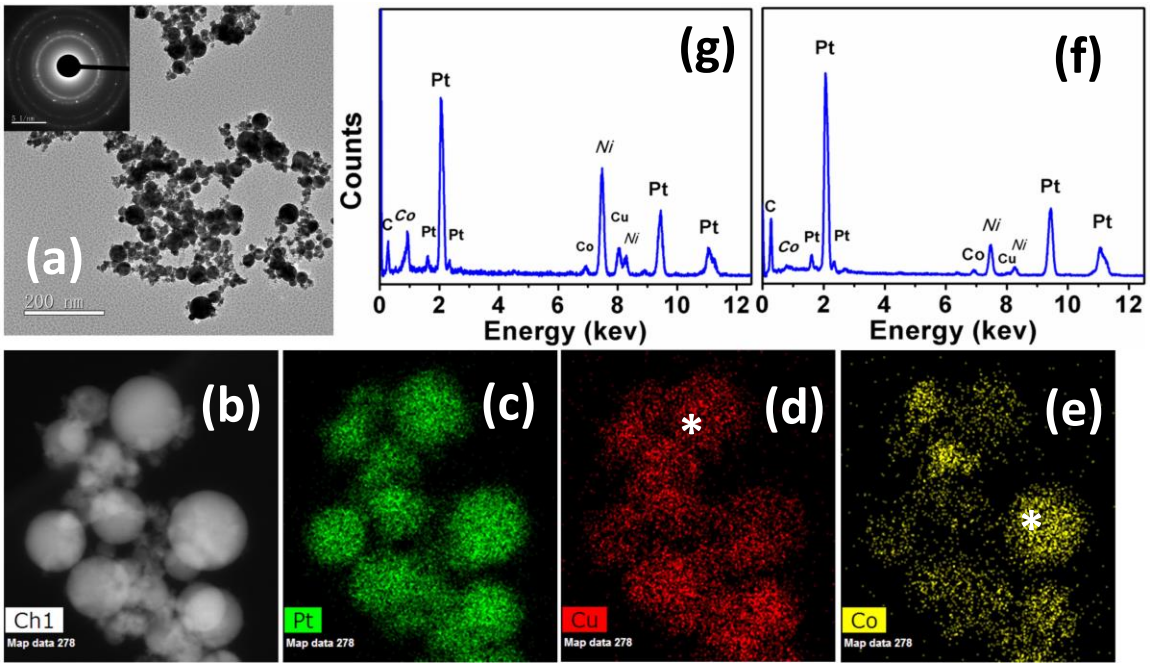

Figure 4.8: (a) TEM image for PtCuCo NAs, (b) HAADF image and (c-e) EDX elemental mapping for Pt, Cu, Co respectively and (f-g)) EDX spectra at spot (*) in (d) and (e).

Table 4-5. Atomic spectral database [142] for different Pt, Cu, and Co atomic emission lines employed for population density calculations.

Species	Wavelength, λ_{ki} (nm)	Transition probability, A_{ki} (10^6 1/s)	Upper energy level, E_k (eV)	Lower energy level, E_i (eV)	g_k	g_i
Pt I[(a)]	265.945	99	4.51086828	0	9	7
Pt I[(a)]	283.02	24	4.23859836	0	7	7
Pt I[(a)]	292.97	22.3	4.0946598	0	7	7
Pt I[(a)]	306.47	67	3.91440216	0	5	7
Cu I	324.754	140	3.816692	0	4	2
Cu I	327.395	138	3.7858976	0	2	2
Co I	340.512	100	4.071888	0.431815	10	10
Co I	345.35	110	4.020881	0.431815	12	10
Co I	350.228	80	3.970904	0.431815	8	10

[(a)] From reference [145]

To obtain the optimum SNR (I_{em}) for improving the accuracy of quantitative estimations, the temporal evolution of SNR for different emission lines obtained from LIBS are plotted in Figure 4.9 as a function of gate delay for a fixed gate width 5 μs. The optimum gate delay for Pt I (306.47nm), Cu I (324.75nm), and Co I (345.35nm) atomic transition lines are determined to be all ~4 μs. The respective spectra of the samples at 4 μs are illustrated in Figure 4.10 to indicate the different atomic transition lines of the analyte species of interest. Figure 4.10 a & b also indicate a wide range of other detected Pt I transition lines that are used for constructing Boltzmann plots and plasma excitation temperature calculations. These lines and their properties are listed in the supplementary information. Three different samples with various stoichiometric ratios were prepared using LASiS-GRR technique to generate a wide range of elemental ratios. The plasma excitation temperatures are estimated from the linear fits to the Boltzmann plots obtained from Pt I lines listed in supplementary information (Figure 4.11). From the slopes of the fits (R2 ~0.93 - 0.96), the plasma excitation temperatures are estimated to be 6566.99 ± 776.98 K (PtCuCo-1), 5585.71 ± 772.71 K (PtCuCo-2), and 5108.70 ± 798.27 K (PtCuCo-3) at 4 μs.

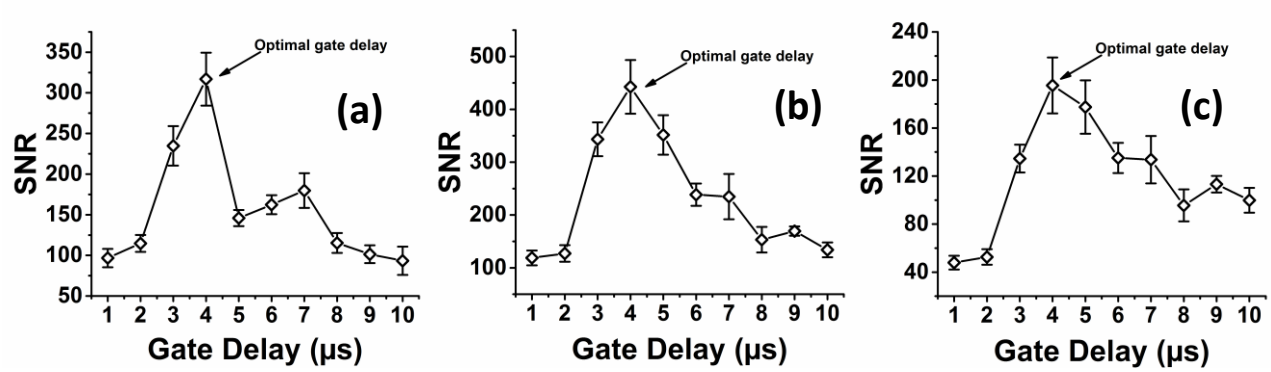

Figure 4.9: Temporal evolution of signal-to-noise ratio for (a) Pt I (306.47 nm), (b) Cu I (324.75 nm) and (c) Co I (345.35 nm). The optimal delays for all analytes were determined as 4μs.

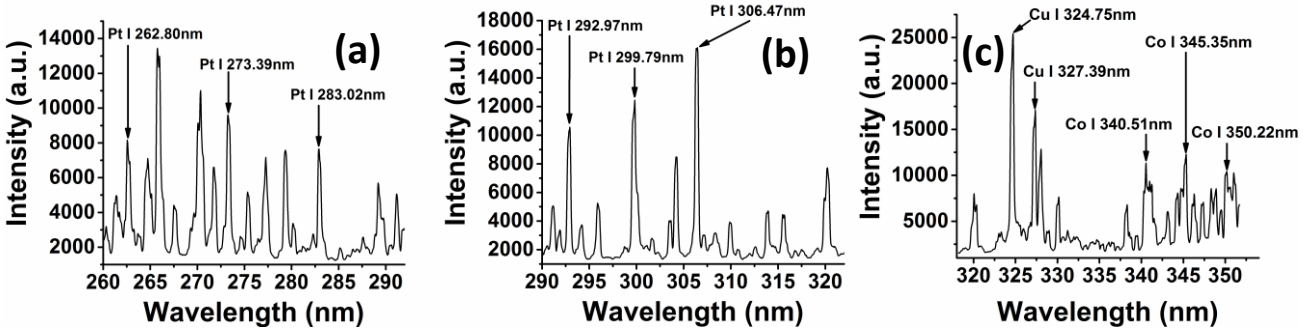

Figure 4.10: LIBS spectra emission signatures from NA indicating various Pt I, Cu I and Co I transition lines collected at 4 μs.

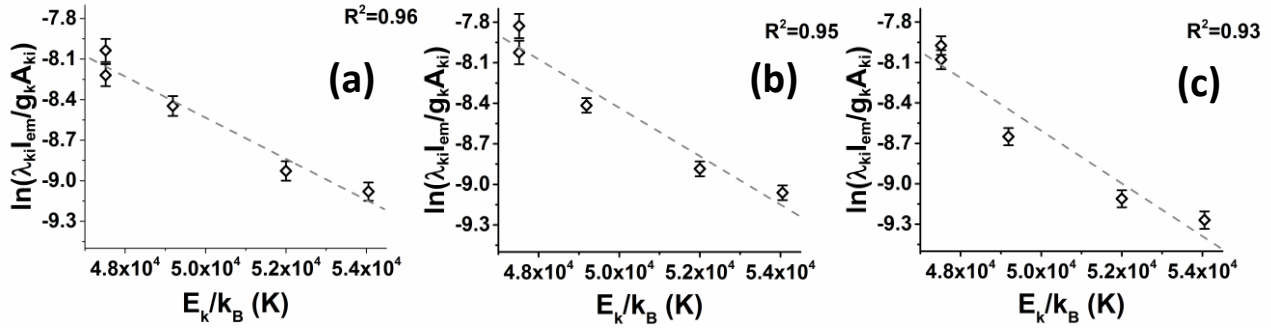

Figure 4.11: Linear Boltzmann plots and linear fits for plasma excitation temperature calculations of three different PtCuCo ternary alloys.

Upon estimating the plasma excitation temperature, the calculation of population densities of various species of interest becomes possible following the internal calibration procedure.

4.4.4 PtCo nanocomposites

As before, the structure, and composition of the samples are verified first from TEM and EDX measurements in Figure 4.12, with the TEM image (Figure 4.12a) distinctly indicating the spherical NPs dispersed in a matrix of "sponge-shaped" nanostructures. The mean sizes of the NPs are estimated to be ~5–10 nm. Furthermore, the elemental distribution of the sample, as characterized from HAADF image (Figure 4.12b) along with the EDX mappings (Figure 4.12b-e), indicate the presence of Co, Pt, and O respectively for the dark field images from Figure 4.12b. It confirms existence of both Pt and Co in the spherical structures.

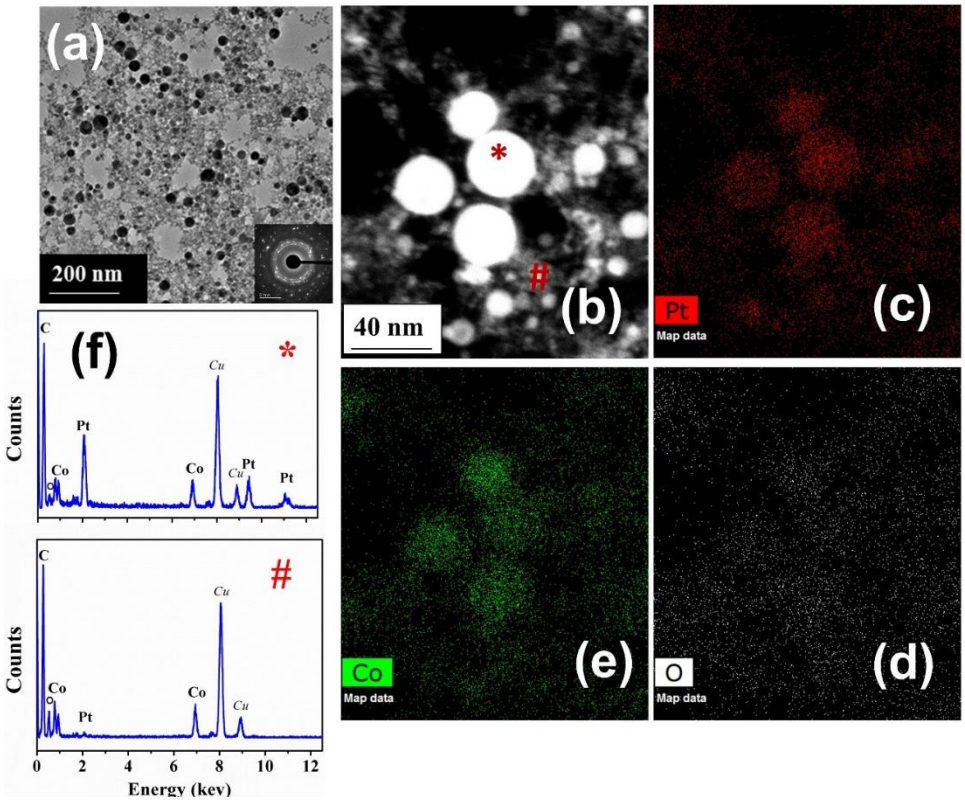

Figure 4.12: (a) Respective TEM image for PtCo NC/ inset indicating electron diffraction pattern. (b) HAADF image and (c-e) EDX elemental mapping for Pt, O, and Co respectively. (f) EDX spectra at spots (*) and (#) in (b).

Hence confirms the formation of PtCo NAs in the bright NPs in HAADF image (Figure 4.12b). Concurrently, Co is detected within the nonspherical structures (Figure 4.12d), while O is almost uniformly distributed in the entire grid of the EDX mapping (Figure 4.12e). The same is also corroborated by the respective EDX spectra in Figure 4.12f corresponding to the sample areas indicated as (*) and (#) in Figure 4.12b. Therefore, it can be qualitatively concluded that the samples are largely composed of NCs of PtCo NAs in CoOx matrices. Further investigations on the quantitative elemental analyses of the PtCo NC samples are carried out from LIBS characterizations. The Pt I (306.47 nm) line used here for all spectral calculations is the same one as used before for the PtNi case study. The cobalt atomic transition line Co I (345.35 nm) is chosen based on the transition probability and line strength as reported in details in Table 4.6. In this case, the temporal evolution plots for SNRs in Figure 4.13 indicate that for both Pt I (306.47 nm) and Co I (345.35 nm) lines, the optimal gate delays appear at 4 μs for the fixed gate width of ~5 μs.

Table 4-6. Atomic spectral database [142] for Pt I and Co I emission lines.

Species	Wavelength, λ_{ki} (nm)	Transition probability, A_{ki} (10^6 1/s)	Upper energy level, E_k (eV)	Lower energy level E_i (eV)	g_k	g_i
Co I	345.35	110	4.026	0.432	12	10
Pt I*	306.47	67	3.914	0	5	7

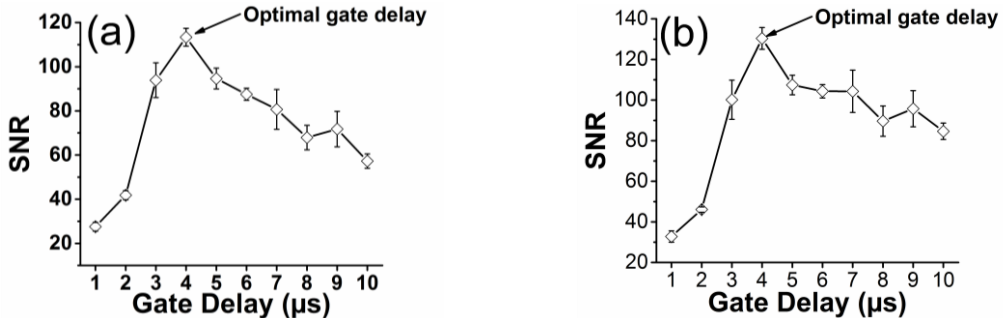

Figure 4.13: Temporal evolution of SNR for (a) Pt I (306.47 nm) and (b) Co I (345.35 nm). The optimal delays were determined as 4 μs for Pt I (306.47 nm) and Co I (345.35 nm).

To establish the accuracy and robustness of the quantitative LIBS technique, three different samples with varying stoichiometric compositions of PtCo NCs (PtCo1, PtCo2, and PtCo3 as prepared using the LASiS-GRR technique, and described earlier in the experimental details section) are analyzed here. Figure 4.14 illustrates the characteristic emission spectra of Pt I (306.47 nm), and Co I (345.35 nm) at 4 μs gate delay at different emission windows, which reveals other emission lines of both Pt and Co at the corresponding windows. Both Pt I (306.47 nm) and Co I (345.35 nm) indicate the highest intensity values, as it was expected due to their greater transition probabilities, and emission strengths. The plasma temperatures at 4 μs gate delay times are estimated based on a linear fit to the Boltzmann plot generated from the same series of Pt I emission lines as reported earlier in Table 4.2. Figure 4.15a-c indicates the corresponding Boltzmann plots along with the respective linear fits for the three different samples (PtCo1, PtCo2, PtCo3 respectively) under study here. The plasma temperatures (Texc, K) are estimated from the slopes of the linear fits in Figures 4.15a-c.

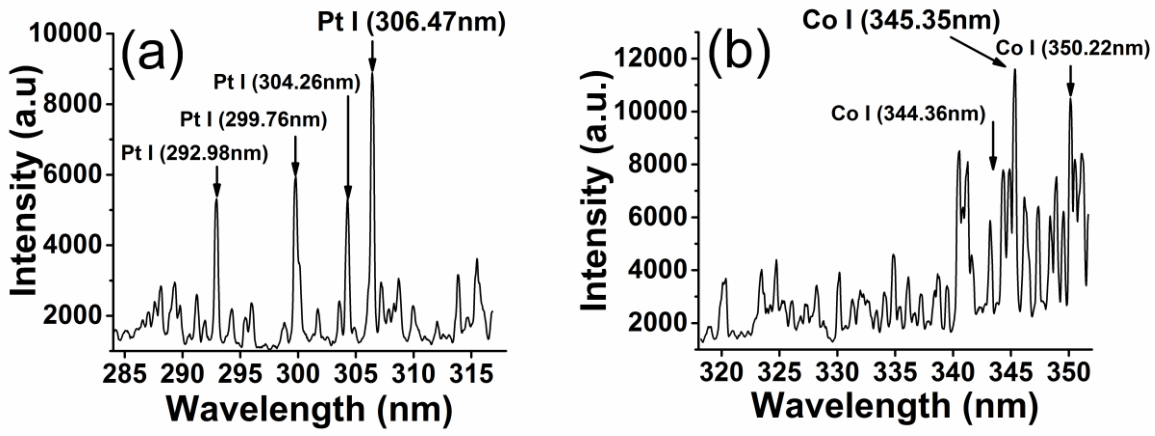

Figure 4.14: Spectral emission signature of (a) Pt I (306.47 nm) and (b) Co I (345.35 nm) lines at 4 μs gate delay.

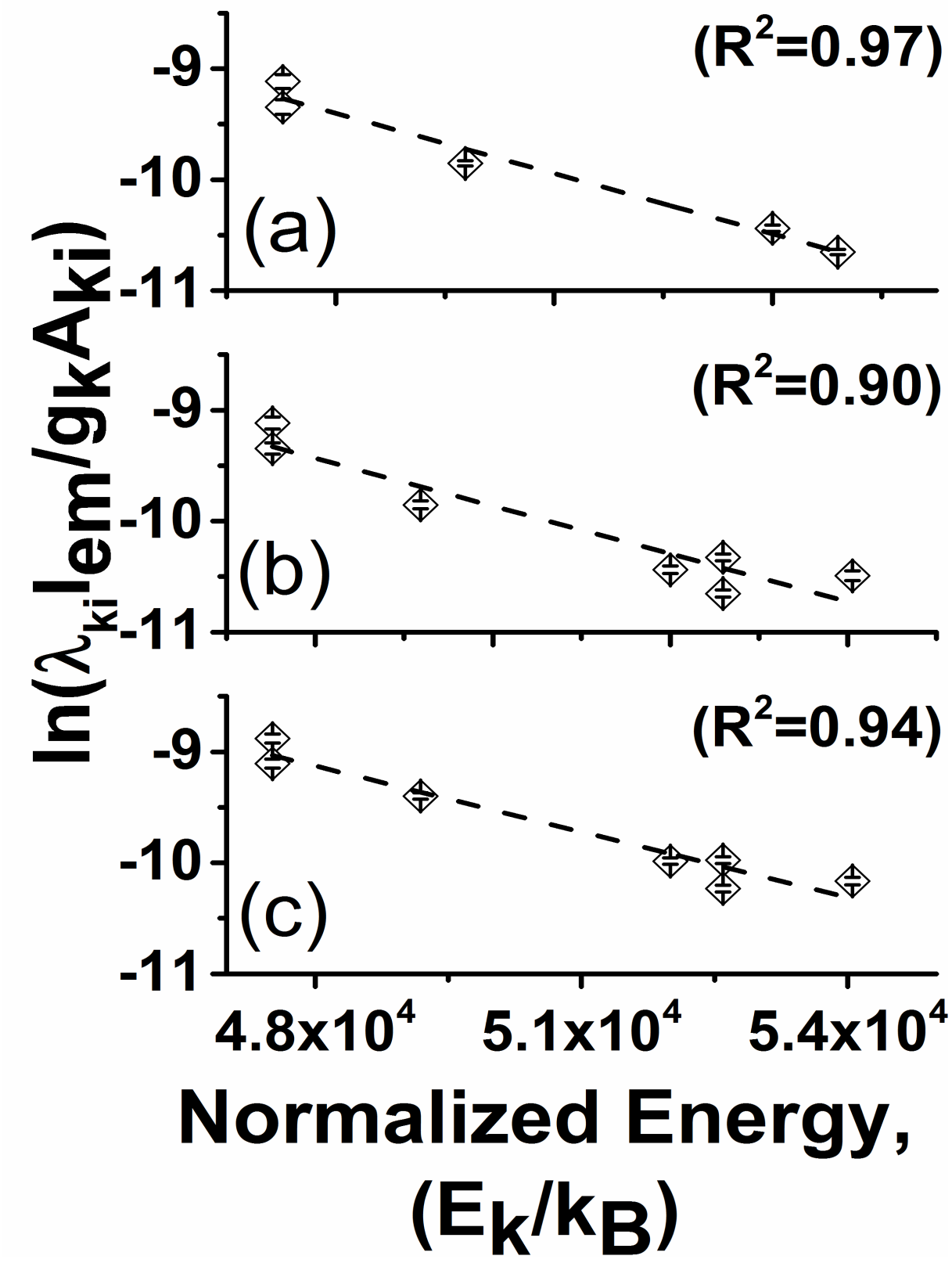

Figure 4.15: Boltzmann plots and linear fits for calculating plasma excitation temperatures for (a-c) three different PtCo NCs.

Table 4-7. Atomic spectral database [142] for different Pt atomic emission lines used for the plasma temperature calculations at 4μs and internal calibration standard, and different Co emission lines used for the internal calibration standard at 4μs.

Species	Wavelength λ_{ki} (nm)	Transition probability A_{ki} (10^6 1/s)	Upper energy level E_k (eV)	Lower energy level E_i (eV)	g_k	g_i
Pt I*	262.803	59	4.65790896	0.09310704	5	5
Pt I*	265.945	99	4.51086828	0	9	7
Pt I*	283.02	24	4.23859836	0	7	7
Pt I*	289.38	7.7	4.23859836	0.09310704	7	5
Pt I*	292.97	22.3	4.0946598	0	7	7
Pt I*	299.79	33.2	4.0946598	0.09310704	7	5
Pt I*	304.26	7.7	4.04164824	0.09884136	11	9
Pt I*	306.47	67	3.91440216	0	5	7
Pt I*	330.185	25.3	4.4213652	0.78809532	3	5
Co I	340.512	100	4.071888	0.431815	10	10
Co I	344.36	69	4.112972	0.513624	8	8
Co I	345.35	110	4.020881	0.431815	12	10
Co I	350.228	80	3.970904	0.431815	8	10

* From reference [145]

This temperatures are found to be 3682 ± 357 K (PtCo1), 4645 ± 685 K (PtCo2), and 5061 ± 559 K (PtCo3) at 4 μs gate delay times. It should be noted here that since the optimum gate delays for both Pt I (306.47 nm), and Co I (345.35 nm) occur at 4 μs, we could not use the same atomic density of bulk oxygen for normalizing the population densities of both Pt and Co as they would simply cancel each other out. Therefore, we had to resort to a similar technique employed earlier by Mukherjee et al. [126] in employing a series of different transition lines of the analyte species itself as the internal calibrator for the normalization process. Table 4.7 lists all the Pt and Co lines used for the aforesaid normalization. In line with our earlier calculations, the estimated quantitative stoichiometric ratio of [Pt]/[Co] is obtained as:

$$R = \frac{[Pt]}{[Co]} = \frac{[N_i^{Pt\,I(306.47nm)} / N_i^{Pt\,I}]_{@GD=4\,\mu s}}{[N_i^{Co\,I(345.35nm)} / N_i^{Co\,I}]_{@GD=4\,\mu s}}$$

In this case, the estimated [Pt]/[Co]ratios for the samples are found to be: 1.13 ± 0.14 (PtCo1), 1.29 ± 0.19 (PtCo2), and 1.19 ± 0.14 (PtCo3). The uncertainties in SNRs, and plasma temperatures (T_{exc}) are considered for the error propagations here.

4.4.5 Comparison: LIBS vs ICP-OES

In this section, we verify our current LIBS results for the quantitative elemental ratios of the NA/NC samples studied here by comparing against the corresponding results obtained from standard ICP-OES measurements. Figure 4.16 plots the LIBS results for few estimated elemental stoichiometric ratios against those obtained from ICP measurements. Here, the red dashed line represents the ideal one-to-one correlation between the LIBS and ICP-OES results. As can be observed from Figure 4.16, the LIBS results are in good agreement with the values predicted from ICP-OES results. It needs to be highlighted here that we purposely chose to work with intermetallic nanomaterials that were synthesized with widely varying elemental ratios (~0.04-6.00) in order to test the robustness and accuracy of the quantitative LIBS analysis for characterizing NPs with a wide range of intermetallic compositions. The error bars in the LIBS have been calculated based on the error propagations due to uncertainties in plasma temperatures (T_{exc}), and shot-to-shot variations in the laser-induced plasma. It is worth mentioning that the samples with larger standard experimental errors indicated larger uncertainties.

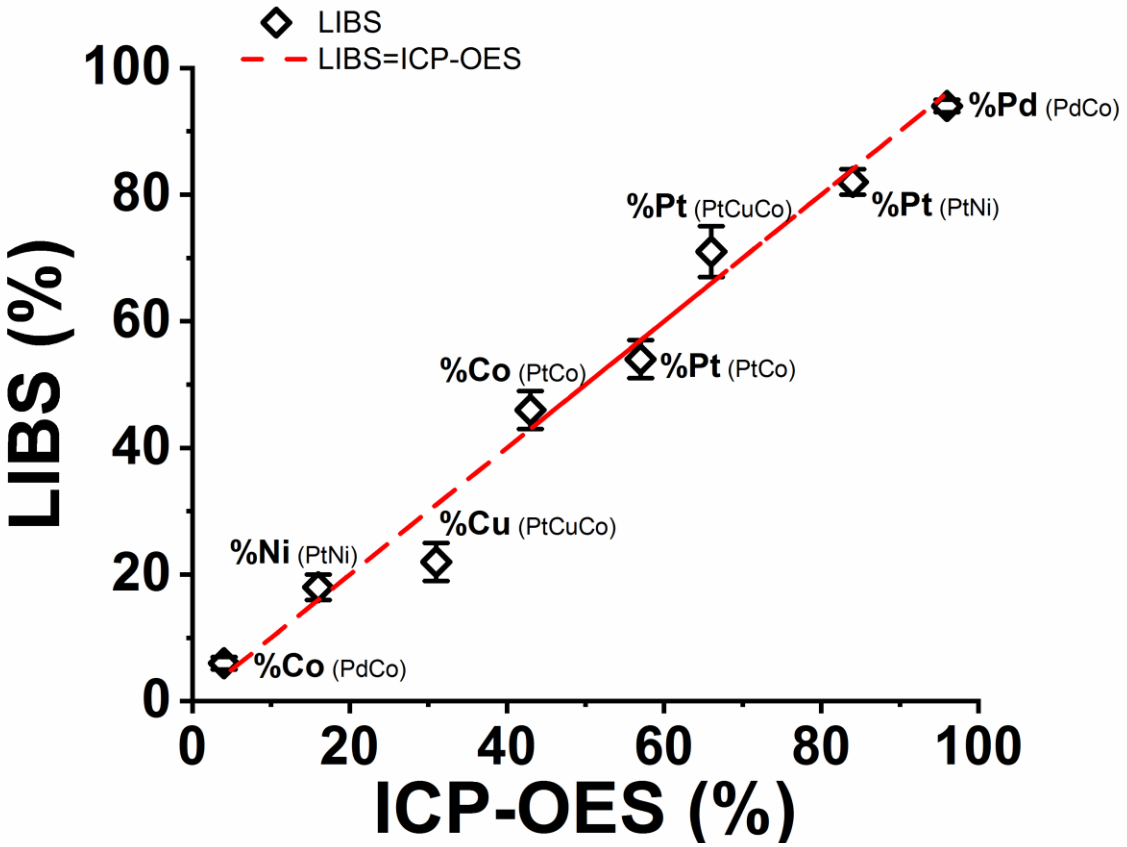

Figure 4.16: Comparison between quantitative LIBS and ICP-OES for number of elements studied in this chapter.

In regards, to the slight variations in the LIBS results from the ICP-OES measurements as observed in Figure 4.16 in some of the cases, one needs to bear in mind that the accuracy of quantitative LIBS analysis has an exponential dependence on the calculated plasma temperatures. Furthermore, self-absorptions can also affect the collected emission intensities and consequently the calculated temperatures. To this end, typically purging neutral gases such as argon and specially helium can thin the plasma considerably thereby reducing the self-absorption effects. However, our focus in the current study being on establishing the robustness and relative accuracy of LIBS for rapid and facile quantitative characterizations of intermetallic NPs, all our experiments were carried out under ambient conditions. Thus, considering the minimal sample preparation steps along with the

simplicity and rapidity of quantitative spectral analysis offered by LIBS, the deviations of our current results are satisfactory.

4.5 Conclusion

In this study, we demonstrate the application of LIBS for quantitative chemical characterizations of intermetallic nanoalloys (NAs), and nanocomposites (NCs) with sizes < 10–15 nm synthesized as electrocatalysts via our in-house developed laser ablation technique (LASiS-GRR). We employ an internal calibration methodology that involves effective normalizations of the analyte species densities by bulk species densities, both estimated from atomic emission lines at identical laser-induced plasma conditions, to carry out quantitative spectral analysis without the need for any external standards. The results from LIBS are in good agreement with those measured from ICP-OES. The minimal sample preparations and rapid measurement capabilities of LIBS, as compared to the time consuming steps and extensive acid digestion procedures involved with ICP-OES measurements, make it an ideal candidate for quantitative spectrochemical analysis of heterogeneous nanomaterials. Specifically, our results establish the promising potential of LIBS as the future analytical technique of choice for facile and rapid screening of intermetallic nanocatalysts designed with tailored structures and compositions.

Chapter 5 Conclusion and Future Works

5.1 Research Conclusions

The continuous efforts in the field of science and engineering to improve human life quality have culminated in the next-generation innovations in material science. To this end, the research embodied in the present thesis unfolded comprehensive experimental and computational studies to investigate the synthesis and characterization of composite and metal/intermetallic nanomaterials engineered with catalytic and energetic surface functionalities. Such novel classes of nanomaterials can find immediate applications in devices and systems designed for electrochemical energy conversions and solid-state pyro-techniques in combustion additives. As part of the overarching research mission of the Nano-BioMaterials Laboratory for Energy, Energetics and Environment (nbml-E3) at UT, this thesis specifically focused on the design, development and deployment of high-energy laser-based synthesis and spectrochemical techniques - for advanced investigation into the processing-structure-property relations of various composite nanomaterials that exhibit unique interfacial properties. Due to the numerous advantages of facile yet robust high-energy synthesis and characterization routes, as extensively discussed in the current thesis, the compilation of the original research contributions here have been dedicated to these techniques in regards to theoretical studies on the nucleation of metal nanoparticles via high-energy synthesis routes, implementation of laser ablation synthesis for generating novel composite energetic nanomaterials, and finally, spectrochemical characterization of composite and intermetallic nanomaterials via Laser Induced Breakdown Spectroscopy (LIBS).

In regards to the aforementioned research directions of this thesis, Chapter 2 was devoted to the development of a sophisticated KMC-based stochastic modeling to simulate the inception stage of

metal nanoparticle formation. This study provided valuable mechanistic insights into the fundamental physics of nanoparticle nucleation process during high-energy syntheses. The implications of such computational studies are far reaching when the experimental complexity of capturing the extremely short spatio-temporal scales of these rare events are taken into consideration. Specifically, we focused on the homogeneous nucleation of metallic nanoparticles computationally. The nature of the process demands for stochastic models that can capture the random events involved in nucleation. To this for the first time, we developed a kinetic Monte Carlo (KMC) enabled to describe the homogeneous nucleation without any priory assumptions. The evolution of clusters in time during the nucleation was analyzed. The size and nucleation rates of the primary particles were obtained through direct observations and the nucleation rates were compared to classical nucleation theory (CNT) indicating deviation from CNT prediction. The deviation from CNT agreed with previous similar molecular dynamics studies and the conditions for reaching the CNT predication were determined.

In Chapter 3, we employed laser ablation synthesis in solution (LASiS) for the production of shell-core metallic nanocomposites with engineered functionalities for energetic applications. Specifically, Al nanoparticles with carbon shell coatings were synthesized that showed that the size of these materials can be controlled systematically through LASiS method. The rationale behind these next generation nano-energetic designs rests on the fundamental hypothesis that the carbon coating on the reactive Al surface prevents the interfacial oxidation of the Al nanoparticles that is known to stymie their burn rates due to diffusion-limited species transport through the oxide ash layers. To this end, our collaborators from the US Army Research Laboratory (ARL) at Aberdeen Proving Ground, MD had employed Laser-induced air shock from energetic materials (LASEM) to determine the energetic activities of the as-synthesized metallic nanocomposites. The

results indicated that a rational tuning of their activities could be achieved by controlling the LASiS synthesis parameters.

Finally, a laser-based spectrochemical characterization of composite and intermetallic nanoparticles via laser-induced breakdown spectroscopy (LIBS) was developed and deployed in Chapter 4. Various catalytic materials such as intermetallic binary, ternary nanoalloys and nanocomposites were prepared through the LASiS method. The properties that determine catalytic activities such as size and morphology of the synthesized materials were analyzed using transmission electron microscopy (TEM). While the morphological characterizations were facilitated through TEM, chemical compositions were obtained using cumbersome techniques such as inductively-coupled plasma optical emission spectroscopy (ICP-OES). LIBS was employed for obtaining chemical compositions of these catalytic materials. A calibration-free approach was used to acquire the chemical compositions of various materials. The results were compared to ICP-OES measurements and good agreements were observed between both methods. It has been shown while the LIBS results are in a good agreement with ICP-OES, it does not need extensive steps involved in ICP-OES such as standard sample preparation for calibration, and sample digestion.

5.2 Future Works

For the future works, the KMC-based computational investigation of the homogenous nucleation of nanoparticles presented in Chapter 2 can be extended beyond the Classical Nucleation Theory (CNT) assumptions by incorporating the effects of size-dependent properties on the nucleation process. Till date, most CNT-based studies of homogeneous nucleation have largely relied on capillarity approximations (i.e., the assumption of constant surface tension properties for the bulk material) which end up being one of the most significant drawbacks in the investigation of

nucleation processes and their comparisons to any experimental results. But, based on the robust and self-reliant KMC model presented in this thesis, one can easily envision the development of a unified KMC model that for the first time can easily address the implementation of size-dependent nanoparticle properties without a priori assumptions. Furthermore, the brute force non-isothermal assumptions typically enforced in nucleation modeling can be negated in future by incorporating heat release effects during the condensation/evaporation processes through simple yet elegant energy balance in the current KMC model. Finally, the nucleation rates can be directly obtained and compared to experimental values after addressing those assumptions. Such an all-encompassing unified KMC model will provide the necessary channels for rational verification of experimentally observed vapor-phase homogenous nucleation events in near future. For the experimental parts of the thesis involved with the synthesis of shell-core nanoparticles as next generation energetic materials in Chapter 3, it would be useful to carry out comprehensive investigations for tuning the synthesis parameters such as annealing, laser re-ablation, laser wavelengths, secondary chemical reactions in solution-phase, etc. to control the sizes and morphologies of these core/shell structures to improve their pyrophoric behaviors. Moreover, synthesis and/or, post-processing of the carbon-coated Al nanoparticles under extreme pressure-temperature conditions or high-energy ion/electron bombardment might enable metastable phase transitions in both the Al and the carbon matrix to induce unique crystalline and/or, fullerene-like interlayered structures of the graphite. Such structures are known to withstand extremely large internal stresses and pressures, which in turn can tune the melting point and other thermophysical properties of the nanoparticles to tailor their interfacial energetic properties. Finally, in Chapter 4 in-situ LIBS can be directly combined with the LASiS process by collecting plasma emission signatures during the laser ablation synthesis of composite and intermetallic nanomaterials. Such

in-situ spectrochemical measurements collected from real-time LASiS-based synthesis will improve our fundamental understanding regarding the complex plasma physics that drives the bubble dynamics, evolution of the chemical compositions and the inception of nanoparticles via nucleation inside the cavitation bubble and the plasma-liquid interface.

References

1. van der Heijden, A.E.D.M., et al., *Processing, application and characterization of (ultra)fine and nanometric materials in energetic compositions.* Shock Compression of Condensed Matter - 2005, Pts 1 and 2, 2006. **845**: p. 1121-1126.
2. Berner, M.K., V.E. Zarko, and M.B. Talawar, *Nanoparticles of energetic materials: synthesis and properties (review).* Combustion Explosion and Shock Waves, 2013. **49**(6): p. 625-647.
3. Magnusson, M.H., K. Deppert, and J.O. Malm, *Single-crystalline tungsten nanoparticles produced by thermal decomposition of tungsten hexacarbonyl.* Journal of Materials Research, 2000. **15**(7): p. 1564-1569.
4. Ahonen, P.P., et al., *Mobility size development and the crystallization path during aerosol decomposition synthesis of TiO2 particles.* Journal of Aerosol Science, 2001. **32**(5): p. 615-630.
5. Lee, D. and M. Choi, *Coalescence enhanced synthesis of nanoparticles to control size, morphology and crystalline phase at high concentrations.* Journal of Aerosol Science, 2002. **33**(1): p. 1-16.
6. Nakaso, K., et al., *Evaluation of the change in the morphology of gold nanoparticles during sintering.* Journal of Aerosol Science, 2002. **33**(7): p. 1061-1074.
7. Urban, F.K., et al., *Nanophase films deposited from a high-rate, nanoparticle beam.* Journal of Vacuum Science & Technology B, 2002. **20**(3): p. 995-999.
8. Weber, A.P., M. Seipenbusch, and G. Kasper, *Application of aerosol techniques to study the catalytic formation of methane on gasborne nickel nanoparticles.* Journal of Physical Chemistry A, 2001. **105**(39): p. 8958-8963.
9. Nakata, Y., et al., *Particle dynamics during nanoparticle synthesis by laser ablation in a background gas.* Journal of Applied Physics, 2002. **91**(3): p. 1640-1643.
10. Anastas, P. and N. Eghbali, *Green Chemistry: Principles and Practice.* Chemical Society Reviews, 2010. **39**(1): p. 301-312.
11. Amendola, V. and M. Meneghetti, *Laser ablation synthesis in solution and size manipulation of noble metal nanoparticles.* Physical Chemistry Chemical Physics, 2009. **11**(20): p. 3805-3821.
12. Barcikowski, S., A. Hahn, and J. Walter, *Health risks of nanoparticulate emissions during femtosecond and picosecond pulsed laser machining.* Laser Applications in Microelectronic and Optoelectronic Manufacturing Vii, 2009. **7201**.
13. Tamura, A., et al., *Simultaneous observation of nascent plasma and bubble induced by laser ablation in water with various pulse durations.* Journal of Applied Physics, 2015. **117**(17).
14. Tanabe, R., et al., *Bubble dynamics in metal nanoparticle formation by laser ablation in liquid studied through high-speed laser stroboscopic videography.* Applied Surface Science, 2015. **351**: p. 327-331.
15. Zhang, D.S., B. Goekce, and S. Barcikowski, *Laser Synthesis and Processing of Colloids: Fundamentals and Applications.* Chemical Reviews, 2017. **117**(5): p. 3990-4103.
16. Soliman, W., N. Takada, and K. Sasaki, *Growth Processes of Nanoparticles in Liquid-Phase Laser Ablation Studied by Laser-Light Scattering.* Applied Physics Express, 2010. **3**(3).
17. Hu, S., et al., *PtCo/CoOx nanocomposites: Bifunctional electrocatalysts for oxygen reduction and evolution reactions synthesized via tandem laser ablation synthesis in solution-galvanic replacement reactions.* Applied Catalysis B-Environmental, 2016. **182**: p. 286-296.
18. Lam, J., et al., *Dynamical study of bubble expansion following laser ablation in liquids.* Applied Physics Letters, 2016. **108**(7).
19. Matsumoto, A., et al., *Transfer of the Species Dissolved in a Liquid into Laser Ablation Plasma: An Approach Using Emission Spectroscopy.* Journal of Physical Chemistry C, 2015. **119**(47): p. 26506-26511.
20. Hu, S., et al., *Tandem laser ablation synthesis in solution-galvanic replacement reaction (LASiS-GRR) for the production of PtCo nanoalloys as oxygen reduction electrocatalysts.* Journal of Power Sources, 2016. **306**: p. 413-423.
21. Saeta, P., et al., *Ultrafast Electronic Disordering during Femtosecond Laser Melting of Gaas.* Physical Review Letters, 1991. **67**(8): p. 1023-1026.

22. Siegal, Y., E.N. Glezer, and E. Mazur, *Dielectric-Constant of Gaas during a Subpicosecond Laser-Induced Phase-Transition.* Physical Review B, 1994. **49**(23): p. 16403-16406.
23. Borisov, O.V., X.L. Mao, and R.E. Russo, *Effects of crater development on fractionation and signal intensity during laser ablation inductively coupled plasma mass spectrometry.* Spectrochimica Acta Part B-Atomic Spectroscopy, 2000. **55**(11): p. 1693-1704.
24. Capitelli, M., F. Capitelli, and A. Eletskii, *Non-equilibrium and equilibrium problems in laser-induced plasmas.* Spectrochimica Acta Part B-Atomic Spectroscopy, 2000. **55**(6): p. 559-574.
25. Sun, L.X. and H.B. Yu, *Correction of self-absorption effect in calibration-free laser-induced breakdown spectroscopy by an internal reference method.* Talanta, 2009. **79**(2): p. 388-395.
26. Park, K., et al., *Size-resolved kinetic measurements of aluminum nanoparticle oxidation with single particle mass spectrometry.* Journal of Physical Chemistry B, 2005. **109**(15): p. 7290-7299.
27. Rao, C.N.R., et al., *Metal nanoparticles and their assemblies.* Chemical Society Reviews, 2000. **29**(1): p. 27-35.
28. Mukherjee, D. and S.A. Davari, *Computational Modeling for Fate, Transport and Evolution of Energetic Metal Nanoparticles Grown via Aerosol Route*, in *Energetic Materials*. 2017, Springer. p. 271-341.
29. Prakash, A., A.P. Bapat, and M.R. Zachariah, *A simple numerical algorithm and software for solution of nucleation, surface growth, and coagulation problems.* Aerosol Science and Technology, 2003. **37**(11): p. 892-898.
30. Girshick, S.L., P. Agarwal, and D.G. Truhlar, *Homogeneous nucleation with magic numbers: Aluminum.* Journal of Chemical Physics, 2009. **131**(13).
31. Li, Z.H., et al., *Free energies of formation of metal clusters and nanoparticles from molecular simulations: Al-n with n=2-60.* Journal of Physical Chemistry C, 2007. **111**(44): p. 16227-16242.
32. Oxtoby, D.W., *Homogeneous nucleation: theory and experiment.* Journal of Physics: Condensed Matter, 1992. **4**(38): p. 7627.
33. Widiyastuti, W., et al., *Nanoparticle Formation Through Solid-Fed Flame Synthesis: Experiment and Modeling.* Aiche Journal, 2009. **55**(4): p. 885-895.
34. Mueller, R., et al., *Growth of zirconia particles made by flame spray pyrolysis.* Aiche Journal, 2004. **50**(12): p. 3085-3094.
35. Madler, L., et al., *Controlled synthesis of nanostructured particles by flame spray pyrolysis.* Journal of Aerosol Science, 2002. **33**(2): p. 369-389.
36. Valeriani, C., et al., *Computing stationary distributions in equilibrium and nonequilibrium systems with forward flux sampling.* Journal of Chemical Physics, 2007. **127**(11).
37. Auer, S. and D. Frenkel, *Prediction of absolute crystal-nucleation rate in hard-sphere colloids.* Nature, 2001. **409**(6823): p. 1020-1023.
38. Allen, R.J., C. Valeriani, and P.R. ten Wolde, *Forward flux sampling for rare event simulations.* Journal of Physics-Condensed Matter, 2009. **21**(46).
39. Finney, E.E. and R.G. Finke, *Nanocluster nucleation and growth kinetic and mechanistic studies: A review emphasizing transition-metal nanoclusters.* Journal of Colloid and Interface Science, 2008. **317**(2): p. 351-374.
40. Rusyniak, M., et al., *Vapor phase homogeneous nucleation of higher alkanes: Dodecane, hexadecane, and octadecane. 1. Critical supersaturation and nucleation rate measurements.* Journal of Physical Chemistry B, 2001. **105**(47): p. 11866-11872.
41. Girshick, S.L. and C.P. Chiu, *Homogeneous Nucleation of Particles from the Vapor-Phase in Thermal Plasma Synthesis.* Plasma Chemistry and Plasma Processing, 1989. **9**(3): p. 355-369.
42. Katz, J.L., *Condensation of a Supersaturated Vapor .1. Homogeneous Nucleation of Normal-Alkanes.* Journal of Chemical Physics, 1970. **52**(9): p. 4733-&.
43. Katz, J.L., et al., *Condensation of a supersaturated vapor. III. The homogeneous nucleation of CCl4, CHCl3, CCl3F, and C2H2Cl4.* The Journal of Chemical Physics, 1976. **65**(1): p. 382-392.

44. McClurg, R.B., R.C. Flagan, and W.A. Goddard, *Thermodynamic properties and homogeneous nucleation for surface-melted physical clusters.* Journal of Chemical Physics, 1996. **105**(17): p. 7648-7663.
45. McClurg, R.B. and R.C. Flagan, *Critical comparison of droplet models in homogeneous nucleation theory.* Journal of Colloid and Interface Science, 1998. **201**(2): p. 194-199.
46. Mukherjee, D., A. Prakash, and M.R. Zachariah, *Implementation of a discrete nodal model to probe the effect of size-dependent surface tension on nanoparticle formation and growth.* Journal of Aerosol Science, 2006. **37**(10): p. 1388-1399.
47. Palmer, J.C. and P.G. Debenedetti, *Recent Advances in Molecular Simulation: A Chemical Engineering Perspective.* Aiche Journal, 2015. **61**(2): p. 370-383.
48. Li, Z.H. and D.G. Truhlar, *Cluster and nanoparticle condensation and evaporation reactions. Thermal rate constants and equilibrium constants of Al(m)+Al(n-m)<-> Al(n) with n=2-60 and m=1-8.* Journal of Physical Chemistry C, 2008. **112**(30): p. 11109-11121.
49. Panda, S. and S.E. Pratsinis, *Modeling the Synthesis of Aluminum Particles by Evaporation-Condensation in an Aerosol Flow Reactor.* Nanostructured Materials, 1995. **5**(7-8): p. 755-767.
50. Delgoshaie, A.H., P. Jenny, and H.A. Tchelepi, *Temporal Markov Processes for Transport in Porous Media: Random Lattice Networks.* arXiv preprint arXiv:1708.04173, 2017.
51. Shizgal, B. and J.C. Barrett, *Time-Dependent Nucleation.* Journal of Chemical Physics, 1989. **91**(10): p. 6505-6518.
52. Davari, S.A. and D. Mukherjee, *Kinetic Monte Carlo simulation for homogeneous nucleation of metal nanoparticles during vapor phase synthesis.* Aiche Journal, 2018. **64**(1): p. 18-28.
53. Efendiev, Y. and M.R. Zachariah, *Hierarchical hybrid Monte-Carlo method for simulation of two-component aerosol nucleation, coagulation and phase segregation.* Journal of Aerosol Science, 2003. **34**(2): p. 169-188.
54. Kruis, F.E., A. Maisels, and H. Fissan, *Direct simulation Monte Carlo method for particle coagulation and aggregation.* Aiche Journal, 2000. **46**(9): p. 1735-1742.
55. Liffman, K., *A Direct Simulation Monte-Carlo Method for Cluster Coagulation.* Journal of Computational Physics, 1992. **100**(1): p. 116-127.
56. Shah, B.H., D. Ramkrishna, and J.D. Borwanker, *Simulation of Particulate Systems Using Concept of Interval of Quiescence.* Aiche Journal, 1977. **23**(6): p. 897-904.
57. Gillespie, D.T., *Exact Method for Numerically Simulating Stochastic Coalescence Process in a Cloud.* Journal of the Atmospheric Sciences, 1975. **32**(10): p. 1977-1989.
58. Maisels, A., F.E. Kruis, and H. Fissan, *Direct simulation Monte Carlo for simultaneous nucleation, coagulation, and surface growth in dispersed systems.* Chemical Engineering Science, 2004. **59**(11): p. 2231-2239.
59. Mukherjee, D., C.G. Sonwane, and M.R. Zachariah, *Kinetic Monte Carlo simulation of the effect of coalescence energy release on the size and shape evolution of nanoparticles grown as an aerosol.* Journal of Chemical Physics, 2003. **119**(6): p. 3391-3404.
60. Smith, M. and T. Matsoukas, *Constant-number Monte Carlo simulation of population balances.* Chemical Engineering Science, 1998. **53**(9): p. 1777-1786.
61. Bahadur, R. and R.B. McClurg, *Comparison of cluster definitions in homogeneous nucleation rate calculations.* Journal of Physical Chemistry B, 2001. **105**(47): p. 11893-11900.
62. Chkonia, G., et al., *Evaluating nucleation rates in direct simulations.* Journal of Chemical Physics, 2009. **130**(6).
63. Reddy, V.S., et al., *Carrier transport mechanism in aluminum nanoparticle embedded AlQ(3) structures for organic bistable memory devices.* Organic Electronics, 2009. **10**(1): p. 138-144.
64. Zhong, X.L., W.L.E. Wong, and M. Gupta, *Enhancing strength and ductility of magnesium by integrating it with aluminum nanoparticles.* Acta Materialia, 2007. **55**(18): p. 6338-6344.
65. Liang, G. and S.C. Tjong, *Electrical conducting behavior of polyethylene composites filled with self-passivated aluminum nanoparticles and carbon nanotubes.* Advanced Engineering Materials, 2007. **9**(11): p. 1014-1017.

66. Tepper, F. and G.V. Ivanov, *'ACTIVATED' ALUMINUM AS A STORED ENERGY SOURCE FOR PROPELLANTS.* 1997. **4**(1-6): p. 636-645.
67. Sun, J., M.L. Pantoya, and S.L. Simon, *Dependence of size and size distribution on reactivity of aluminum nanoparticles in reactions with oxygen and MoO3.* Thermochimica Acta, 2006. **444**(2): p. 117-127.
68. Trunov, M.A., et al., *Oxidation and melting of aluminum nanopowders.* Journal of Physical Chemistry B, 2006. **110**(26): p. 13094-13099.
69. Mukherjee, D., M. Wang, and B. Khomami, *Impact of particle morphology on surface oxidation of nanoparticles: A kinetic Monte Carlo based study.* Aiche Journal, 2012. **58**(11): p. 3341-3353.
70. Russo, M.F., et al., *Molecular dynamic simulation of aluminum-water reactions using the ReaxFF reactive force field.* International Journal of Hydrogen Energy, 2011. **36**(10): p. 5828-5835.
71. Vashishta, P., R.K. Kalia, and A. Nakano, *Multimillion atom simulations of dynamics of oxidation of an aluminum nanoparticle and nanoindentation on ceramics.* Journal of Physical Chemistry B, 2006. **110**(8): p. 3727-3733.
72. Julin, J., I. Napari, and H. Vehkamaki, *Comparative study on methodology in molecular dynamics simulation of nucleation.* Journal of Chemical Physics, 2007. **126**(22).
73. Yasuoka, K. and M. Matsumoto, *Molecular dynamics of homogeneous nucleation in the vapor phase. I. Lennard-Jones fluid.* Journal of Chemical Physics, 1998. **109**(19): p. 8451-8462.
74. Wedekind, J., et al., *Nucleation rate isotherms of argon from molecular dynamics simulations.* Journal of Chemical Physics, 2007. **127**(15).
75. Wedekind, J., R. Strey, and D. Reguera, *New method to analyze simulations of activated processes.* Journal of Chemical Physics, 2007. **126**(13).
76. Mench, M., C. Yeh, and K. Kuo, *Propellant burning rate enhancement and thermal behavior of ultra-fine aluminum powders(Alex).* Energetic materials- Production, processing and characterization, 1998: p. 30-1.
77. Chiaverini, M.J., et al., *Instantaneous regression behavior of HTPB solid fuels burning with GOX in a simulated hybrid rocket motor.* International Journal of Energetic Materials and Chemical Propulsion, 1997. **4**(1-6).
78. Renie, J., et al., *Aluminum particle combustion in composite solid propellants.* Purdue University, West Lafayette, Ind, 1982.
79. Bakhman, N., A. Belyaev, and Y.A. Kondrashkov, *Influence of the metal additives onto the burning rate of the model solid rocket propellants.* Phys Combust Explos, 1970. **6**: p. 93.
80. Ritter, H. and S. Braun, *High explosives containing ultrafine aluminum ALEX.* Propellants, Explosives, Pyrotechnics, 2001. **26**(6): p. 311-314.
81. Ilyin, A., et al., *Characterization of aluminum powders I. Parameters of reactivity of aluminum powders.* Propellants Explosives Pyrotechnics, 2002. **27**(6): p. 361-364.
82. Brousseau, P. and C.J. Anderson, *Nanometric aluminum in explosives.* Propellants Explosives Pyrotechnics, 2002. **27**(5): p. 300-306.
83. Weiser, V., S. Kelzenberg, and N. Eisenreich, *Influence of the metal particle size on the ignition of energetic materials.* Propellants Explosives Pyrotechnics, 2001. **26**(6): p. 284-289.
84. Rai, A., et al., *Understanding the mechanism of aluminium nanoparticle oxidation.* Combustion Theory and Modelling, 2006. **10**(5): p. 843-859.
85. GEN, M., M. Ziskin, and I. PETROV, *A study of the dispersion of aluminium aerosols as dependent on the conditions of their formation.* Doklady Akademii Nauk SSSR, 1959. **127**(2): p. 366-368.
86. Tillotson, T.M., et al., *Nanostructured energetic materials using sol-gel methodologies.* Journal of Non-Crystalline Solids, 2001. **285**(1-3): p. 338-345.
87. Dreizin, E.L., *Metal-based reactive nanomaterials.* Progress in Energy and Combustion Science, 2009. **35**(2): p. 141-167.
88. Prakash, A., A.V. McCormick, and M.R. Zachariah, *Tuning the reactivity of energetic nanoparticles by creation of a core-shell nanostructure.* Nano Letters, 2005. **5**(7): p. 1357-1360.

89. Park, K., A. Rai, and M.R. Zachariah, *Characterizing the coating and size-resolved oxidative stability of carbon-coated aluminum nanoparticles by single-particle mass-spectrometry*. Journal of Nanoparticle Research, 2006. **8**(3-4): p. 455-464.
90. Shahravan, A., T. Desai, and T. Matsoukas, *Passivation of Aluminum Nanoparticles by Plasma-Enhanced Chemical Vapor Deposition for Energetic Nanomaterials.* Acs Applied Materials & Interfaces, 2014. **6**(10): p. 7942-7947.
91. Atmane, Y.A., et al., *Functionalization of Aluminum Nanoparticles Using a Combination of Aryl Diazonium Salt Chemistry and Iniferter Method.* Journal of Physical Chemistry C, 2013. **117**(49): p. 26000-26006.
92. Meziani, M.J., et al., *Formation and Properties of Stabilized Aluminum Nanoparticles.* Acs Applied Materials & Interfaces, 2009. **1**(3): p. 703-709.
93. Baladi, A. and R.S. Mamoory, *Investigation of different liquid media and ablation times on pulsed laser ablation synthesis of aluminum nanoparticles.* Applied Surface Science, 2010. **256**(24): p. 7559-7564.
94. Kuladeep, R., et al., *Investigation of optical limiting properties of Aluminium nanoparticles prepared by pulsed laser ablation in different carrier media.* Journal of Applied Physics, 2013. **114**(24).
95. Viau, G., et al., *Internal structure of Al hollow nanoparticles generated by laser ablation in liquid ethanol.* Chemical Physics Letters, 2011. **501**(4-6): p. 419-422.
96. Gottfried, J.L., *Laboratory-Scale Method for Estimating Explosive Performance from Laser-Induced Shock Waves.* Propellants Explosives Pyrotechnics, 2015. **40**(5): p. 674-681.
97. Gottfried, J.L., T.M. Klapotke, and T.G. Witkowski, *Estimated Detonation Velocities for TKX-50, MAD-X1, BDNAPM, BTNPM, TKX-55, and DAAF using the Laser-induced Air Shock from Energetic Materials Technique*. Propellants Explosives Pyrotechnics, 2017. **42**(4): p. 353-359.
98. Gottfried, J.L. and E.J. Bukowski, *Laser-shocked energetic materials with metal additives: evaluation of chemistry and detonation performance.* Applied Optics, 2017. **56**(3): p. B47-B57.
99. Hu, S., C. Melton, and D. Mukherjee, *A facile route for the synthesis of nanostructured oxides and hydroxides of cobalt using laser ablation synthesis in solution (LASIS).* Physical Chemistry Chemical Physics, 2014. **16**(43): p. 24034-24044.
100. Gottfried, J.L., *Influence of exothermic chemical reactions on laser-induced shock waves.* Physical Chemistry Chemical Physics, 2014. **16**(39): p. 21452-21466.
101. Gottfried, J.L., *Method for estimating detonation performance of materials*. 2017, Google Patents.
102. Zhang, P.F., et al., *One-Pot Synthesis of Ternary Pt-Ni-Cu Nanocrystals with High Catalytic Performance.* Chemistry of Materials, 2015. **27**(18): p. 6402-6410.
103. Zhu, H.Y., et al., *Synthetic Control of FePtM Nanorods (M = Cu, Ni) To Enhance the Oxygen Reduction Reaction.* Journal of the American Chemical Society, 2013. **135**(19): p. 7130-7133.
104. Luo, J., et al., *Ternary alloy nanoparticles with controllable sizes and composition and electrocatalytic activity.* Journal of Materials Chemistry, 2006. **16**(17): p. 1665-1673.
105. Scofield, M.E., et al., *Tailoring the composition of ultrathin, ternary alloy PtRuFe nanowires for the methanol oxidation reaction and formic acid oxidation reaction.* Energy & Environmental Science, 2015. **8**(1): p. 350-363.
106. Matin, M.A., et al., *Rational syntheses of core-shell Fe@(PtRu) nanoparticle electrocatalysts for the methanol oxidation reaction with complete suppression of CO-poisoning and highly enhanced activity.* Journal of Materials Chemistry A, 2015. **3**(33): p. 17154-17164.
107. Wang, D.Y., et al., *Simple Replacement Reaction for the Preparation of Ternary Fe1-xPtRux Nanocrystals with Superior Catalytic Activity in Methanol Oxidation Reaction.* Journal of the American Chemical Society, 2012. **134**(24): p. 10011-10020.
108. Zhu, Y.L., et al., *A Universal and Facile Way for the Development of Superior Bifunctional Electrocatalysts for Oxygen Reduction and Evolution Reactions Utilizing the Synergistic Effect.* Chemistry-a European Journal, 2014. **20**(47): p. 15533-15542.

109. Sa, Y.J., et al., *Ordered mesoporous Co3O4 spinels as stable, bifunctional, noble metal-free oxygen electrocatalysts.* Journal of Materials Chemistry A, 2013. **1**(34): p. 9992-10001.
110. Gorlin, Y. and T.F. Jaramillo, *A Bifunctional Nonprecious Metal Catalyst for Oxygen Reduction and Water Oxidation.* Journal of the American Chemical Society, 2010. **132**(39): p. 13612-13614.
111. Wang, D.L., et al., *Structurally ordered intermetallic platinum-cobalt core-shell nanoparticles with enhanced activity and stability as oxygen reduction electrocatalysts.* Nature Materials, 2013. **12**(1): p. 81-87.
112. Koh, S., M.F. Toney, and P. Strasser, *Activity-stability relationships of ordered and disordered alloy phases of Pt3Co electrocatalysts for the oxygen reduction reaction (ORR).* Electrochimica Acta, 2007. **52**(8): p. 2765-2774.
113. Hwang, B.J., et al., *An investigation of structure-catalytic activity relationship for Pt-Co/C bimetallic nanoparticles toward the oxygen reduction reaction.* Journal of Physical Chemistry C, 2007. **111**(42): p. 15267-15276.
114. Zignani, S.C., E. Antolini, and E.R. Gonzalez, *Evaluation of the stability and durability of Pt and Pt-Co/C catalysts for polymer electrolyte membrane fuel cells.* Journal of Power Sources, 2008. **182**(1): p. 83-90.
115. Tighe, M., et al., *Comparison of digestion methods for ICP-OES analysis of a wide range of analytes in heavy metal contaminated soil samples with specific reference to arsenic and antimony.* Communications in Soil Science and Plant Analysis, 2004. **35**(9-10): p. 1369-1385.
116. Borisov, O.V., et al., *Determination of platinum, palladium, rhodium and titanium in automotive catalytic converters using inductively coupled plasma mass spectrometry with liquid nebulization.* Journal of Analytical Atomic Spectrometry, 1997. **12**(2): p. 239-246.
117. Lomer, M.C.E., et al., *Determination of titanium dioxide in foods using inductively coupled plasma optical emission spectrometry.* Analyst, 2000. **125**(12): p. 2339-2343.
118. Radziemski, L.J. and D.A. Cremers, *Spectrochemical analysis using laser plasma excitation*, in *Laser-induced plasmas and applications*. 1989.
119. Hahn, D.W. and N. Omenetto, *Laser-Induced Breakdown Spectroscopy (LIBS), Part II: Review of Instrumental and Methodological Approaches to Material Analysis and Applications to Different Fields.* Applied Spectroscopy, 2012. **66**(4): p. 347-419.
120. Mukherjee, D., A. Rai, and M.R. Zachariah, *Quantitative laser-induced breakdown spectroscopy for aerosols via internal calibration: Application to the oxidative coating of aluminum nanoparticles.* Journal of Aerosol Science, 2006. **37**(6): p. 677-695.
121. Davari, S.A., S. Hu, and D. Mukherjee, *Calibration-free quantitative analysis of elemental ratios in intermetallic nanoalloys and nanocomposites using Laser Induced Breakdown Spectroscopy (LIBS).* Talanta, 2017. **164**: p. 330-340.
122. Hu, S., et al., *Hybrid nanocomposites of nanostructured Co3O4 interfaced with reduced/nitrogen-doped graphene oxides for selective improvements in electrocatalytic and/or supercapacitive properties.* Rsc Advances, 2017. **7**(53): p. 33166-33176.
123. Davari, S.A., et al., *Rapid elemental composition analysis of intermetallic ternary nanoalloys using calibration-free quantitative Laser Induced Breakdown Spectroscopy (LIBS).* Mrs Advances, 2017. **2**(55): p. 3371-3376.
124. Gottfried, J.L., et al., *Standoff detection of chemical and biological threats using laser-induced breakdown spectroscopy.* Applied Spectroscopy, 2008. **62**(4): p. 353-363.
125. Cremers, D.A., et al., *Measuring total soil carbon with laser-induced breakdown spectroscopy (LIBS).* Journal of Environmental Quality, 2001. **30**(6): p. 2202-2206.
126. Mukherjee, D. and M.D. Cheng, *Quantitative analysis of carbonaceous aerosols using laser-induced breakdown spectroscopy: a study on mass loading induced plasma matrix effects.* Journal of Analytical Atomic Spectrometry, 2008. **23**(1): p. 119-128.
127. Naes, B.E., et al., *A comparison of laser ablation inductively coupled plasma mass spectrometry, micro X-ray fluorescence spectroscopy, and laser induced breakdown spectroscopy for the*

discrimination of automotive glass. Spectrochimica Acta Part B-Atomic Spectroscopy, 2008. **63**(10): p. 1145-1150.
128. De Lucia, F.C. and J.L. Gottfried, *Influence of Molecular Structure on the Laser-Induced Plasma Emission of the Explosive RDX and Organic Polymers.* Journal of Physical Chemistry A, 2013. **117**(39): p. 9555-9563.
129. Gottfried, J.L., et al., *Laser-induced breakdown spectroscopy for detection of explosives residues: a review of recent advances, challenges, and future prospects.* Analytical and Bioanalytical Chemistry, 2009. **395**(2): p. 283-300.
130. Davari, S.A., et al., *Calibration-free quantitative analysis of thin-film oxide layers in semiconductors using laser induced breakdown spectroscopy (LIBS).* Journal of Analytical Atomic Spectrometry, 2017. **32**(7): p. 1378-1387.
131. Mukherjee, D. and M.D. Cheng, *Characterization of carbon-containing aerosolized drugs using laser-induced breakdown spectroscopy.* Applied Spectroscopy, 2008. **62**(5): p. 554-562.
132. Davari, S.A., et al., *In-vitro analysis of early calcification in aortic valvular interstitial cells using Laser-Induced Breakdown Spectroscopy (LIBS).* Journal of biophotonics, 2018. **11**(1).
133. Sattmann, R., V. Sturm, and R. Noll, *Laser-Induced Breakdown Spectroscopy of Steel Samples Using Multiple Q-Switch Nd-Yag Laser-Pulses.* Journal of Physics D-Applied Physics, 1995. **28**(10): p. 2181-2187.
134. Kim, D.E., et al., *Quantitative analysis of aluminum impurities in zinc alloy by laser-induced breakdown spectroscopy.* Applied Spectroscopy, 1997. **51**(1): p. 22-29.
135. Li, J.M., et al., *Determination of cobalt in low-alloy steels using laser-induced breakdown spectroscopy combined with laser-induced fluorescence.* Talanta, 2016. **151**: p. 234-238.
136. Hahn, D.W. and M.M. Lunden, *Detection and analysis of aerosol particles by laser-induced breakdown spectroscopy.* Aerosol Science and Technology, 2000. **33**(1-2): p. 30-48.
137. Hahn, D.W., *Laser-induced breakdown spectroscopy for sizing and elemental analysis of discrete aerosol particles.* Applied Physics Letters, 1998. **72**(23): p. 2960-2962.
138. Carranza, J.E. and D.W. Hahn, *Assessment of the upper particle size limit for quantitative analysis of aerosols using laser-induced breakdown spectroscopy.* Analytical Chemistry, 2002. **74**(21): p. 5450-5454.
139. Kebede, A., et al., *Controlled synthesis, characterization, and application of iron oxide nanoparticles for oral delivery of insulin.* Lasers in Medical Science, 2013. **28**(2): p. 579-587.
140. Zhang, Y.Y., et al., *A new diagnostic for volume fraction measurement of metal-oxide nanoparticles in flames using phase-selective laser-induced breakdown spectroscopy.* Proceedings of the Combustion Institute, 2015. **35**: p. 3681-3688.
141. Serrano, J., et al., *Potential of laser-induced breakdown spectroscopy for discrimination of nano-sized carbon materials. Insights on the optical characterization of graphene.* Spectrochimica Acta Part B: Atomic Spectroscopy, 2014. **97**: p. 105-112.
142. Petrovic, S., et al., *Agglomeration in core-shell structure of CuAg nanoparticles synthesized by the laser ablation of Cu target in aqueous solutions.* Journal of Optics, 2015. **17**(2).
143. Kadel, K. and W.Z. Li, *Solvothermal synthesis and structural characterization of unfilled and Yb-filled cobalt antimony skutterudite.* Crystal Research and Technology, 2014. **49**(2-3): p. 135-141.
144. Tognoni, E., et al., *Calibration-Free Laser-Induced Breakdown Spectroscopy: State of the art.* Spectrochimica Acta Part B-Atomic Spectroscopy, 2010. **65**(1): p. 1-14.
145. Ciucci, A., et al., *New procedure for quantitative elemental analysis by laser-induced plasma spectroscopy.* Applied Spectroscopy, 1999. **53**(8): p. 960-964.
146. Kramida, A., Ralchenko, Yu., Reader, J. and NIST ASD Team. *NIST Atomic Spectra Database (version 5.3)*. [[Online]] 2015; Available from: http://physics.nist.gov/asd
147. Tognoni, E. and G. Cristoforetti, *[INVITED] Signal and noise in Laser Induced Breakdown Spectroscopy: An introductory review.* Optics and Laser Technology, 2016. **79**: p. 164-172.
148. Radziemski, L.J., et al., *Time-Resolved Laser-Induced Breakdown Spectrometry of Aerosols.* Analytical Chemistry, 1983. **55**(8): p. 1246-1252.

149. Den Hartog, E.A., et al., *Improved laboratory transition probabilities for PtI and application to the platinum abundances of BD+17 degrees 3248 and the Sun.* Astrophysical Journal, 2005. **619**(1): p. 639-655.
150. Persons, T.M., et al., *Nanomanufacturing: emergence and implications for US competitiveness, the environment, and human health.* 2014.
151. Mudryi, A.V., et al., *Structural and optical properties of thin films of Cu(In,Ga)Se-2 semiconductor compounds.* Journal of Applied Spectroscopy, 2010. **77**(3): p. 371-377.
152. Dullweber, T., et al., *Study of the effect of gallium grading in Cu(In,Ga)Se-2.* Thin Solid Films, 2000. **361**: p. 478-481.
153. Wei, S.H., S.B. Zhang, and A. Zunger, *Effects of Ga addition to CuInSe2 on its electronic, structural, and defect properties.* Applied Physics Letters, 1998. **72**(24): p. 3199-3201.
154. Macdonald, D., et al., *Light-induced boron-oxygen defect generation in compensated p-type Czochralski silicon.* Journal of Applied Physics, 2009. **105**(9).
155. Falster, R. and V.V. Voronkov, *On the properties of the intrinsic point defects in silicon: A perspective from crystal growth and wafer processing.* Physica Status Solidi B-Basic Research, 2000. **222**(1): p. 219-244.
156. Chen, J.H., et al., *Rapid-thermal-anneal-based internal gettering for germanium-doped Czochralski silicon.* Applied Physics a-Materials Science & Processing, 2009. **94**(4): p. 905-910.
157. Kim, I.G. and J.S. Kwon, *Reduction of grown-in defects by vacancy-assisted oxygen precipitation in high density dynamic random access memory.* Applied Physics Letters, 2003. **83**(23): p. 4863-4865.
158. Yang, X.Y., B. Lee, and V. Misra, *High Mobility 4H-SiC Lateral MOSFETs Using Lanthanum Silicate and Atomic Layer Deposited SiO2.* Ieee Electron Device Letters, 2015. **36**(4): p. 312-314.
159. Shen, X., S. Dhar, and S.T. Pantelides, *Atomic origin of high-temperature electron trapping in metal-oxide-semiconductor devices.* Applied Physics Letters, 2015. **106**(14).
160. Chanthaphan, A., et al., *Improved bias-temperature instability characteristics in SiC metal-oxide-semiconductor devices with aluminum oxynitride dielectrics.* Applied Physics Letters, 2014. **104**(12).
161. Wang, Y.C., et al., *Investigation of Leakage Current Mechanisms in La2O3/SiO2/4H-SiC MOS Capacitors with Varied SiO2 Thickness.* Journal of Electronic Materials, 2016. **45**(11): p. 5600-5605.
162. Durose, K., et al., *Physical characterization of thin-film solar cells.* Progress in Photovoltaics, 2004. **12**(2-3): p. 177-217.
163. Jackson, P., et al., *New world record efficiency for Cu(In,Ga)Se-2 thin-film solar cells beyond 20%.* Progress in Photovoltaics, 2011. **19**(7): p. 894-897.
164. Martinuzzi, S., et al., *n-Type Multicrystalline Silicon Wafers Prepared from Plasma Torch Refined Upgraded Metallurgical Feedstock.* Progress in Photovoltaics, 2009. **17**(5): p. 297-305.
165. Darwiche, S., et al., *Laser-induced breakdown spectroscopy for photovoltaic silicon wafer analysis.* Progress in Photovoltaics, 2012. **20**(4): p. 463-471.
166. Lee, S.H., et al., *Ablation and Spectroscopic Characteristics of Thin CuIn1-xGaxSe2 Solar Cell Films Fabricated by Co-Evaporation and Co-Sputtering Processes.* International Journal of Precision Engineering and Manufacturing-Green Technology, 2014. **1**(1): p. 17-24.
167. Bol'shakov, A.A., et al., *Laser-induced breakdown spectroscopy in industrial and security applications.* Applied Optics, 2010. **49**(13): p. C132-C142.
168. Liu, Z.X., A. Masuda, and M. Kondo, *Investigation on the crystal growth process of spherical Si single crystals by melting.* Journal of Crystal Growth, 2009. **311**(16): p. 4116-4122.
169. Veve, C., M. Stemmer, and S. Martinuzzi, *Oxygen precipitates in annealed CZ silicon wafers detected by SIRM and FTIR spectroscopy.* Materials Science and Engineering B-Solid State Materials for Advanced Technology, 1996. **36**(1-3): p. 200-203.

170. Hill, D.E., *Determination of Interstitial Oxygen Concentration in Low-Resistivity N-Type Silicon-Wafers by Infrared-Absorption Measurements.* Journal of the Electrochemical Society, 1990. **137**(12): p. 3926-3928.
171. Hartstein, A. and N.F. Albert, *Determination of the Inversion-Layer Thickness from Capacitance Measurements of Metal-Oxide-Semiconductor Field-Effect Transistors with Ultrathin Oxide Layers.* Physical Review B, 1988. **38**(2): p. 1235-1240.
172. Sodini, C.G., T.W. Ekstedt, and J.L. Moll, *Charge Accumulation and Mobility in Thin Dielectric Mos-Transistors.* Solid-State Electronics, 1982. **25**(9): p. 833-841.
173. Liang, M.S., et al., *Inversion-Layer Capacitance and Mobility of Very Thin Gate-Oxide Mosfets.* Ieee Transactions on Electron Devices, 1986. **33**(3): p. 409-413.
174. Ferioli, F., P.V. Puzinauskas, and S.G. Buckley, *Laser-induced breakdown spectroscopy for on-line engine equivalence ratio measurements.* Applied Spectroscopy, 2003. **57**(9): p. 1183-1189.
175. Wisbrun, R., et al., *Detector for Trace Elemental Analysis of Solid Environmental-Samples by Laser-Plasma Spectroscopy.* Analytical Chemistry, 1994. **66**(18): p. 2964-2975.
176. Gottfried, J.L., *Influence of metal substrates on the detection of explosive residues with laser-induced breakdown spectroscopy.* Applied Optics, 2013. **52**(4): p. B10-B19.
177. Owens, T., et al., *Ultrafast thin-film laser-induced breakdown spectroscopy of doped oxides.* Applied Optics, 2010. **49**(13): p. C67-C69.
178. Lee, S.H., et al., *Analysis of the absorption layer of CIGS solar cell by laser-induced breakdown spectroscopy.* Applied Optics, 2012. **51**(7): p. B115-B120.
179. Axente, E., et al., *Accurate analysis of indium-zinc oxide thin films via laser-induced breakdown spectroscopy based on plasma modeling.* Journal of Analytical Atomic Spectrometry, 2014. **29**(3): p. 553-564.
180. Popescu, A.C., et al., *Analysis of indium zinc oxide thin films by laser-induced breakdown spectroscopy.* Journal of Applied Physics, 2011. **110**(8).
181. Banerjee, S.P., et al., *Characterization of organic photovoltaic devices using femtosecond laser induced breakdown spectroscopy.* Applied Surface Science, 2017. **418**: p. 542-547.
182. Lindman, B.R., R.O. Bonow, and C.M. Otto, *Current Management of Calcific Aortic Stenosis.* Circulation Research, 2013. **113**(2): p. 223-237.
183. Rajamannan, N.M., et al., *Human aortic valve calcification is associated with an osteoblast phenotype.* Circulation, 2003. **107**(17): p. 2181-2184.
184. Freeman, R.V. and C.M. Otto, *Spectrum of calcific aortic valve disease pathogenesis, disease progression, and treatment strategies.* Circulation, 2005. **111**(24): p. 3316-3326.
185. Mohler, E.R., *Mechanisms of aortic valve calcification.* The American journal of cardiology, 2004. **94**(11): p. 1396-1402.
186. Schoen, F.J., *Evolving Concepts of Cardiac Valve Dynamics The Continuum of Development, Functional Structure, Pathobiology, and Tissue Engineering.* Circulation, 2008. **118**(18): p. 1864-1880.
187. Masjedi, S., et al., *Comparison of calcification potential of valvular interstitial cells isolated from individual aortic valve cusps.* Cardiovascular Pathology, 2016. **25**(3): p. 185-194.
188. Clark-Greuel, J.N., et al., *Transforming growth factor-β1 mechanisms in aortic valve calcification: increased alkaline phosphatase and related events.* The Annals of thoracic surgery, 2007. **83**(3): p. 946-953.
189. Ortolani, F., et al., *Pro-calcific responses by aortic valve interstitial cells in a novel in vitro model simulating dystrophic calcification.* Italian Journal of Anatomy and Embryology, 2010. **115**(1/2): p. 135-139.
190. Yip, C.Y.Y. and C.A. Simmons, *The aortic valve microenvironment and its role in calcific aortic valve disease.* Cardiovascular Pathology, 2011. **20**(3): p. 177-182.
191. Yang, X., et al., *Bone morphogenic protein 2 induces Runx2 and osteopontin expression in human aortic valve interstitial cells: role of Smad1 and extracellular signal-regulated kinase 1/2.* The Journal of thoracic and cardiovascular surgery, 2009. **138**(4): p. 1008-1015. e1.

192. Masjedi, S. and Z. Ferdous, *Understanding the role of sex in heart valve and major vascular diseases.* Cardiovascular engineering and technology, 2015. **6**(3): p. 209-219.
193. Aggarwal, S.R., et al., *Sex differences in aortic valve calcification measured by multidetector computed tomography in aortic stenosis.* Circulation: Cardiovascular Imaging, 2013. **6**(1): p. 40-47.
194. Baumgartner, H., et al., *Echocardiographic assessment of valve stenosis: EAE/ASE recommendations for clinical practice.* European Heart Journal-Cardiovascular Imaging, 2008.
195. Balachandran, K., et al., *Elevated cyclic stretch induces aortic valve calcification in a bone morphogenic protein-dependent manner.* Am J Pathol, 2010. **177**(1): p. 49-57.
196. Bertazzo, S., et al., *Nano-analytical electron microscopy reveals fundamental insights into human cardiovascular tissue calcification.* Nature Materials, 2013. **12**(6): p. 576-583.
197. Connolly, J.M., et al., *Triglycidylamine crosslinking of porcine aortic valve cusps or bovine pericardium results in improved biocompatibility, biomechanics, and calcification resistance: chemical and biological mechanisms.* Am J Pathol, 2005. **166**(1): p. 1-13.
198. Benton, J.A., H.B. Kern, and K.S. Anseth, *Substrate properties influence calcification in valvular interstitial cell culture.* J Heart Valve Dis, 2008. **17**(6): p. 689-99.
199. Rocha, R., et al., *Identification of calcifications in cardiac valves by near infrared Raman Spectroscopy.* Photomedicine and Laser Surgery, 2007. **25**(4): p. 287-290.
200. Dritsa, V., et al., *An Infrared Spectroscopic Study of Aortic Valve. A Possible Mechanism of Calcification and the Role of Magnesium Salts.* In Vivo, 2014. **28**(1): p. 91-98.
201. Vyavahare, N., et al., *Prevention of bioprosthetic heart valve calcification by ethanol preincubation. Efficacy and mechanisms.* Circulation, 1997. **95**(2): p. 479-88.
202. Bowler, M.A. and W.D. Merryman, *In vitro models of aortic valve calcification: solidifying a system.* Cardiovasc Pathol, 2015. **24**(1): p. 1-10.
203. Majd, A.E., et al., *Spatially Resolved Laser-Induced Breakdown Spectroscopy in Methane-Air Diffusion Flames.* Applied Spectroscopy, 2011. **65**(1): p. 36-42.
204. Gottfried, J.L., *Discrimination of biological and chemical threat simulants in residue mixtures on multiple substrates.* Analytical and Bioanalytical Chemistry, 2011. **400**(10): p. 3289-3301.
205. Davari, S.A., et al., *Back Cover: In-vitro analysis of early calcification in aortic valvular interstitial cells using Laser-Induced Breakdown Spectroscopy (LIBS) (J. Biophotonics 1/2018).* Journal of Biophotonics, 2018. **11**(1): p. e201870126.
206. Hybl, J.D., G.A. Lithgow, and S.G. Buckley, *Laser-induced breakdown spectroscopy detection and classification of biological aerosols.* Applied Spectroscopy, 2003. **57**(10): p. 1207-1215.
207. Kumar, A., et al., *Characterization of malignant tissue cells by laser-induced breakdown spectroscopy.* Applied Optics, 2004. **43**(28): p. 5399-5403.
208. Pedram, S.A., R.L. Klatzky, and P. Berkelman, *Torque Contribution to Haptic Rendering of Virtual Textures.* IEEE transactions on haptics, 2017. **10**(4): p. 567-579.
209. Mehari, F., et al., *Investigation of Laser Induced Breakdown Spectroscopy (LIBS) for the Differentiation of Nerve and Gland Tissue-A Possible Application for a Laser Surgery Feedback Control Mechanism.* Plasma Science & Technology, 2016. **18**(6): p. 654-660.
210. Samek, O., et al., *Quantitative laser-induced breakdown spectroscopy analysis of calcified tissue samples.* Spectrochimica Acta Part B-Atomic Spectroscopy, 2001. **56**(6): p. 865-875.
211. Singh, V.K., V. Kumar, and J. Sharma, *Importance of laser-induced breakdown spectroscopy for hard tissues (bone, teeth) and other calcified tissue materials.* Lasers in Medical Science, 2015. **30**(6): p. 1763-1778.
212. Masjedi, S., et al., *Sex-related differences in matrix remodeling and early osteogenic markers in aortic valvular interstitial cells.* Heart Vessels, 2017. **32**(2): p. 217-228.
213. Seya, K., et al., *Contribution of Bone Morphogenetic Protein-2 to Aortic Valve Calcification in Aged Rat.* Journal of Pharmacological Sciences, 2011. **115**(1): p. 8-14.

214. Holtorf, H.L., J.A. Jansen, and A.G. Mikos, *Flow perfusion culture induces the osteoblastic differentiation of marrow stroma cell-scaffold constructs in the absence of dexamethasone.* J Biomed Mater Res A, 2005. **72**(3): p. 326-34.
215. Byon, C.H., et al., *Oxidative stress induces vascular calcification through modulation of the osteogenic transcription factor Runx2 by AKT signaling.* Journal of Biological Chemistry, 2008. **283**(22): p. 15319-15327.
216. Kolambkar, Y.M., et al., *Colonization and osteogenic differentiation of different stem cell sources on electrospun nanofiber meshes.* Tissue Eng Part A, 2010. **16**(10): p. 3219-30.

Appendices

Appendix A Extended investigations using LIBS: Semiconductor and thin film applications

This chapter is based on the following publications:

- **Davari, S. A.**; Hu, S.; Pamu, R.; Mukherjee, D. "Calibration-free quantitative analysis of thin-film oxide layers in semiconductors using Laser Induced Breakdown Spectroscopy (LIBS)", Journal of Analytical Atomic Spectrometry, 2017,32, 1378-1387.

- **Davari, S.A.**, Standley, R.W., Taylor, P., Mukherjee, D.,''Detection of interstitial oxygen contents in CZ grown silicon crystals using matrix-assisted calibration in laser-induced breakdown spectroscopy (LIBS) '', Analytical Chemistry, Under review

- **Davari, S. A.**; Mukherjee, D. "Analyzing depth profile in heterojunction systems using Laser InducedBreakdown Spectroscopy (LIBS)", MRS Communications, ***[Invited Paper]***, in prep

A.1 Introduction

The global energy demands in recent decades have led to significant manufacturing of semiconducting materials for solar cell applications. The efficiency and performance of solar cells strongly depend on the quality and characteristic properties of cost-effective semiconducting materials. The estimated global market share of US in the semiconductor sales is approximated at~ 50% with the most well-known materials of interest being Silicon (Si), and heterojunction materials such as Gallium arsenide (GaAs) and copper indium gallium diselenide (CIGS) [150]. Specifically, for multi-junction solar cells, the primary parameter that affects the efficiency of thin film semiconductors such as CIGS [$CuIn_{1-x}Ga_xSe_2$] is the chemical composition of the absorber layer that determines the charge density and transport properties [151-153]. Variations in stoichiometric ratios of the main constituents change both the structural and electronic properties of these materials [151-153]. Typically, in the photovoltaic grade, Si impurities such as boron and oxygen change the electrical and mechanical properties significantly [154, 155]. While oxygen contents determine the defects that decrease the hardness of the Si wafers, it is essential for internal

gettering [156, 157]. On the other hand, the efficiency of metal-oxide-semiconductors field-effect transistors (MOSFET) is largely driven by the property and reliability of the SiO_2 layer [158-160] wherein the main gate current leakage gets affected by the SiO_2 thickness [161].

To this end, various techniques such as secondary ion mass spectrometry (SIMS) [162], x-ray fluorescence (XRF) [163], inductively coupled plasma optical emission spectroscopy (ICP-OES) [164] have been used for the elemental analysis of thin-film semiconductor materials. Both SIMS and ICP-OES require extensive sample preparations and standards with ICP-OES specifically requiring the use of strong and harmful acids such as hydrofluoric acid. Such requirements render them as destructive methods [165] that cannot be employed for in-situ characterizations during most industrial manufacturing processes. But these methods are largely relied upon for post-processing off-line quality control in the industrial semiconductor sectors due to their ability to provide accurate measurements. On the other hand, only XRF can be operated in atmospheric conditions with minimal sample preparations [166]. However, XRF is not accurate for light elements measurements [167]. To this end, Fourier transform infrared (FTIR) spectrometry is commonly adopted as the industrial standard technique for oxygen concentration measurements in single crystalline Si wafers [168, 169]. However, it suffers from interference from free carrier absorption present in heavily doped substrates [170]. To overcome such issues, the semiconductor industry currently resorts to gas fusion analysis (GFA) to measure oxygen concentrations in heavily doped epitaxial substrate. But, GFA is a high destructive technique that has increasingly proven to be energy expensive and time consuming for the semiconductor manufacturing sector. In turn, such techniques fail to get implemented as rapid and on-line quantitative analyses tool for quality control purposes. Specifically, for MOS devices, the challenge rests on the accurate monitoring and tailoring of thin oxide layers on silicon or other semiconducting materials to tune

the inversion layer charge accumulation, mobility and transport [171, 172]. Typical commercial-grade MOSFETS have been classically fabricated and extensively analyzed for gate oxide layers ranging between ~3 nm and 20-50 nm thicknesses approximately [171]. To this end, the effect of gate oxide layer thicknesses on the charge mobility and capacitance in Si/SiO_2 systems become a critical parameter in the design of MOSFETS and have been investigated in great details over the years [173]. In light of the aforementioned challenges in the physical and chemical characterizations of thin films for semiconductor manufacturing sectors, there exits an acute need for a robust and efficient analytical technique that can accurately monitor and measure gate oxide film characteristics during the manufacturing and processing of metal/metal oxide semiconductor materials in order to tailor their wafer electronic properties for specific device fabrication requirements.

Laser Induced Breakdown Spectroscopy (LIBS) is a relatively non-destructive spectrochemical characterization technique that can address the aforementioned issues in a facile, rapid and yet effective manner. Being a non-contact technique that is not limited by the type or physical state of the analyte materials, LIBS provides advantages that are specifically attractive for large-scale manufacturing sectors. Furthermore, it is cost-effective and capable of carrying out rapid multi elemental analysis in one shot without compromising on the precision that makes it well-suited for in-situ implementation in industrial environments. In the past, LIBS has been employed for chemical analysis in highly diverse applications ranging from combustion [174], environmental/bio-hazard analysis [175], and intermetallic nanocatalysts [121-123] to, explosives detection/energetic studies [176], pharmaceutical [131], and biological/biomedical studies [132].

In recent years, there has been a growing interest in employing LIBS for material characterizations in the semiconductor industry – specifically, in regards to its choice as the future on-line

quantitative analysis tool. To this end, Owens et al. [177] showed that LIBS can effectively measure heavy metal dopants in thin films. Lee et al. [178] had carried out semi-quantitative LIBS analysis to obtain the elemental ratios of constituents in thin-film CIGS absorption layer. Added to this, Darwiche et al. [165] had extended the technique to quantify the extent of boron dopants in solar grade Si wafers using standard calibration curves. More recent efforts by Axente et al. [179] and Popescu et al. [180] have demonstrated the application of LIBS for the characterization of indium zinc oxide thin films, while Banerjee et al. [181] had employed the technique for multi-layered profiling of organic photovoltaic coatings. Specifically, the work by Axente et al. [179] had compared recorded spectra with spectra computed based on local thermodynamics equilibrium to obtain atomic fraction of indium quantitatively. On the other hand, the work by Banerjee et al. had qualitatively shown that LIBS can be employed as a feedback control system during real-time laser scribing processes. It needs to be mentioned here that the calibration-free LIBS techniques proposed by Popescu et al. [180] and Axente et al. [179] resorted to computational models in deducing the quantitative elemental fractions, as compared to a methodology based on raw spectral data collected from analyte samples as developed by our previous works and implemented in the current study. Additionally, while the average thin films used in these studies were about 350 nm (Popescu et al. [180]) and 500 nm (Axente et al. [179]) thick, they did not attempt to report the lowest film thickness analytically detectable by LIBS.

In our efforts to investigate the feasibility of LIBS as the future analytical tool for rapid quantitative characterization of industrial grade thin film MOS, this study presents a calibration-free LIBS technique for quantifying thin-film oxide layers grown atop industrial-grade Si wafers. Commercial Si wafers, obtained were treated at different temperatures in order to synthesize and control the oxide layer thicknesses systematically. The ratio of ablated oxygen (O) to Si is

measured based on the O and Si atomic emission signals by using the LIBS internal calibration technique developed in our earlier works [121, 130]. The oxide layer thicknesses along with the crater sizes and profiles are measured using ellipsometry, scanning electron microscope (SEM), atomic force microscopy (AFM), and optical profilometer. Based on the profilometric measurements, the ratios of O to Si in the oxide layers and their film thicknesses on the Si wafers are estimated, and compared to the LIBS results.

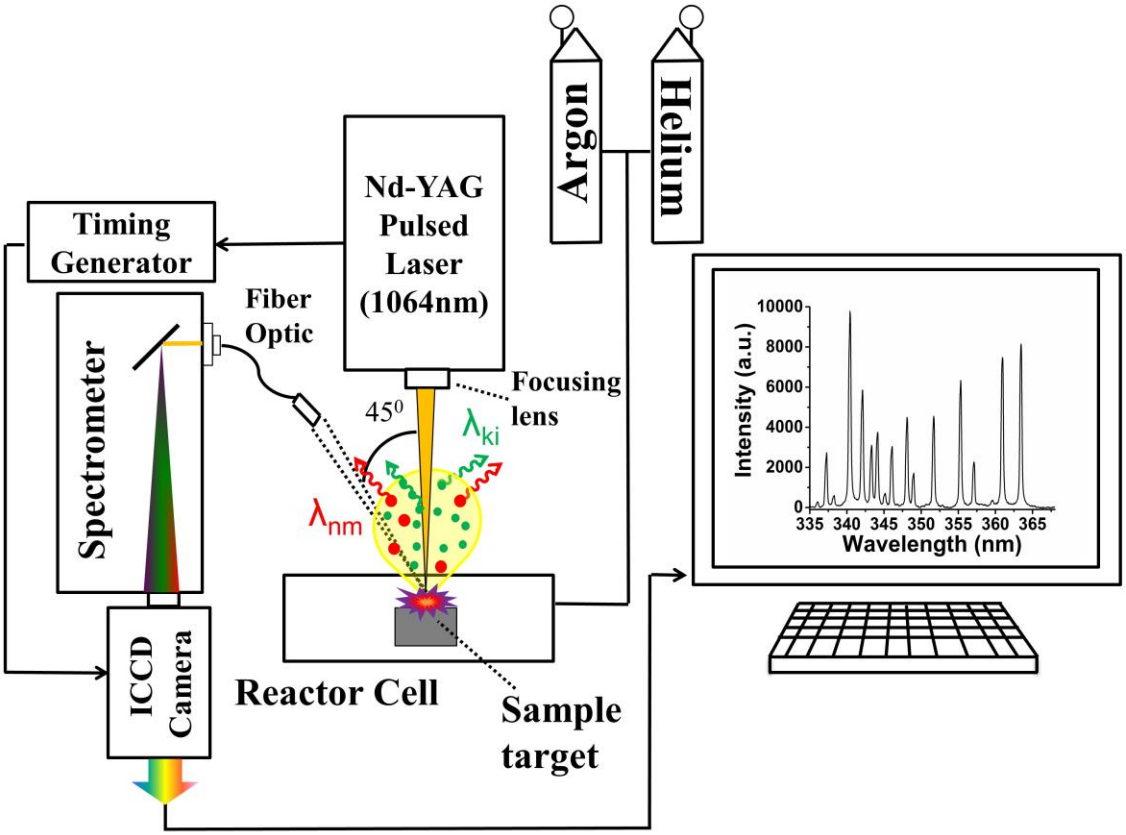

Figure A.1: Schematic of LIBS set-up used in this study.

A.2 Experimental set-up

A.2.1 LIBS set-up

The experimental set-up is illustrated in Figure A.1. The laser-induced plasma is generated on the sample target surface using a Q-switched Nd-YAG laser of wavelength 1064 nm operating at 10

Hz repetition rates, 200 mJ/pulse energy, and a pulse width of 8 ns (Make: Insight 122551-R). The laser is focused with a 25 mm diameter fused silica lens (focal length = 35mm) at the focal point on the target surface (Figure A.1). The spot size on the sample is set to 75 µm diameter, which creates a plasma volume of ~1-2 mm^3 approximately. Since the oxide layer is thin, only one laser shot per spot is collected. To improve the statistical average of the signal intensity for each analyte of interest, spectral data over approximately 100–150 spots are collected. The plasma emission is collected with a fiber optic port carrying a pair of collimation-focusing lens and mounted at 45 degree collection angle (Figure A.1), which yields the optimum intensity from the plasma volume. The focused light is transmitted to a Czerny-Turner spectrometer (Make: Andor Technology; Model: Shamrock - SR-303i-A) with 1200 grooves/mm grating (resolution of 0.1 nm at 500 nm) and a nominal dispersion of 2.58 nm/mm. The slit width is fixed at 95µm for all experiments carried out here in order to have the optimum spectral line intensity and resolution. A time-gated intensified charge-coupled device (ICCD) detector array (1024x1024 CCD) (Make: Andor Technology; Model: DH334T-18U-E3) detects the spectral lines at the spectrometer exit focal plane. The time gating is synchronized with the laser Q-switch through an in-built timing generator in the ICCD camera set-up.

A.2.2 SiO_2 films synthesis

Commercial silicon wafers, purchased from (UniversityWafer, Inc. ID#2444), were cut to approximately 1x1 cm^2 pieces. The wafers underwent dry thermal oxidation in laboratory furnaces at various temperatures in order to create and control the oxide layer thickness on top of the wafer. Specifically, the wafers were baked for 20 minutes at oven temperatures ranging from 900^0 C-1000^0 C with a 25^0 C step, and with one final sample being baked at 1050^0 C. The samples were tested using LIBS in an in-house built reactor cell while both helium (6 lpm) and argon (2 lpm)

were purged into the cell as the buffer gas. The choice of flow rates is discussed in the results and discussion. To account for any unwanted background trace oxygen that might exist in the buffer gas or the control Si wafer samples, the background emission for O I is subtracted from the emissions from the baked Si wafer samples. Here, the background is considered as the emissions from the Si wafers without any oxide layer. To accomplish that, Si wafers are dipped into 10% hydrofluoric (HF) acid for 10 minutes.

A.2.3 Crater characterization

Prior to sample ablations for the LIBS measurements, the oxide layer thicknesses on the respective heat-treated Si wafer samples are measured using an ellipsometer (Horiba Sci.; Model: UVISEL,). Subsequent to the LIBS measurements, the sample crater sizes are also measured using a profilometer (Veeco Wyko Non-contact Profilometer NT3300). Finally, we use atomic-force microscopy (AFM; Make: NT-MDT; Model: NTEGRA Spectra) in the tapping mode with silicon cantilever tips (Model: AppNano Model: ACTA) and scanning electron microscopy (SEM) in order to verify the crater sizes and profiles further.

A.3 Results and discussion

In this study, atomic transition lines were chosen from the NIST Atomic Energy Levels Data Center [146]. For detailed quantitative LIBS analyses, the atomic emission lines of O I (777.19 nm) and Si I (288.16 nm) were selected. The specific choice of these lines was based on their robust transition probabilities and line strengths. To this end, Table A.1 reports the detailed spectral data for the aforementioned emission lines of choice. Figure A.2. a & b show spectral emissions

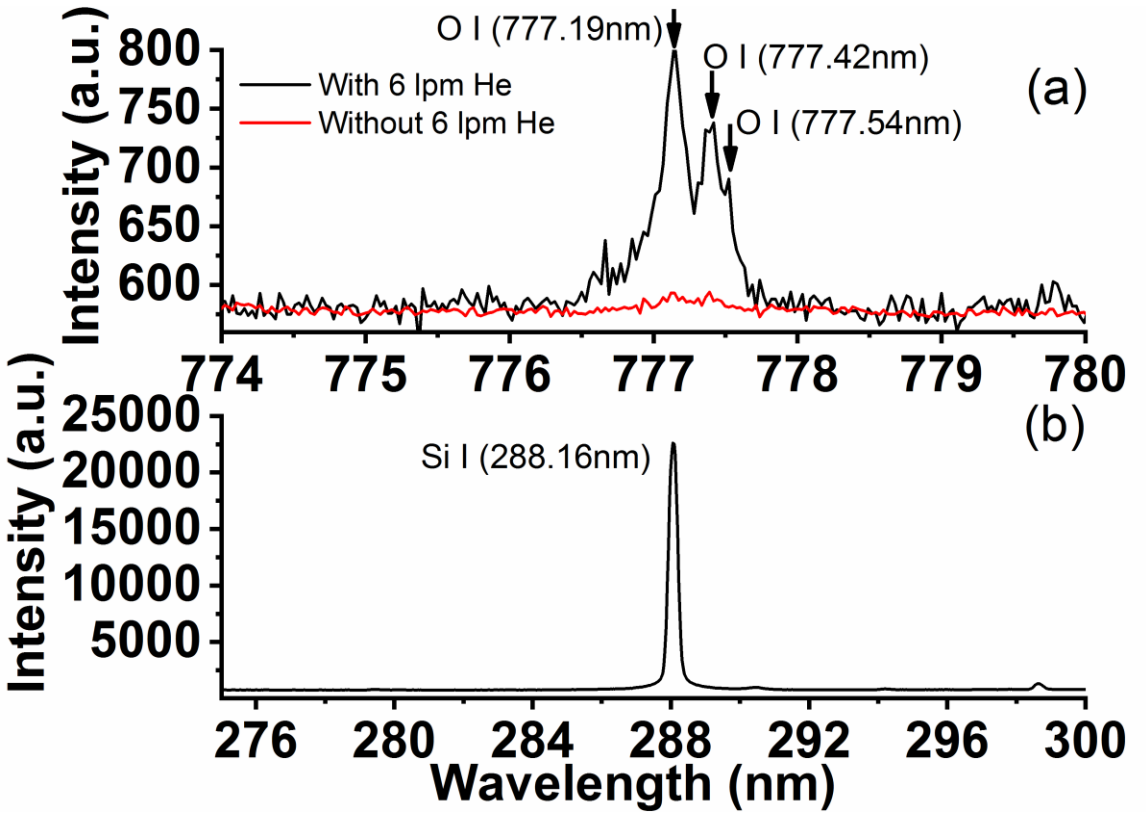

Figure A.2: Spectral emission signature for (a) O I (777.19 nm) with and without helium in the buffer gas, and (b) Si I (288.16 nm) lines at the respective gate delays of 3.5µs, and 5µs.

Table A-1. Atomic spectral database [142] for Si I and O I emission lines used for the population density calculations during quantitative analysis of ablated spots.

Species	Wavelength, λ_{ki} (nm)	Transition probability, A_{ki} (10^6 1/s)	Upper energy level, E_k (eV)	Lower energy level, E_i (eV)	g_k	g_i
Si I	288.16	218	5.082	0.781	3	5
O I	777.19	36.9	10.741	9.146	7	5

of O I (777.19 nm) and Si I (288.16 nm) lines respectively. It is observed in Figure A.2a that in the presence of 6 lpm helium mixed with 2 lpm argon, O I (777.19 nm) signal enhances significantly. Such observations were also previously reported by Mukherjee et al.'s work [120] where it was discussed that the addition of helium creates a less dense plasma that effectively reduces the background continuum noise. However, reducing plasma density eventually deteriorates the emission signals too. Therefore, based on the specific sample of study, an optimal value for the ratio of helium to argon flow rates provides the ideal signal enhancements. To this end, the O I (777.19 nm) SNR is plotted as a function of He/Ar flow rates ratio as the background buffer gas (Figure A.3). It is clearly observed that an optimal ratio of ~ 3 for He/Ar ratio in the background buffer gas produces the maximum O I SNR of ~18.

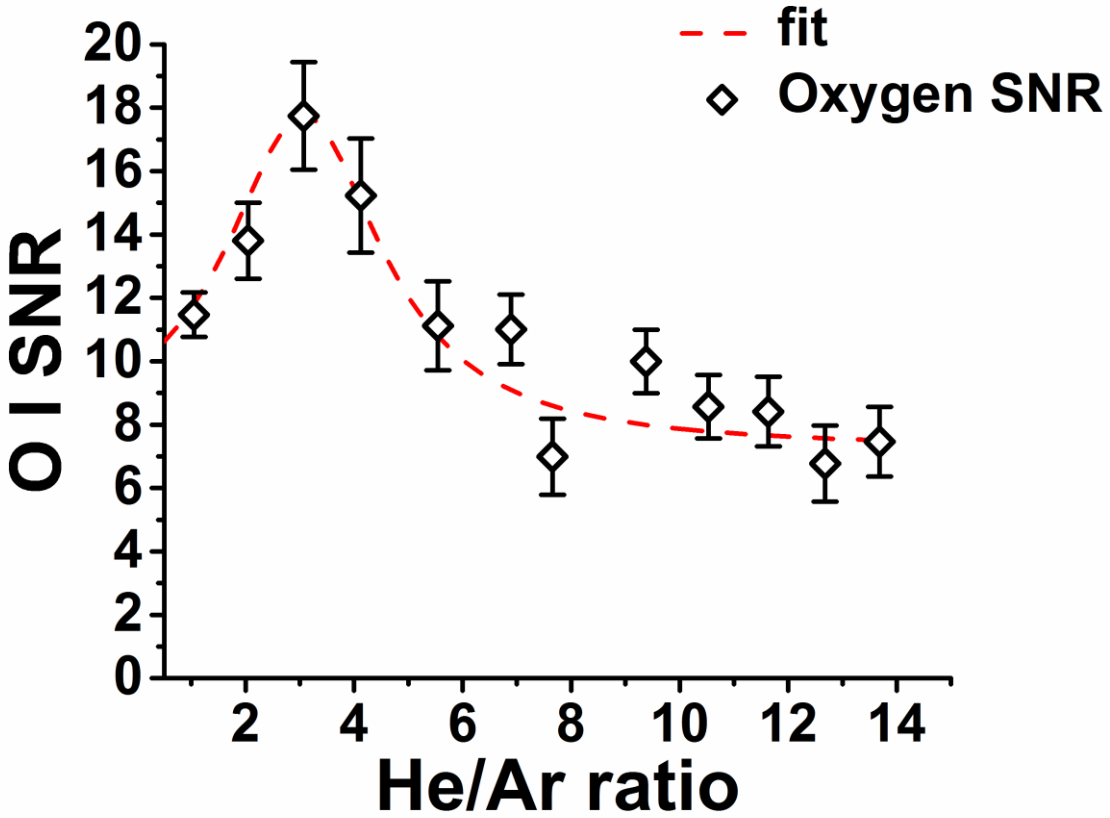

Figure A.3: Optimizing oxygen SNR with respect to ratio of helium to argon flow rates.

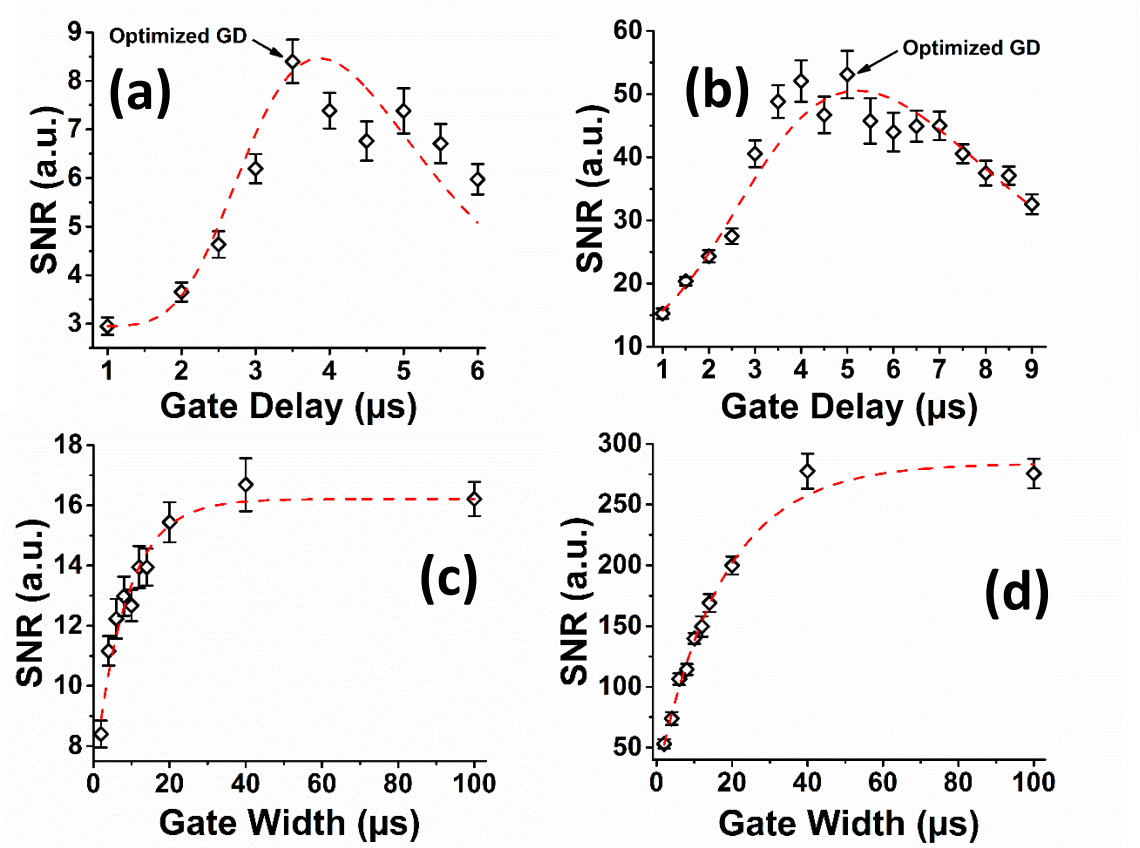

Figure A.4: Temporal evolution of signal-to-noise ratio for (a) O I (777.19 nm), and (b) Si I (288.16 nm) over gate delays. The optimal gate delays were determined to be 3.5μs and 5μs for the peak signal-to-noise ratio for O I (777.19 nm), and (b) Si I (288.16 nm) respectively. (c) temporal evolution of signal-to-noise ratio for (c) O I (777.19 nm), and (d) Si I (288.16 nm) over gate width.

For lower ratios, the plasma is relatively thick that subdues the signal enhancement while for greater ratios, the plasma becomes too thin and O I (777.19 nm) emission signal is decreased. Hence, for the rest of experiments, 2 lpm of argon and 6 lpm of helium was used as the buffer gas. Furthermore, in order to gain the maximum accuracy for the population density calculations from the LIBS signals, the optimal gate delays for each of the Si I and O I emission lines are determined by plotting their respective SNRs as a function gate delays. Figure A.4.a & b shows the temporal

evolution of O I (777.19 nm) and Si I (288.16 nm) emission lines respectively at the gate widths of 2 µs. From these plots, the optimal gate delays are estimated as 3.5µs and 5µs for the respective O I and Si I emission lines. Based on the linear parts of Figure A.4c and 4d the gate width 14µs is used for both O I and Si I. Figure A.5 shows the characteristic emission spectra of O I (777.19 nm) acquired from the control (devoid of oxide layer) and specific samples baked at different temperatures. It can be observed from Figure A.5 that the control sample still shows some background emission at 777.19 nm, which is associated with the ubiquitous oxygen contents in the reactor cell that is almost impossible to eliminate in the absence of extremely high-end vacuum systems.

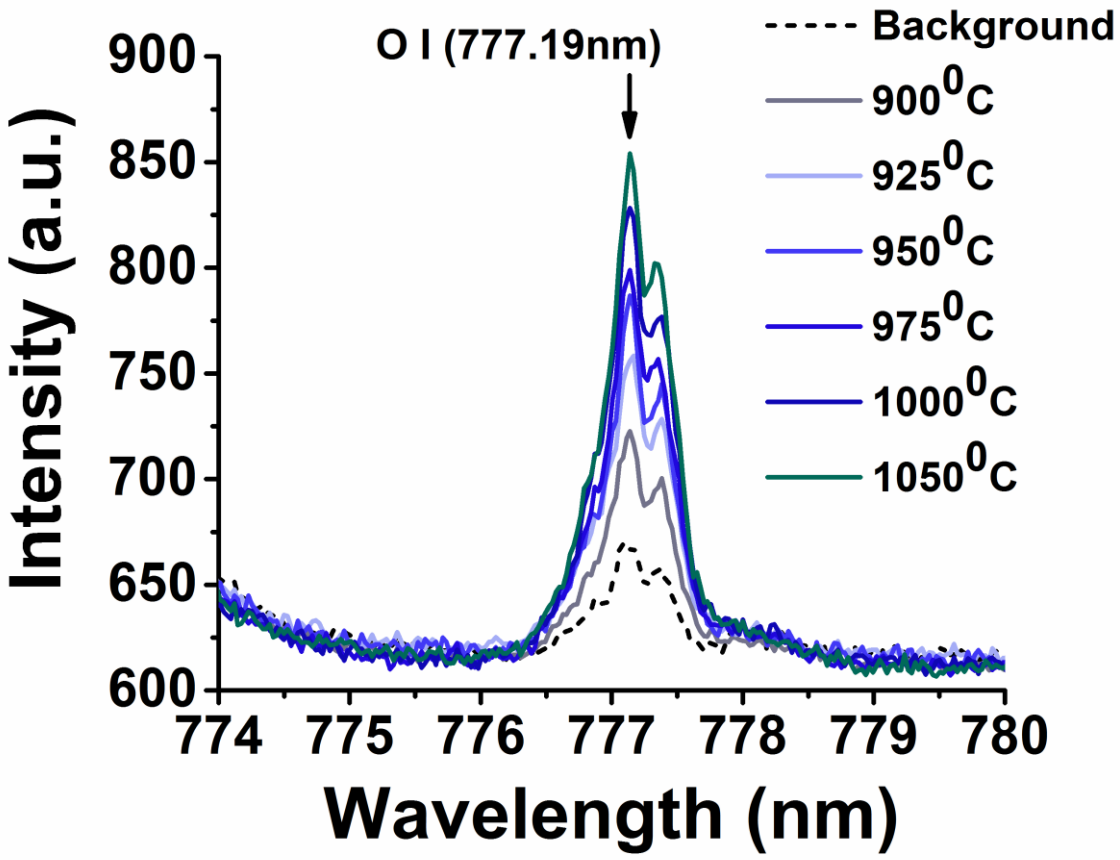

Figure A.5: Spectral emission signature for O I (777.19 nm) for samples with various oxide layer thickness.

However, the specific heated samples show distinct enhancement of the emissions at O I (777.19 nm) as compared to the background emission which allows for background subtractions. Moreover, the O I (777.19 nm) emissions increase systematically as the oxide layers of the specific samples increase due to their baking at increasing temperatures. This increasing oxide layer thickness is also confirmed by ellipsometry measurements in the next section. The plasma excitation temperatures, T_{exc} required for the population density calculations are estimated from linear Boltzmann plots as explained in the experimental sections earlier. Here, the linear Boltzmann plots are constructed at the two different time delays (3.5μs and 5μs) of the plasma evolution using a series of Ar I lines with known spectral properties as listed in Table A.2.

Table A-2. Atomic spectral database [142] for different Ar atomic emission lines.

Sample treated temperature	[O]/[Si] (Ablation-Cylinder)	[O]/[Si] (LIBS)	[O]/[Si] (Ablation-Cone frustum)	Plasma excitation temp. T_{exc} (K)	
				at 3.5μs	at 5μs
900^0 C	0.022	0.025	0.046	17,125±3833	15,166±2893
925^0 C	0.027	0.047	0.047	17,803±3706	15,849±3235
950^0 C	0.032	0.045	0.079	17,372±2898	16,427±3637
975^0 C	0.051	0.052	0.102	20,802±4162	17,580±4550
1000^0 C	0.057	0.098	0.133	21,535±4692	20,311±5826
1050^0 C	0.078	0.097	0.179	20,142±4620	18,255±4628

Figure A.6a and 6b illustrate the Boltzmann plots acquired at 3.5μs and 5μs gate, whose slopes indicate T_{exc}=17,126 K and 15,166 K respectively. Similarly, the T_{exc} values for all the different heat–treated samples are estimated and reported in Table A.3. The estimated excitation temperatures are employed to calculate the relative population densities of oxygen (NiO I), silicon (NiSi I) and argon (NiAr I) from the respective atomic emission lines of O I (777.19 nm), Si I (288.16 nm) and Ar I (series of lines indicated in Table A.2). Using Ar as the bulk species in the plasma for the normalization shown in eqn. 4.2, the ratio of oxygen to silicon ([O]/[Si]) is:

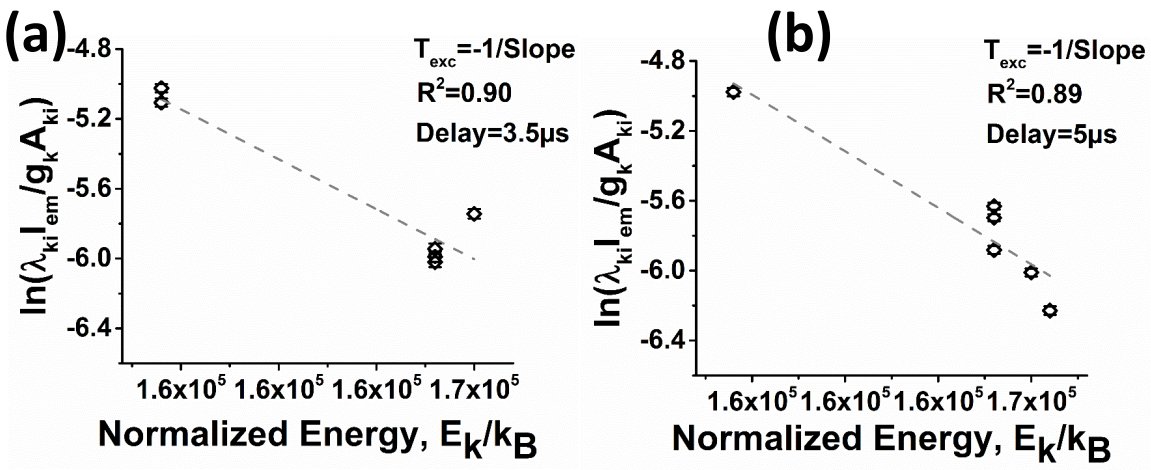

Figure A.6: The linear Boltzmann plots generated from Ar I lines listed in Table A.2, and used for T_{exc} calculations at the respective gate delays of 3.5μs and 5μs.

Table A-3. [O]/[Si] ratios for various samples and respective plasma excitation temperatures.

Species	Wavelength, λ_{ki} (nm)	Transition probability, A_{ki} (10^6 1/s)	Upper energy level, E_k (eV)	Lower energy level, E_i (eV)	g_k	g_i
Ar I	415.859	1.40	14.528	11.548	5	5
Ar I	420.068	0.967	14.499	11.548	7	5
Ar I	425.936	3.98	14.738	11.828	1	3
Ar I	427.217	0.797	14.525	11.624	3	3
Ar I	433.356	0.568	14.688	11.828	5	3
Ar I	696.543	6.39	13.328	11.548	3	5
Ar I	706.722	3.80	13.302	11.548	5	5

$$R = \frac{[O]}{[Si]} = \frac{\left[N_i^{O\ I\ (777.19\ nm)} \Big/ N_i^{Ar\ I} \right]_{@GD=3.5\mu s}}{\left[N_i^{Si\ I\ (288.16\ nm)} \Big/ N_i^{Ar\ I} \right]_{@GD=5\mu s}} \qquad (A.1)$$

The results for [O]/[Si] (LIBS) ratios are tabulated in Table A.3. In order to compare the results obtained from the quantitative LIBS analyses, the amounts of ablated materials are also estimated by characterizing the oxide layer thicknesses and crater profile using ellipsometry, SEM, AFM and profilometer measurements. Based on the profilometric calculation, discussed in the following sections, the amount of ablated oxygen and silicon are estimated, and used for calculating [O]/[Si] (ablation) ratios in Table A.3 from the crater ablation analyses that will be presented in the following sections. As the first step toward characterization of the amount of elemental species in the laser ablated crater from the LIBS measurements, the initial oxide layer thicknesses from the samples are measured using ellipsometry. A classical dispersion model based on SiO_2 on top of silicon substrate is used for curve fitting. For each oxidation temperature, four different pieces and on each piece four different spots are analyzed for the ellipsometry measurements. The oxide layer thicknesses are reported in Table A.4. As expected, the oxide layer thickness grows further as the oxidation temperature increases. Moreover, the small standard deviations indicate that the oxide layer is uniform across the samples surface.

Table A-4. The oxide layer thicknesses for various oxidation temperature.

Sample treated temperature	900^0 C	925^0 C	950^0 C	975^0 C	1000^0 C	1050^0 C
Thickness (nm)	50.94±0.25	64.63±0.19	75.62±0.05	122.10±0.01	136.93±0.35	188.82±0.37

Figure A.7 shows the SEM image for the crater obtained from the ablation of a representative sample (Si wafer baked at 950^0 C). The image indicates that ablation spot diameter is approximately 200μm, while the crater depth can be qualitatively observed to be shallow.

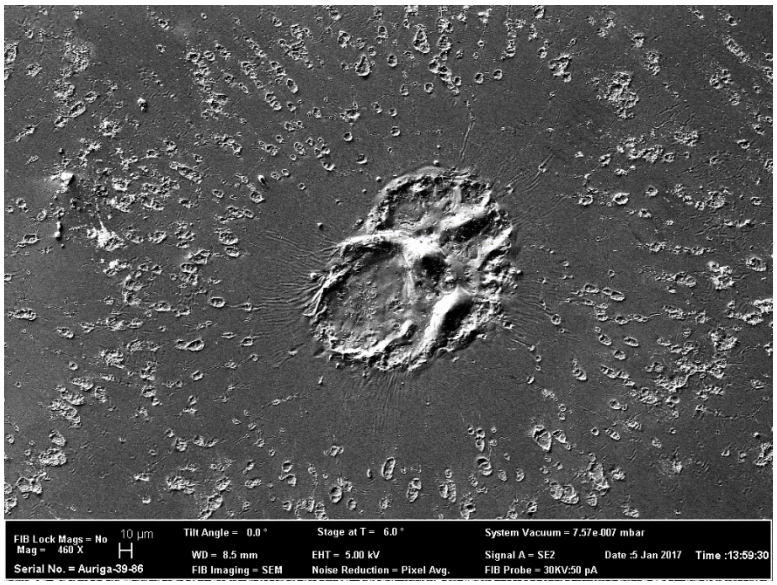

Figure A.7: SEM image of the ablated spots used for measuring ablated spot diameter.

In order to obtain the crater depth quantitatively, the samples are measured using a profilometer (Figure A.8a). The profilometer result also indicates that the ablation spot diameter is 200µm, while the crater depth is approximated to be ~2.5µm. For a secondary verification of the crater depth, the ablation spots are also topographically imaged using AFM in tapping mode with slow scan rate.

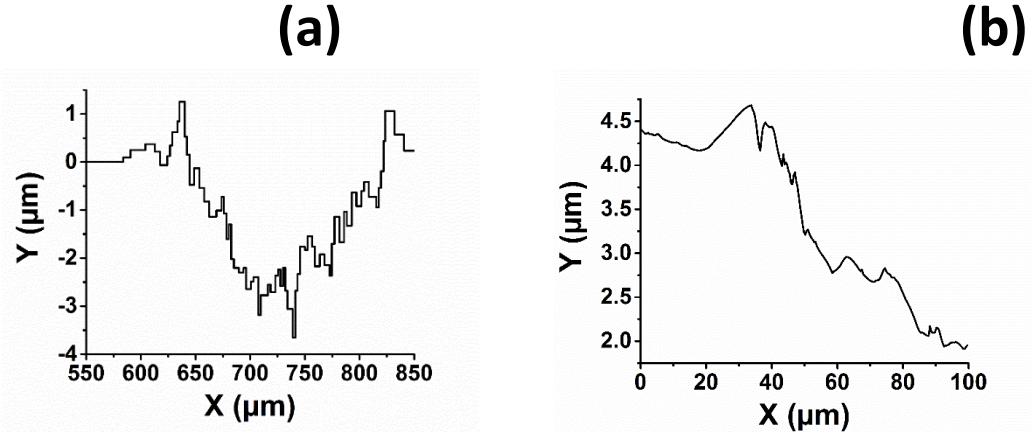

Figure A.8: Depth profile measurement for the ablated spots using (a) optical profilometer, and (b) AFM.

Due to the AFM instrument limitations, only a 100µmx100µm window can be measured. Hence, the measured window was chosen such that it spanned over ~30µm of the spot edge and ~70µm of the crater. As seen from the z-profile of the AFM topography image for the selected window in Figure A.8.b, the crater depth can be confirmed to be ~ 2.5 as also corroborated from our profilometer measurements. Based on the oxide layer thickness, ablation spot diameter and the crater depth, two simple geometric models, namely cylindrical and the frustum of a cone, are constructed to calculate the amount of ablated O and Si, and construct the ablated [O]/[Si] ratio as depicted in Figure A.9.a & b. Based on these geometries for the ablated volume, [O]/[Si] ratio can be determined as:

$$\frac{[O]}{[Si]} = \frac{2(\frac{\rho_{SiO_2}}{Mw_{SiO_2}})\delta_{SiO_2}}{(\frac{\rho_{SiO_2}}{Mw_{SiO_2}})\delta_{SiO_2} + (\frac{\rho_{Si}}{Mw_{Si}})h} \qquad \text{(A.2)}$$

where V_{SiO2} and V_{Si} are the ablated volumes of oxide layer and silicon substrate respectively.

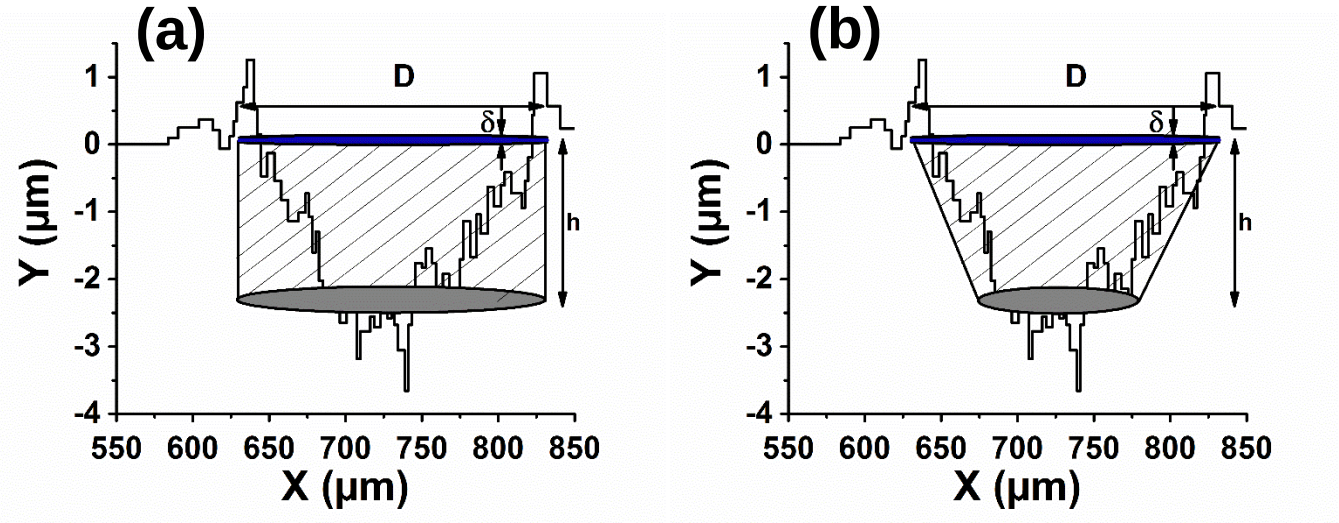

Figure A.9: The simple geometric models (a) cylinder and (b) cone-frustum showing ablation volume used for calculating [O]/[Si] ratio.

They can be expressed by the oxide layer thickness (δ_{SiO2}), and crater depth (h). Mw and ρ are molecular weights and densities respectively and are tabulated in Table A.5 for Si and SiO_2.

Table A-5. Si and SiO2 properties used for calculating [O]/[Si] ratio from profilometric model.

Properties	Molecular weight, Mw (g/mol)	Density, ρ (g/cm^3)
SiO_2	60.083	2.65
Si	28.085	2.33

Figure A.10 illustrates the results for the ratio of [O]/[Si] as obtained from LIBS plotted as a function of the respective ratios obtained from crater profile or ablation characterizations based on the assumption of a cylindrical and cone frustum geometries. The red and the blue dotted lines represent the linear fits to the calculated values for the cylindrical and the cone-frustum geometries.

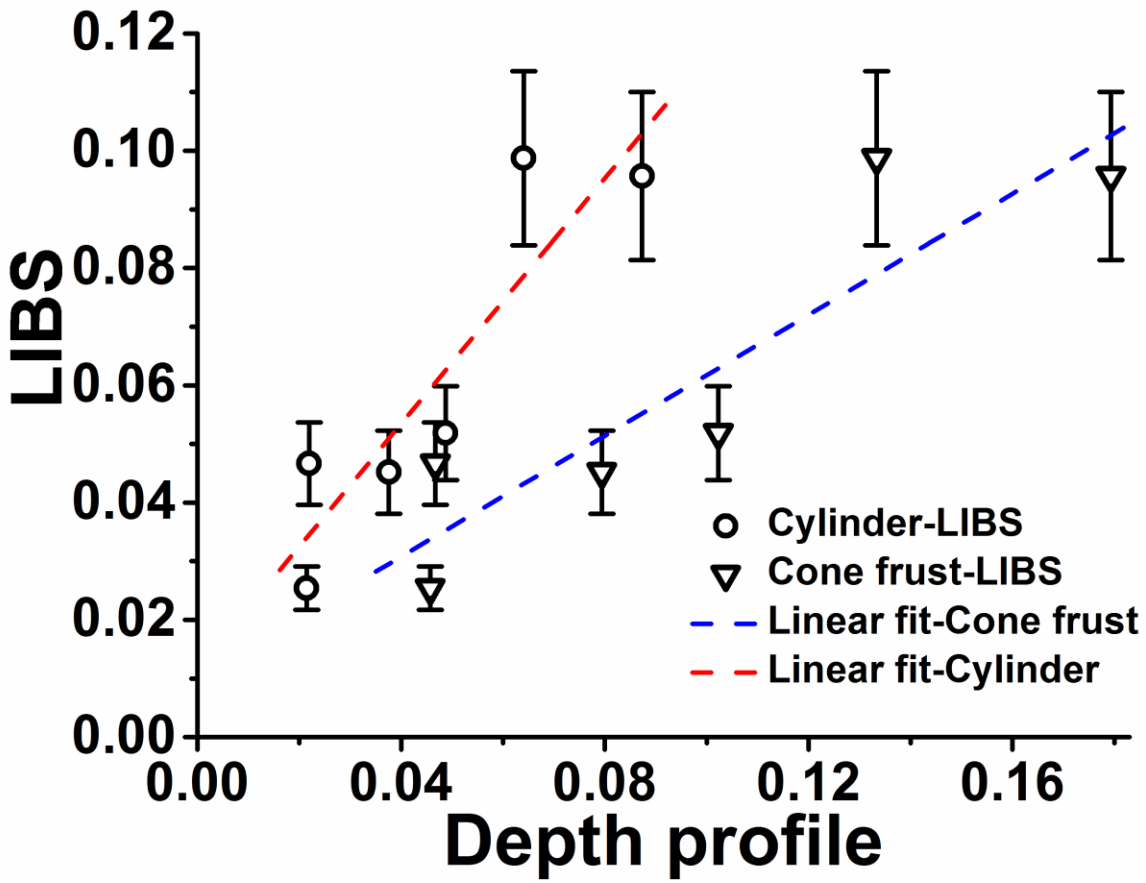

Figure A.10: Comparison between [O]/[Si] ratio directly measured by LIBS, and calculated by characterizing ablated spot.

It can be observed that the LIBS results are relatively in good agreements and indicate a linear correlation with the profilometric calculations. The error bars are calculated based on the error propagation for both methods due to uncertainties in plasma temperature, shot-to-shot variation in laser-induced, and standard deviations in crater measurements. The deviations from the profilometric calculations can be related to the errors in measuring crater profiles and simplistic geometric models, which change the amount of ablated silicon. Analyzing the crater profile of the ablation spot indicates that the amount of ablated silicon based on the cylinder geometry is greater than the actual ablated silicon, while the cone-frustum underestimates the amount of ablated silicon. In fact, the ideal one-to-one linear correlation between the [O]/[Si] ratios from LIBS measurements and the profilometric analyses appears to lie within the two sets of data for the cylindrical and the cone-frustum profile geometry cases (i.e. the red and the blue dotted linear fits). Furthermore, the errors bars on the [O]/[Si] ratios from the LIBS measurements commensurate with the spread in the data for the aforementioned two cases thereby indicating that the deviations are within the experimental margins of error. Finally we present the LIBS calibration for the quantitative determination of thin-film oxide layer thickness on Si wafer by plotting the O I subtracted signal as a function of oxide layer thicknesses (from ellipsometry measurements) in Figure A.11. Based on the slope of the calibration curve, the minimum distinguishable oxide layer (δmin) that can be estimated form our current LIBS set-up is found to be:

$$\delta_{min} = \frac{3\sigma_B}{S} \tag{A.3}$$

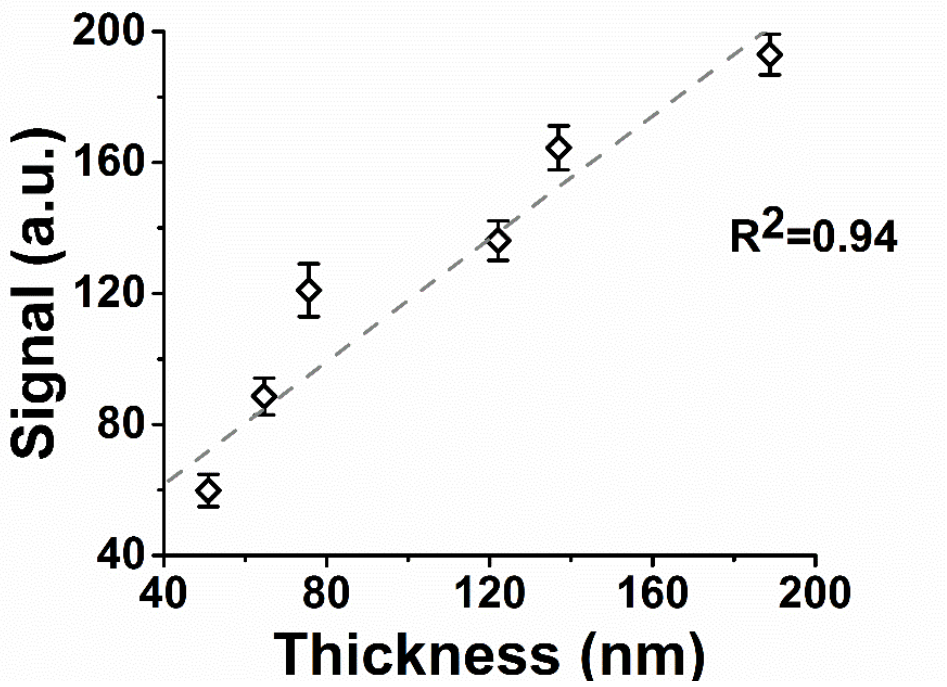

Figure A.11: Calibration curve for O I (777.19 nm) SNR as a function of oxide layer thickness.

where, is the standard deviation of the background and S is the slope of the calibration curve. This give the estimated thinnest detectable oxide layer using LIBS as δmin ~ 10.51 ± 1.44 nm.

A.4 Conclusion

We have employed LIBS for calibration-free quantitative analysis of thin-film silicon dioxide layers with various thicknesses synthesized via dry thermal oxidation of Si wafers. To this end, an internal calibration technique was applied that involved effective normalization of the analyte species densities by bulk species densities in the laser-induced plasma. The species densities of O (analyte) and Si (bulk) for the SiO_2 films in this case were estimated from the respective atomic emission lines at identical plasma conditions to generate the ablated oxygen to silicon ([O]/[Si]) ratio. The results from our LIBS analyses were corroborated by the [O]/[Si] ratios directly calculated from the ablated spots by measuring the oxide layer thicknesses and crater profiles using ellipsometry, SEM, AFM and profilometry techniques. The results are in good agreement with each other within the margins of experimental uncertainty. The small deviations of the LIBS results

from the profilometric calculations were attributed to the errors in the depth measurements and assumed geometry of the crater profile. Based on our measurements, a calibration curve for the LIBS analysis was established that indicated the detection limit for the thinnest oxide layer thickness to be ~ 10.5 ± 1.4 nm. Results from the current work provide future directions towards the promising potential of LIBS as an analytical tool for rapid screening of oxide layers in MOS transistors/capacitors, and more generally, for surface composition analysis of thin-film materials.

Appendix B Extended investigations using LIBS: Biomedical engineering

This chapter is based on the following publications:

- **Davari, S. A.**; Masjedi, S.; Ferdous, Z.; Mukherjee, D. "In-vitro early detection of calcium in aortic valvular interstitial cells undergoing osteogenic differentiation using Laser-Induced Breakdown Spectroscopy (LIBS)", Journal of Biophotonics, 2018, 11 (1) ***[Cover Article]***.

B.1 Introduction

Calcific aortic valve disease (CAVD) is a common cardiovascular disorder affecting 25% of the elderly population over the age of 65 and at severe stages, 4% over the age of 80 [182, 183]. Early detection of CAVD is elusive and late detection of CAVD leaves the patients with the only viable treatment of aortic valve transplant surgery [184, 185]. Early stage CAVD is associated with calcium (Ca) accumulation in aortic valves that can lead to stenotic aortic valves wherein extracellular matrix (ECM) decomposition and tissue stiffening occurs along with large nodule formation within the aortic valve cusps [186]. CAVD is an active cell-mediated condition, where the inhabitant valvular interstitial cells (VICs) differentiate into osteoblast-like cells and exhibit bone-like characteristics, such as calcific nodule formation [187, 188], hydroxyapatite deposition [183, 189] and osteogenic marker expressions [190, 191].

Typically computer tomography (CT) and echocardiography are used as the dominant tools for clinical diagnosis of CAVD in patients [192-194]. For direct evaluation of aortic valve calcification for research purposes, various techniques have been developed to measure the calcium deposition in VICs or valve tissue sections on a laboratory platform. The most common techniques include Von Kossa staining [187, 195], Alizarin Red staining [195], Raman spectroscopy, scanning electron microscopy (SEM) , transmission electron microscopy (TEM)

[196], atomic absorption spectroscopy [197], arsenazo III calcium assay [195], and o-cresolphthalein complexone calcium assay [198] measurements. However, till date, these in-vitro methods have not been able to demonstrate the limits of detection (LOD) needed to quantify calcium depositions in significantly low amounts during the early onset of calcification in aortic valves. Calcium quantification through histology is time-consuming and lacks accuracy due to false positive stained regions in image analysis. The spectroscopy methods used for calcium detection in calcified aortic valve tissues, including near-infrared (NIR) Raman [199], Fourier transform infrared (FTIR) [200] and atomic absorption [201] are all sensitive quantification techniques for calcium. However, NIR Raman can be prone to false positive results due to the heterogeneity of human tissue and high dependency on chemical band positions. On the other hand, FTIR is typically unable to quantify calcium contents within the aortic valves. Additionally, atomic absorption spectroscopy is limited to tissue sections and is an expensive technique [202]. Thus, there exists a critical need for robust in-vitro analytical techniques that can achieve rapid and highly accurate detection of extremely small calcium depositions in VICs with minimal sample preparation steps. In turn, such analytical advancements can expedite biomedical research in diagnosing the elusive origins of enhanced CAVD.

Laser Induced Breakdown Spectroscopy (LIBS) is a relatively non-destructive spectrochemical characterization technique, which can address the aforementioned issues in a facile, yet effective manner. Typically, LIBS involves the collection and processing of optical emissions emanating from a high-irradiance pulsed laser tightly focused to generate a high temperature, high pressure micro-plasma containing the analyte of interest [118]. These emissions (ionic, atomic and molecular), collected as spectral signatures, can reveal the constituents and properties of the plasma and hence, the sample. The relatively simple set-up and minimal sample preparations for

LIBS have drawn the attention of analytical researchers in recent years [119]. Additionally, the fast and easy operation, and data collection make LIBS ideal for in-situ applications [120].

In the past, LIBS has found a vast amount of applications in diverse spectral, and elemental studies ranging from combustion [203], and environmental/bio-hazard analysis [204], to explosives detection [176], pharmaceutical [131] and semiconductor and thin films [130] applications. Specifically, our recent application of calibration-free quantitative LIBS towards metal nanoparticles, carbonaceous aerosols and nanoalloy characterizations has established the technique at the forefront of elemental analysis in complex matrices [121-123, 132, 205]. In biological applications of LIBS, Hybl [206] showed the capability of LIBS as a bioaerosol classifier to distinguish different classes of biological agents using Principal Component Analysis (PCA). Kumar [207] introduced LIBS as an automated, real-time technique for cancer diagnosis based on the differences in the trace element concentrations in normal and malignant cells. Robotic surgery and laser surgery have been considered recently [208, 209]. A recent study has also used LIBS signatures resulting from tissue ablation to distinguish porcine gland from nerve tissues in order to create a feedback control mechanism during real-time laser surgery [209]. In regards to the application of quantitative LIBS for biological and biomedical studies, Samek [210] resorted to tissue-equivalent synthetic pellets of $CaCO_3$ as the external reference matrix to establish standard calibration curves for quantitative analysis of toxic elements in calcified hard tissue samples. The complexity of laser-sample interactions has mostly restricted the LIBS applications for calcified biological samples to quantitative elemental analysis of hard calcified tissues such as teeth, and bones [210, 211]. To this end, the commonly employed technique of lyophilization could possibly provide a solution for removing the moisture from the soft tissue samples without altering

the biological structures. But, to the best of our knowledge, no report exists on the use of LIBS to quantify calcifications in lyophilized VICs without any external calibration standard.

In this study, we establish LIBS for the first time as a quantitative analytical technique for in-vitro analysis of calcium depositions in VICs subjected to osteogenic culture over 2 to 21 days. The appearance of calcium deposits within the matrix is a sign of osteoblastic shift in valvular cells. Early diagnosis of CAVD demands fundamental research that can enable laboratory-based rapid screening and analyses of early calcification in VICs to understand the initiation and origin of the disease. For that, VICs behavior should be studied over time from normal to calcified conditions. Our goal was to identify the earliest time that the cultured VICs start to show any calcium depositions. Specifically, we investigate the evolution of the calcium atomic emissions for Ca I (422.67 nm) from LIBS measurements on the aforesaid VIC samples. Our results for the spectral signatures of Ca will be compared and correlated to calcium assays to demonstrate the efficacy of LIBS in quantifying the amount of calcium depositions in VICs. The LODs for both methods will be compared to establish the high-resolution capabilities of LIBS over the assays in detecting early-stage calcification in aortic valve cells.

B.2 Materials and methods

B.2.1 VIC isolation and culture

VICs were isolated from porcine aortic valve cusps (Wampler's Farm Sausage, Inc., Lenoir City, TN) by collagenase II digestion, as previously described 6, and cultured in growth media (DMEM, 10% FBS, 1% L-glutamine, and 1% Penicillin/Streptomycin) at 37^{o}C and 5% CO_2 until four passages. Unless otherwise specified, the VICs were seeded at a density of 250,000 cells/well into 6-well plates. To stimulate calcification on VICs, osteogenic media consisting of 2.18 g/L beta-glycerophosphate, 50 mg/L L-ascorbic acid 2-phosphate and 1mM dexamethasone (all purchased

from Sigma, St. Louis, MO) in regular media was added to the experimental samples. Control samples were cultured in regular media under similar condition. The media was changed every 2 days. Experiments were performed after 2, 4, 7, 10, 14 and 21 days of VIC culture in osteogenic media.

B.2.2 Lyophilization

VIC samples were freeze-dried prior to being used for LIBS quantification. At each time-point, the VIC monolayer was washed with phosphate-buffered saline (PBS). Then, the cells were removed from the well surface by scraping and transferred to silicon wafer substrates (rectangular, ~1x1cm^2). Subsequently, the VICs were frozen at -20^{0}C for at least 8 hours and then lyophilized overnight.

B.2.3 DNA content measurement

A fluorescence DNA assay was used to measure the cell density of the VIC samples [187, 212]. The VICs were scraped and digested in Proteinase-K solution (1mg/mL) (Sigma). Then, the cell lysates were incubated in a water bath for 90 minutes at a temperature between 60-70^{o}C and then heated at >70^{o}C for 30 minutes to denature the Proteinase-K. Hoechst 33258 dye (Sigma) was used to tag the released DNA and fluorescence emission was measured using a BioTek H1 plate reader at 458 nm. Calf thymus DNA standards (Sigma) were used in each assay to calculate DNA density.

B.2.4 Calcium assay

A colorimetric calcium assay based on arsenazo dye was used to measure the calcium content of the osteogenic VICs [187]. First, VICs were homogenized in 1N acetic acid, then arsenazo dye was added to the samples. The calcium content was measured against calcium standard (Ricca chemical, Arlington, TX). Samples absorbance was detected at 650 nm using a BioTek H1 plate reader. The calcium content was normalized to total DNA content.

B.2.5 Von Kossa staining

Von Kossa staining was used to determine the amount of calcium deposition [187]. The VICs in each well were fixed in 10% formalin (Fisher Scientific, Fair Lawn, NJ). After washing with distilled water for 3 times, a silver nitrate (Ricca Chemical Co., Arlington, TX) solution (3%) was added to the fixed VICs. Then the samples were incubated and exposed to UV until the calcium salts turned dark brown or black. The undissolved salts were removed using a 5% sodium thiosulfate (Sigma) solution and dehydrated with Flex before imaging. 10X images of the calcific depositions were obtained with a bright field microscope (Motic Inc., BC, Canada), and ImageJ software (NIH) was used for image analysis.

B.3 Results and discussion

Colorimetric calcium assay results show that the calcium content of VICs cultured in osteogenic media increases overtime wherein after 14 and 21 days of osteogenic culture, the calcium content is significantly increased compared to the VICs at day 10 of osteogenic culture (Figure B.1a).

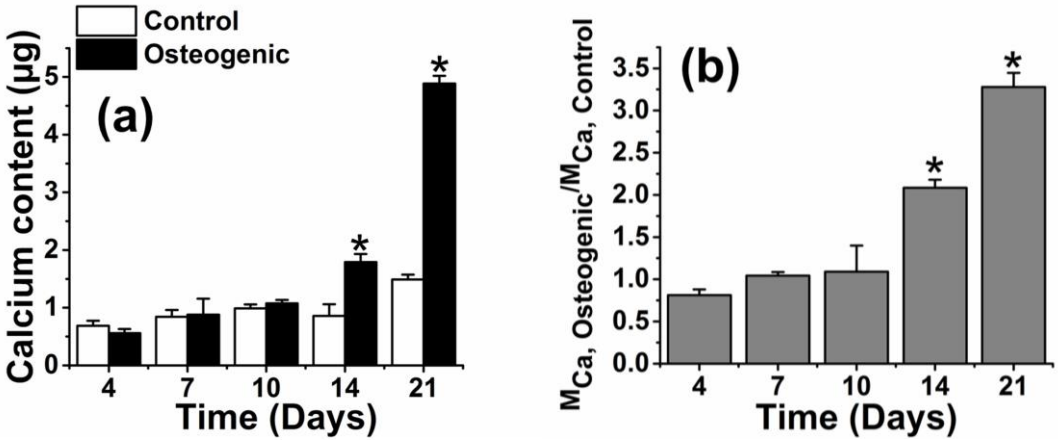

Figure B.1: (a) Calcium assay results for control and osteogenic VICs after 4, 7, 10, 14 and 21 days of culture in osteogenic media, *p<0.05 compared to osteogenic day 10 (b) normalized calcium content of osteogenic VICs to respective controls at each time point. The data represents mean ± std. error, n=3 porcine aortic valves, *p<0.05 compared to respective control.

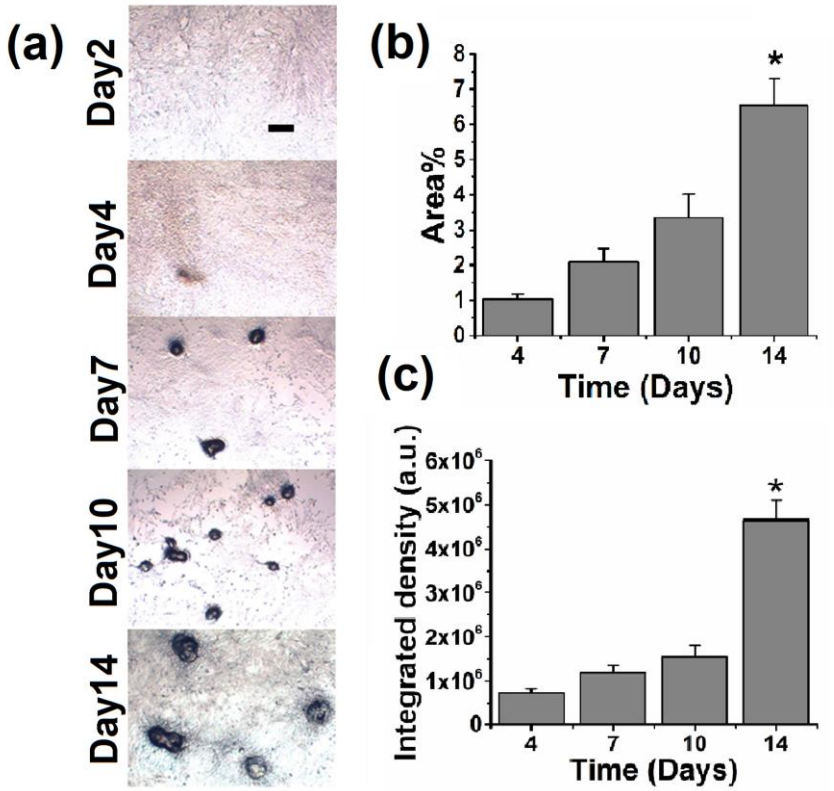

Figure B.2: (a) Von Kossa staining of VICs cultured in osteogenic media for 2, 4, 7, 10 and 14 days; the scale bar is 250µm. Image analysis results showing (b) area percentage (c) integrated density of the calcium deposition within VICs cultured in osteogenic media for 4, 7, 10 and 14 days. The data represents mean ±std. error, n=3 porcine aortic valves, *P<0.05.

Moreover, the calcium fold changes (calcium content normalized to respective controls) are significantly elevated in VICs after 14 days of culture in osteogenic media (Figure B.1b). However, for smaller amounts of calcium, the assay results have observable fluctuations between experimental and control VICs at day 4 and are unable to detect the calcium content at day 2 (Figure B.1a). Similarly, analysis of calcium deposition among VIC monolayers by Von Kossa staining show increased calcification overtime (Figure B.2a). The representative images of calcium deposition in Figure B.2a shows the nodules within VICs cultured in osteogenic media at different time points. It is obvious that at day 2 of osteogenic culture, no calcium deposition can be observed. Image analysis results demonstrate significantly elevated area percentage covered with calcium deposition and integrated density in VICs cultured in osteogenic media at day 14 as compared to

the corresponding values over 4 – 10 days (Figure B.2b, c). Osteogenic differentiation of the VICs cultured in osteogenic condition advances over time and can be evaluated by change in the identified osteogenic markers. In a study on rat VICs cultured in osteogenic media for 7 and 14 days, the amounts of osteogenic markers increased significantly at day 14 compared to day 7, showing that longer duration of culture is associated with increased calcification [213]. Our calcium assay results are consistent with previous studies showing that amount of calcium increases over the time range of 4 to 21 days.

Representative LIBS spectra for Ca I (422.67 nm) atomic emission lines from VIC samples at day 10 collected over various gate delays are shown in Figure B.3. It can be observed that the emission intensity of the 422.67 nm line decreases in time as a result of the diminishing continuum spectral background due to the recombination of free ions with electrons within the plasma that finally leads to atomic transitions from electronically excited to ground state. The temporal decrease in the absolute line intensity is accompanied by the respective decrease in the noise that results in an optimal gate delay wherein the analyte signal is relatively high as compared to the continuum noise in the spectrum. The temporal variations in signal-to-noise ratio (SNR) for the Ca I (422.67 nm) line, as shown in the inset in Figure B.3, indicates the optimal SNR to be 3 μs. Therefore, for all quantitative analysis presented here, we use a gate delay of 3 μs and a gate width of 5μs for the Ca I (422.67 nm) detections in the VIC samples. The spectral signatures from osteogenic VICs cultured over days 2 to 21 are illustrated in Figure B.4a indicating an increase in Ca I (422.67 nm) peak over time due to increasing calcium contents. The extent of calcification can be inferred by comparing the respective spectral signatures from osteogenic and control VICs, as indicated in Figure B.4b for the specific case of osteogenic VICs cultured over 21 days. It is observed that except for the specific emission peak of Ca I (422.67 nm), both the control and analyte spectra

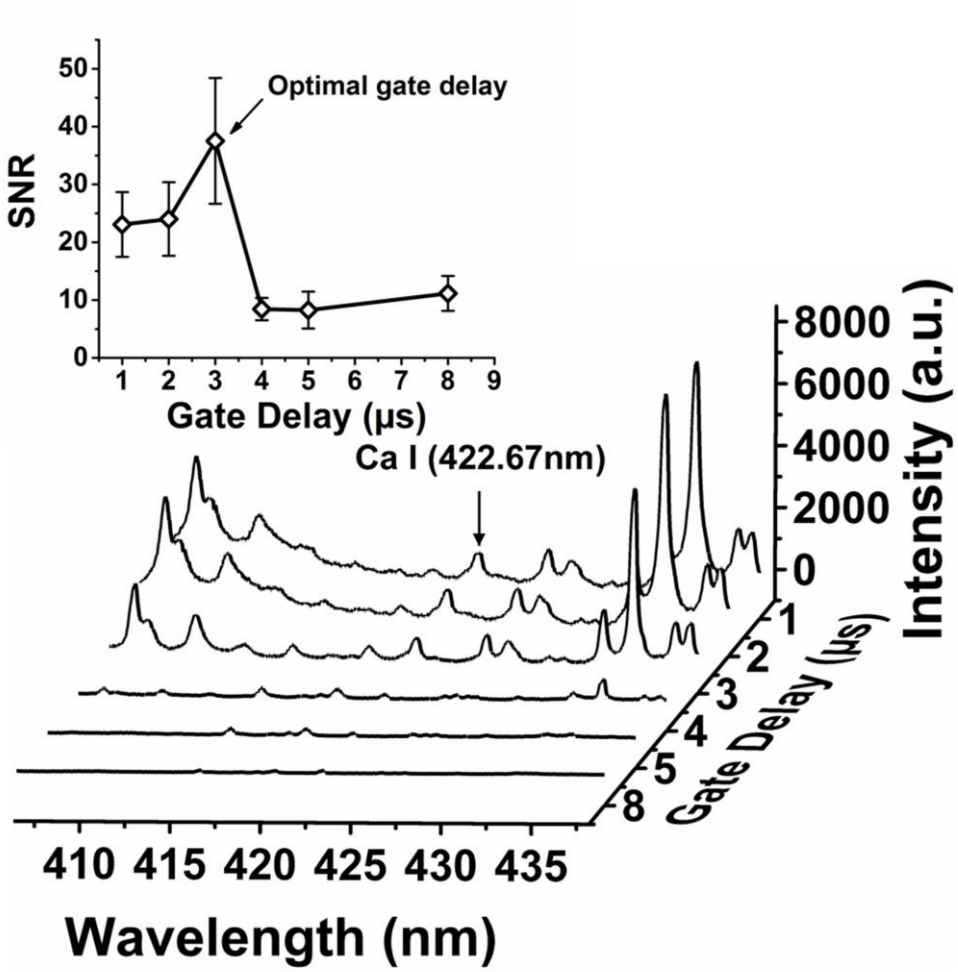

Figure B.3: LIBS spectra at different gate delays for Ca I (422.67 nm) emission line from day 10 osteogenic VIC samples. (Inset: SNR for Ca I line indicating optimal gate delay ~ 3 usec).

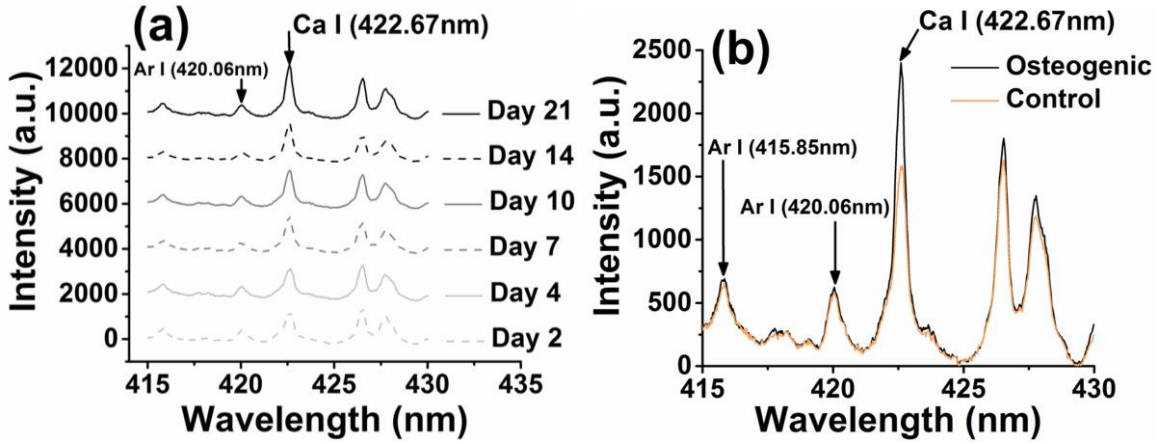

Figure B.4: (a) LIBS signatures for Ca I (422.67 nm) emission line from osteogenic VICs at various time points of cell culture (spectra are shifted for better visualization); (b) Comparison of Ca I (422.67 nm) emissions from osteogenic and control VICs at day 21.

demonstrate comparable emissions for the spectral signatures from the background Ar gas over the wavelength window of interest. This confirms that the spectral enhancement in the analyte line of interest (422.67 nm) arises specifically from the relevant differences in the calcium content between the control and osteogenic VICs, and is not an experimental artifact due to shot-to-shot fluctuations. The evolution of the effective LIBS emissions (SNR) from both control and osteogenic VICs cultured over the 2 to 21 days are shown in Figure B.5a. The slight variations in the SNR values for the control VIC samples over time can be attributed to shot-shot variations, especially considering the fact that the respective SNRs for the osteogenic VICs indicated consistently higher and temporally increasing values. The effective LIBS signal is proportional to the atomic number densities of calcium in the plasma volume as per the Maxwell-Boltzmann relations:

$$I_{em} \propto N_i \exp\left(-\frac{\Delta E_{ki}}{k_B T_{exc}}\right)$$

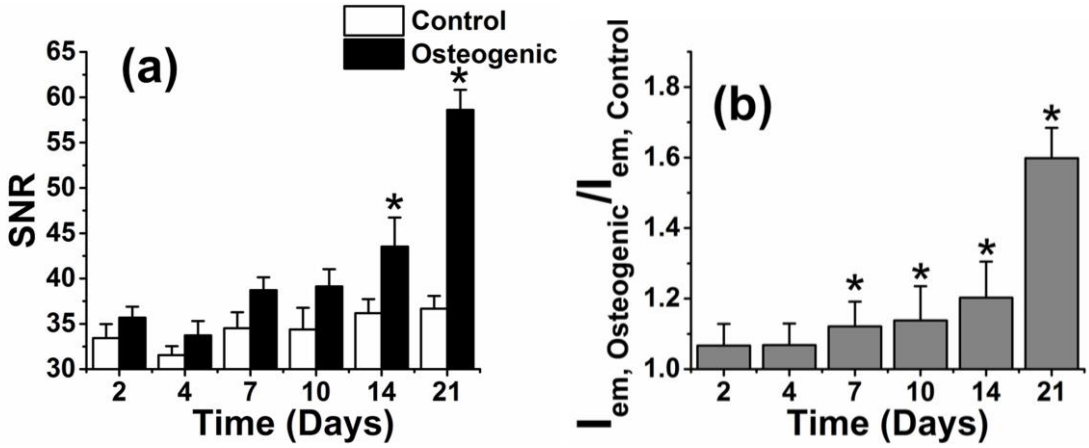

Figure B.5: (a) LIBS results for control and osteogenic VICs after 2, 4, 7, 10, 14 and 21 days of culture in osteogenic media, *p<0.05 compared to osteogenic day 10 (b) normalized calcium content of osteogenic VICs to respective controls at each time point. The data represents mean ± std. error, n=3 porcine aortic valves, *p<0.05 compared to respective control.

where ΔE_{ki} is the energy difference between the transition states, and T_{exc} is the plasma temperature. Hence, the differences in the effective signals from the control and osteogenic VICs can be directly correlated to the differences in the relative calcium contents in the respective VIC samples. To account for the artifacts arising from spectroscopic, optical and experimental factors affecting the measured relative emission intensities at different conditions of the plasma evolution, Figure B.5b indicates the effective signals from osteogenic VICs are normalized to the respective signals from the control samples ($I_{em,\ osteogenic}/I_{em,\ control}$) at 3 μs for the different days of cell culture. For each osteogenic VIC sample, the $I_{em,\ osteogenic}/I_{em,\ control}$ ratios in Figure B.5b are proportionately higher than unity for the different days of culture, thereby confirming the excess calcium contents in osteogenic VICs over their respective controls. These results are even consistent over the early stages of calcifications (i.e., the samples cultured for 2 to 4 days). This definitely supports our hypothesis that the cultured VICs deposit elevated amounts of calcium as compared to their respective controls over all stages of osteogenic differentiation. In turn, these results point towards the ability of LIBS to resolve the onset of calcium depositions in early-stages of osteogenic differentiation ($I_{em,\ osteogenic} > I_{em,\ control}$ for both day 4 and day 7 VIC samples in Figure B.5a and b). On the other hand, the calcium assay fails to indicate any detectable signal above the background fluctuations for the VICs cultured up to day 7 (specifically, $M_{Ca,\ osteogenic}/M_{ca,\ control} < 1$ for day 4 in Figure B.1b). Additionally, neither the calcium assay nor the Von Kossa staining is able to detect any calcium deposition within osteogenic VICs after 2 days of culture. This indicates the inadequacy in the detection limits of the calcium assay.

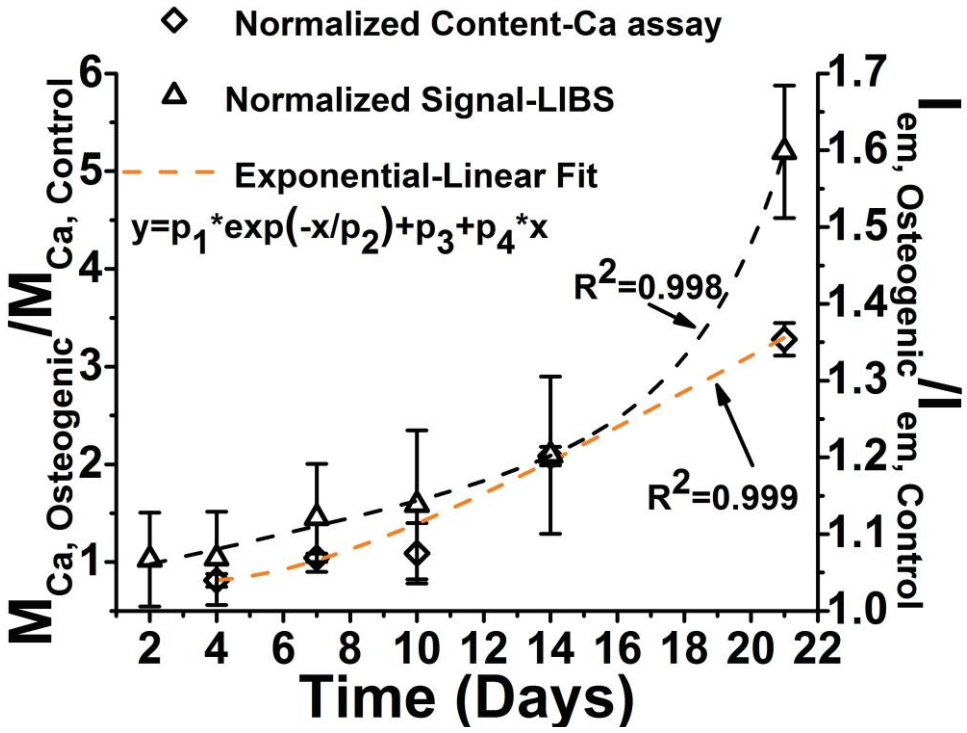

Figure B.6: Time evolution curve for the normalized LIBS signal intensities ($I_{em,\ osteogenic}/I_{em,\ control}$; right y-axis) and assay measurements ($M_{Ca,\ osteogenic}/M_{ca,\ control}$; left y-axis) for calcium contents in the osteogenic VIC samples indicating the similar linear-exponential trends for calcium depositions over the different periods of cell culture. (Fit equation as shown in the plot)

However, a greater sensitivity and superior detection limits of LIBS enable us to detect spectrally significant calcium signals from VIC samples with as early as 2 days of cell culture. A time evolution curve, as shown in Figure B.6, is established for both normalized LIBS signals (from Figure B.5b) and assay measurements (from Figure B.1b) for the calcium contents in the osteogenic VIC samples. Fitted curves for both the aforementioned normalized data indicate a linear increase up to day 14 of VIC osteogenic culture which is subsequently followed by an exponential increase until day 21 (Figure B.6 indicates the linear-exponential fit used). Therefore, one can observe a direct correlation between the calcium signal measurements from LIBS and calcium deposition detections from calcium assay. To this end, Figure B.7 establishes the linearity (R^2 = 0.94) in the correlation curve between normalized Ca signal emissions from LIBS ($I_{em,\ osteogenic}/I_{em,\ control}$) and calcium contents from calcium assay ($M_{Ca,\ osteogenic}/M_{Ca,\ control}$).

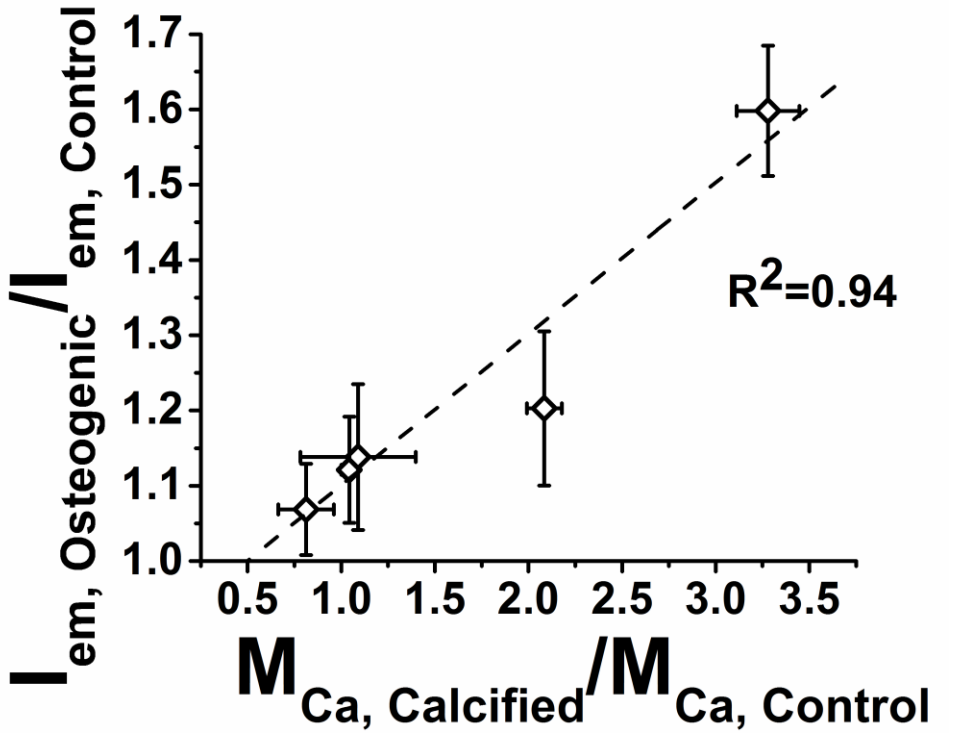

Figure B.7: Linear correlation between normalized Ca signal emissions from LIBS ($I_{em,\ osteogenic}/I_{em,\ control}$) and normalized calcium content from calcium assay($M_{Ca,\ osteogenic}/M_{ca,\ control}$).

It should be noted that the day 4 calcium assay data from Figure B.1a indicate lower calcium content in the osteogenic VICs as compared to the respective controls. This is highly unlikely since it contradicts our very hypothesis that the cultured VICs deposit elevated amounts of calcium as compared to their control cell counterparts over all stages of osteogenic differentiations. Therefore, we infer that day 7 is the earliest time point during the cell culture durations in our study that allows for conclusive measurement of calcium content by calcium assay. In this context, the LOD for the assay measurements at day 7 is estimated to be ~0.84 µg. Our LOD from calcium assay measurements is relatively smaller or in the similar range as compared to previous studies using calcium assay approach that reported LODs of 1.5 [214], 50 [215],and 0.9µg [216] for measured calcium contents in marrow stromal, vascular smooth muscle and mesenchymal stem cells.

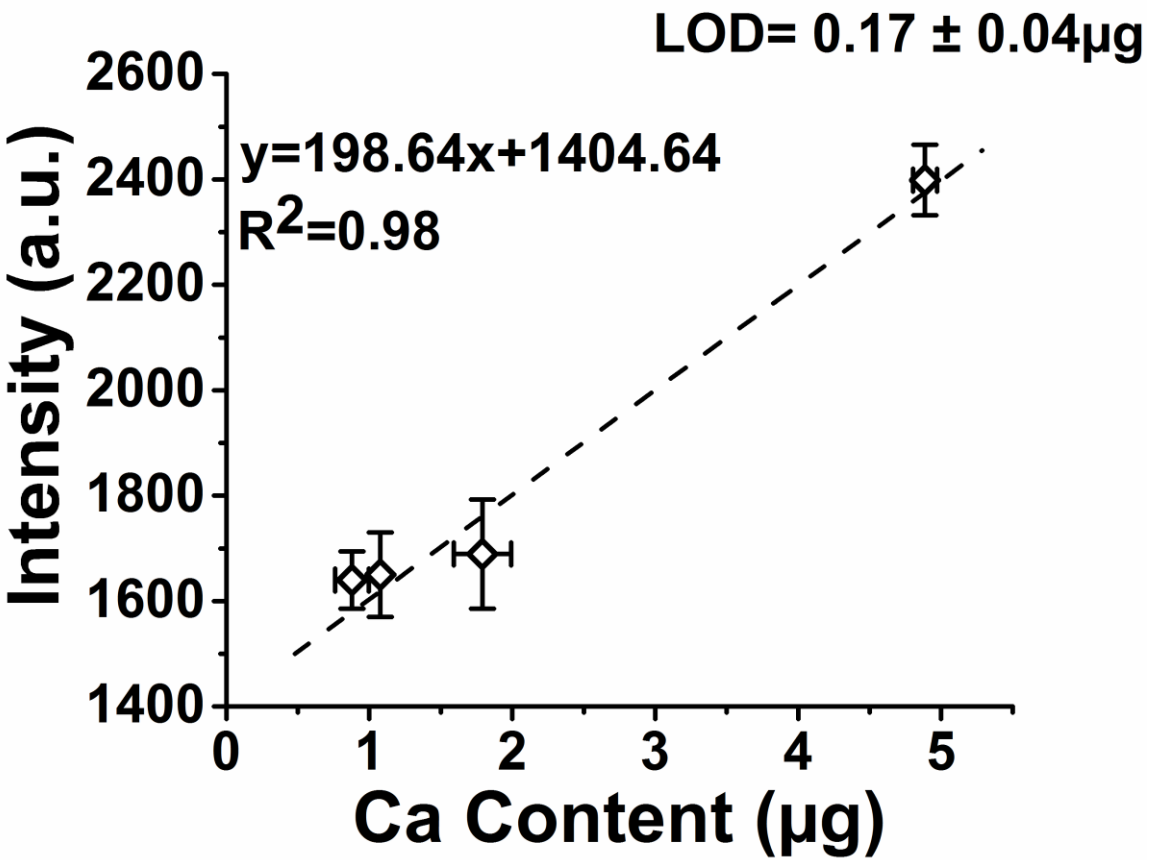

Figure B.8: LIBS calibration curve for signal intensities from Ca I (422.67 nm) emission lines as a function of calcium content estimated from calcium assay. LOD is estimated based on the slope. Error bars represent ± std. error

In contrast, the normalized calcium signals measured by LIBS is observed to be greater than unity for all VIC samples even at time points as early as 2 and 4 days of culture. To this end, we quantitate our current LIBS analysis via LOD measurements from the calibration curve in Figure B.8 that relates the detectable calcium assay measurements over 7 to 21 days to the corresponding LIBS calcium signals. We adopt the following definition of LOD here:

$$\text{LOD} = \frac{3\sigma_B}{S}$$

where, σ_B is standard deviation of the background of spectra and S is the slope of the linear fit to the calibration curve as shown in Figure B.8. The calibration curve shows good linearity (R^2=0.98),

and the estimated LOD for calcium from our LIBS measurements is found to be ~ 0.17 ± 0.04 µg which indicates a 5-fold improvement over calcium detection from the assay.

B.4 Conclusion

In this study, we established a significant milestone in using LIBS as an analytical tool for quantitative in-vitro detection of small amounts of calcium in cellular samples that are undetectable by conventional methods. LIBS signals for Ca emissions from analyte samples of osteogenic VICs were distinctly identified as enhancements over the corresponding signals from control cells, thereby establishing the specificity of the LIBS analysis. A linear correlation between the LIBS signal and the biochemical calcium assay results was observed that indicated a systematic increase in the Ca signals from osteogenic VICs cultured over different durations of time. While the calcium assay could significantly detect calcifications in VICs only after 7 days of culture, the LIBS results could reliably resolve Ca signals from osteogenic VICs as early as 2 days of culture. A calibration curve for the LIBS results was generated that established the LOD for quantitative calcium detection to be ~0.17 ± 0.04 µg, thereby indicating a 5-fold improvement over the conventional calcium assay measurements. Our results indicate that LIBS provides significantly lower LOD over calcium assay and histology techniques. In future, such studies may aid the fundamental research in the determination of the initiation point of calcification in aortic valves. The results from the present study provide a novel and accurate bio-analytical tool for measuring low amounts of calcium in cell samples for in-vitro pathological studies on laboratory platforms. Further investigations are required in future to assess the possibility of using LIBS for in-vivo applications.

Vita

Seyyed Ali Davari received his B.S. in mechanical engineering from Sharif University of Technology in 2012. During his undergraduate studies, he was a researcher at Institute for Research in Fundamental Sciences (IPM) working on turbulence flows over the national observatory under supervision of Dr. Mir Abbas Jalali. Later, he joined University of Tennessee for pursuing his Ph.D. in mechanical engineering under supervision of Dr. Dibyendu Mukherjee in January 2013. During his graduate studies, he obtained a minor in computational science in 2017. His research focuses on synthesis and characterization of metallic, intermetallic nanoalloys and composites for energy and energetic applications through stochastic modeling, laser ablation in solution and laser-induced breakdown spectroscopy. His research works have manifested in terms of ten published and under review papers, one book chapter and one invited book. Ali will continue his academic career as a postdoctoral fellow at UC Davis to develop LIBS for air quality monitoring.